Università degli Studi di Padova

Dipartimento di Fisica e Astronomia Galileo Galilei

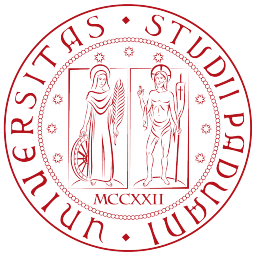

Tesi di laurea magistrale in Fisica

Looking for planets with SPHERE in planetary systems with double debris belt

Laureando:
Cecilia Lazzoni

Relatore:
Prof. Francesco Marzari
Corelatore:
Prof. Silvano Desidera

Contents

Chapter 1

Introduction

Debris disks are optically thin, almost gas-free dusty disks observed around a significant fraction of main-sequence stars older than about 10 Myr. Since the circumstellar dust is short-lived, the very existence of these disks is considered as an evidence that dust-producing planetesimals are still present in mature systems, in which planets have formed- or failed to form- a long time ago. It is inferred that these planetesimals orbit their host star at asteroid to Kuiper belt distances and continually supply fresh dust through mutual collisions.
The main aim of this work is to analyze systems that own a debris disk composed of two debris belts, similar to our Solar System, one of which is in the interior part of the system near to the star at distances similar to the asteroid belt at $3,5$ AU, and the other one is in the outer regions at distances similar to the Kuiper belt at 30 AU. The gap between the two belts is assumed to be almost empty. In order to explain the existence of this vacuum space the most simple assumption is to assume the presence of one or more planets orbiting the star between the two belts. This hypothesis is also the most likely and thus makes such systems very interesting for exoplanets researches, even if some other mechanism may be at work. For example, self-stirring due to the largest planetesimals in the belts could possibly produce a disk with particular features such as two distinct components.
The choice of the systems has been done crossing the elements of the catalog of Chen ([4]) modeled with two debris belts from SEDs analysis and the targets of SPHERE, an instrument of high-contrast direct imaging at VLT. We ended up with almost forty systems with ages between 10 and 500 Myr and beneath 150 pc from the Sun.
We started the analysis with one planet on circular orbit as responsible for the entire gap, but we needed too massive objects. Therefore we moved to study the case of one planet on eccentric orbit. We first performed numerical simulations in order to confirm the validity of the equations we used. As we expected, as the eccentricity of the planet increases its mass becomes smaller.
We compared these results with the detection limits curves of SPHERE. These graphics plot the mass of the planet M_p versus its semi-major axis a_p. Points beneath the curve are not detectable whereas point above it are indeed detectable. In most cases, the only planet of the system would have been detected and, as far as actually it has not been found, we moved to analyze multi-planetary models.

We first assumed the presence of two and three equal mass planets on circular orbits around their star. These hypothesis are very restrictive but they helped us to get a first view into the stability of multiple planetary systems using the Hill's stability criterion. We compared again the results with detection limits and we obtained that, for such starting assumptions, triple planetary systems are more likely to be responsible for the gap.
The last step of our analysis was to consider two equal-mass planets on eccentric orbits. We found that the stability of the system depends much more on the eccentricities of the two planets than on their masses. Thus little variations of $e_{p,1}$ and $e_{p,2}$ cause steep variations in M_p and a sudden passage between detectability to undetectability.
In Appendix D we present the application of our procedure to the system HIP67497 recently spatially resolved with SPHERE. In chapter 2 and 3 we are going to briefly resume how a planetary system forms and the physics that lies behind debris disks; in chapter 4 we present the techniques most used in finding exoplanets (with particular attention to radial velocities methods and direct imaging); in chapter 5 we illustrate how the targets were chosen and some characteristics of the systems studied; chapter 6 and 7 are dedicated to stability analysis of single and multiple planetary models; chapter 8 illustrates double debris belts systems in which planets have been found using radial velocities techniques; chapter 9 resumes our conclusions.

Chapter 2

Planetary System Formation

We are going to briefly resume how a planetary system takes form, from the earliest stages when the star takes its place in the main sequence and has a young disk of gas and dust that surrounds it, to later epochs, when the system settles down and planets form. For a more complete vision of these arguments see also *Astrophysics of planet formation* by P. J. Armitage.

2.1 Protoplanetary disk

Planets form from gas and dust that surround young stars for the first few millions years of their evolution. Gas and dust belong to a common structure that is called protoplanetary disk. In order to understand how such disks born we have to investigate the process of star formation. Stars generate from gas in giant and cold molecular clouds that are not homogeneous structures. Therefore, by means of turbulence phenomenon, any collapsing region will possesses nonzero angular momentum. Thus disks form because particles in it have too much angular momentum to collapse directly to the star. Protoplanetary disks survive for quite a long time because once gas settles around a young star its specific angular momentum increases with radius. In order to accrete, angular momentum must be dissipated or redistributed within the disk, and this process turns out to require time scales that are much longer than the orbital or dynamical time scales. We can consider the entire structure as (quasi) static and this suffices for a first study of temperature, density and composition profiles of protoplanetary disks, which are of great interest for models of planet formation. Observationally, it is clear that protoplanetary disks are not static structures, but rather evolve slowly over time. This is, however, a very good approximation that helps us to describe the structure of the disk. We can assume two more simplifications beyond the stationarity. First, we can assume the total disk mass to be much smaller than the mass of the star, $M_{disk} << M_*$, and this allows us to neglect the gravitational potential of the disk and to take into account only stellar gravity. Second, the vertical thickness of the disk h is a small fraction of the orbital radius r. This follows from the fact that a disk has a large surface area and can cool via radiative losses rather efficiently. Indeed, efficient cooling implies relatively low disk temperatures and pressures, which are unable to support the gas against gravity except in a geometrically thin disk configuration

with $h/r << 1$. All these assumptions are of great usefulness when we try to solve the dynamics and structure of the disk.

2.2 Planetesimals

In order to form a body that has the typical dimensions of terrestrial planets ($M_p \sim 10^{24}$kg, $R_p \sim 10^3$km), micron-sized particles require to grow up to 12 orders of magnitude in size scale. This process begins with planetesimals formation.
The first step to understand how a particle evolves within the protoplanetary disk is to calculate the aerodynamic force experienced by the particle that has a relative velocity v with respect to the local velocity of the gas disk. This force takes different expressions depend on which physical regime we are looking at. Let us suppose the particles to be spherical and solid with radius s and density ρ_d. Moreover, let us call λ the mean free path of gas molecules within the disk. If $s < \lambda$ then the fluid on the scale of the particles is effectively a collisionless ensemble of molecules with a Maxwellian velocity distribution. The drag force in this regime- which is normally the most relevant for small particles within protoplanetary disks- is called the *Epstein drag* and is described by

$$\mathbf{F_D} = -\frac{4\pi}{3}\rho s^2 v_{th}\mathbf{v} \tag{2.1}$$

where v_{th} is the thermal velocity defined as

$$v_{th} = \sqrt{\frac{8k_B T}{\pi \mu m_H}}. \tag{2.2}$$

T and ρ are the temperature and the density of the gas and μ is the mean molecular weight. If, instead, $s > \lambda$, the particle is in the so called *Stokes drag regime* and the disk flows as a fluid around the obstruction presented by the particle. In this case the drag force is well expressed by

$$\mathbf{F_D} = -\frac{C_D \pi}{2}\rho s^2 v\mathbf{v} \tag{2.3}$$

and C_D is the drag coefficient.
In each regime the force scales with the frontal area πs^2 that the particle presents to the gas. This means that the acceleration caused by gas drag, which is proportional to the drag force divided by the particle's mass $\mathbf{F_D}/m_d$, decreases with particle size. For example, for spherical particles we can assume $m_d = \frac{4\pi}{3}s^3\rho_d$ and thus the acceleration scales as s^{-1}. It is now clear that as particles grow up in size the effects of drag forces become weaker and weaker and eventually negligible once bodies of planetesimal size have formed.
Aerodynamic drag on particles is an important effect for understanding both the vertical distribution and radial motion of dust and larger bodies within the protoplanetary disk. To begin with, we ignore turbulence and consider the vertical settling and growth of dust particles suspended in a laminar disk. We can quantify how much the solid and gas components are coupled by defining the friction time scale for a particle of mass m as

$$t_{fric} = \frac{mv}{|F_D|} \tag{2.4}$$

where v is the relative velocity between the particle and the gas. The friction time scale measures the time in which drag modifies the relative velocity significantly. Thus, as we have already noticed above, small dust particles are strongly coupled to the gas.
If we make use of the approximation that considers the mass of the disk to be slightly smaller than the mass of the star, the only contribute to gravitational forces comes from the latter. Therefore, a small particle at height z above the mid-plane of a laminar disk experiences a downward vertical force, generated by the z component of the stellar gravity. The gas in the disk is supported against this force by an upwardly directed pressure gradient, but no such force acts on a dust particle. Therefore, if started at rest, a solid particle will accelerate downward until the gravitational force will be balanced by aerodynamic drag. Particles drifts toward the disk mid-plane with a terminal velocity defined by

$$v_{settle} = \frac{\rho_d s}{\rho v_{th}} \Omega^2 z \tag{2.5}$$

where $\Omega = \sqrt{GM_*/r^3}$ is the local Keplerian velocity, r is the radial distance from the star, ρ and ρ_d are the densities of the gas and dust, respectively. The time required for the settling of particles is

$$t_{settle} = \frac{2\Sigma}{\pi \rho_d s \Omega} e^{-\frac{z^2}{2h^2}} \tag{2.6}$$

and Σ is the surface density of the disk.
We thus expect that the time required to a micron size particle to sediment on the mid plane will be much shorter than the disk lifetime.
During the migration from the upper part of the layer to its center, particles will collide with one another and grow. As we can see from eq. (2.5), the settling velocity increases with particle size, so any such coagulation accelerates the collapse of the dust toward the disk mid-plane. We can, however, consider two different scenarios: one leads to cohesion between particles and the other one to disruption in smaller bodies. When we treat the initial dust particles, collisions are likely to cause particle adhesion leading to a rapid growth from sub-micron scales up to small macroscopic scales. The effect of collisional disruption becomes dominant when larger particles have formed and have high relative velocities. This kind of effect helps us to explain the presence of a population of small grains that survive to late times, as seen from infrared (IR) excesses present in most of classical stars (more problematic is to understand how the population of small grains survive even longer). Therefore, the process of fragmentation allows a broad distribution of particle sizes to survive out to late times but it is not efficient for collisions at relative velocities of the order of a cms^{-1} (values typical of settling for micron-sized particles) and becomes more probable for collisions at velocities of a ms^{-1} or higher.
Until now we have neglected the effect of turbulence. Turbulence acts to stir up small solid particles, preventing their settling into a thin layer at the disk mid-plane. The condition for solid particles to become strongly concentrated toward the disk mid-plane in the presence of turbulence is

$$\Omega t_{fric} >> \alpha \tag{2.7}$$

where t_{fric} is given by eq.(2.4), Ωt_{fric} is called dimensionless friction time and α is the Shakura Sunyaev prescription. For any reasonable value of α this implies

that substantial particle growth is required before settling takes place.
Once the different sized particles have reached the mid plane of the disk we have to analyze how their radial velocities evolve. The first important effect to consider is due to different forces experienced by solid and gas particles. The gas in the disk is partially supported against gravity by an outward pressure gradient, that does not apply to solid particles, and then it orbits at sub-Keplerian velocity that can be expressed by

$$v_{\phi,gas} = v_K(1-\eta)^{1/2}, \tag{2.8}$$

where $v_K = \sqrt{GM_*/r}$ is the classical Keplerian velocity and $\eta = nc_s^2/v_K^2$.
For a small dust particle, aerodynamic coupling to the gas is very strong. To a good approximation the dust will be swept along with the gas, and its azimuthal velocity will equal that of the disk gas. Since this is sub-Keplerian, the centrifugal force will be insufficient to balance gravity, and the particle will spiral inward at its radial thermal velocity.
Large rocks, that are poorly coupled to the gas, are affected by a similar phenomenon. In this case the aerodynamic forces exerted by the gas component can be regarded as perturbations to the orbital motion of the solid body, which orbits the star with azimuthal velocity that is close to the Keplerian speed. This is faster than the motion of the sub-Keplerian disk gas, and as a result the rock experiences a sort of wind that tends to remove angular momentum from the orbit. The loss of angular momentum again results in inward drift.
Therefore we can guess two main conclusions. The first one is that planetesimal formation must be rapid, at least if it occurs via a cascade of pairwise collisions that lead to an overall growth. Indeed, if this was not the case the great part of the solid material in the disk would drift toward the star to be evaporated in the hot inner regions. The second one implies that the radial redistribution of solids is very likely to occur.
As said above, particles will be affected by the gas leading to radial drifts quite different for small and large particles. This effect introduces relative velocities between particles of different sizes, which can promote collisions and (possibly) growth via coagulation. The most simple assumption is to consider all collisions as adhesive. However this is not a likely scenario as problems arise when there are high relative velocities between particles. The resultant high energy collisions between large rocks will break up them into smaller bodies. This is a remarkable complication of the further evolution of the system and no real solution has yet been reached to explain the process that leads to the formation of km-scale planetesimals.
The simplest model is based on the idea that growth to km-scale occurs via a succession of pairwise particle-particle collisions that result on an average growth. Even if coagulation appears an unavoidable process for particles less than about a meter in size and adhesive collisions between small particles result in particle growth on very short time scales, it is harder to imagine larger boulders, with high relative velocities due to aerodynamic effects, sticking together. Therefore, this size regime is quite difficult to model and represents a lack in our knowledge.
Thus far we have assumed that the only important interactions between particles are physical collisions, and that those particles are dynamically unimportant for the evolution of the gas disk. Indeed, at early epochs when the disk has just

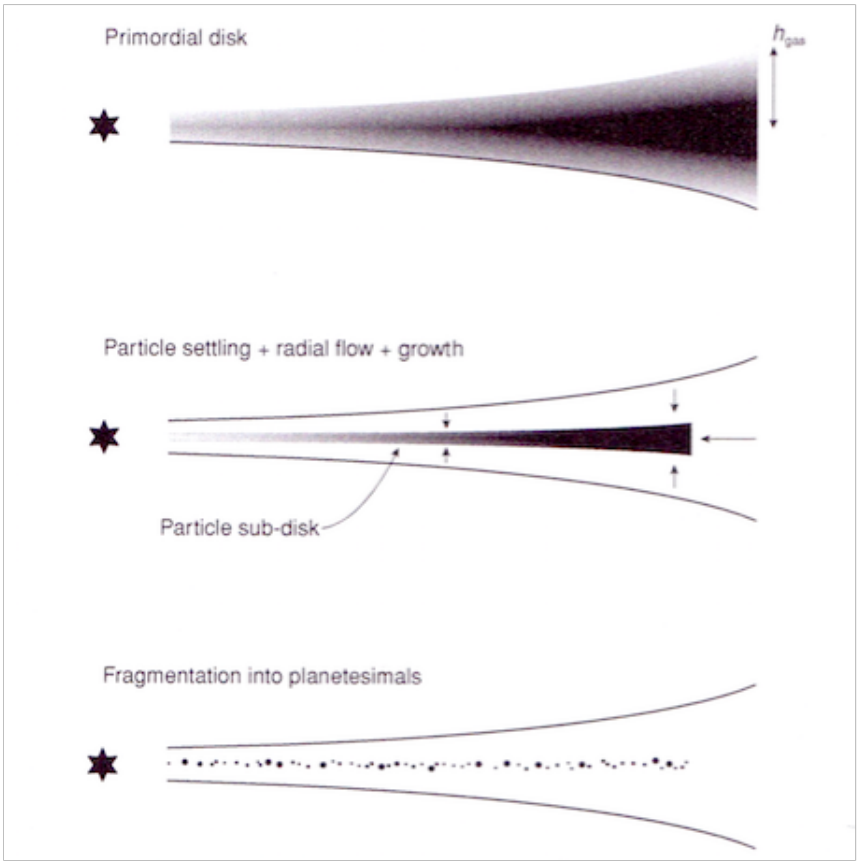

Figure 2.1: Steps that take to the formation of planetesimals. Credits: [1]

formed, the mass of the gas component is much greater than the total mass of the solids and dust particles are small and distributed uniformly throughout the gas disk. But, as the disk evolves in time, these conditions may be locally violated due to some combination of vertical settling, radial drift and photoevaporation. If the solid particles start to play a dynamical role a number of new physical effects may occur.
One of these is the gravitational instability generated within a dense layer of particles located close to the disk mid-plane. Such an instability, known as the *Goldreich-Ward mechanism*, might result in the prompt formation of planetesimals. The condition for a Keplerian disk to be marginally unstable to gravitational instability is expressed using the *Toomre parameter* Q

$$Q = \frac{c_s \Omega}{\pi G \Sigma_0}, \tag{2.9}$$

and is given by

$$Q < 1. \tag{2.10}$$

Thus, disk will become unstable to its own self-gravity when $Q < Q_{crit}$, where Q_{crit} is of the order of unity, even if quite larger than 1.

Another mechanism comes from the existence of new two-fluid instabilities that arise because of the coupling between the solid and gaseous components. These might result in clumping of the solid particles and promote planetesimals formation either via direct collisions or via gravitational collapse. In order to explain how such disk instabilities generate, we can outline three stages of the evolution of the system. In the first one the solid component of the disk is homogeneously distributed with the gas. In the second stage, dust settles vertically to form a thin sub-disk of particles around the $z = 0$ plane. Turbulence causes a stir up in dust particles, so substantially settling requires at least some collisional growth to have occurred. Radial drift can also, in principle, contribute to an increase at the mid-plane particle density in the inner disk. In the third stage the sub-disk, composed of solid particles, becomes unstable due to some combination of high surface density and/or low velocity dispersion. This may lead to the formation of bound clumps of particles, which rapidly agglomerate to form planetesimals. As outlined in this paragraph, we know very little about planetesimals formation, and thus about planets formation. To summarize, there appears to be no theoretical impediment to the rapid growth of dusty or icy particles up to small macroscopic dimensions. The growth mechanism at these scales is well described by pairwise collisions that result in sticking, and the time scale in the inner disk can be surprisingly short ($10^3 - 10^4$ yr within a few AU from the star). The fact that dust is still present in the inner regions of disks with ages of several Myr seems to suggest that erosive collisions proceed parallel with growth mechanism, provide always fresh dust.
Growth beyond the mm or cm size regime presents greater challenges. One possibility is that rapid pairwise growth continues all the way from dust scales up to planetesimals. A second chance is that gravitational instability forms planetesimals rapidly from much smaller objects, bypassing many of the scales for which collisional growth is most uncertain.
Nevertheless, there are empirical observation of planetesimals. For example the Solar System has solid bodies of varying composition, which are presumably descend from planetesimals, all the way from Mercury (at 0.4 AU) out to the edge of the classical Kuiper Belt (at about 47 AU). For these reason, even if we can not constrained planetesimals formation yet, they are clearly a fundamental step to planet formation models.

2.3 Terrestrial Planets

We want now to analyze how a terrestrial planet borns. From the previous paragraph we understand that, even if the theory is not well constrained, planetesimals are very likely to form. The physical process that controls further growth of planetesimals in bigger objects is mostly mutual gravitational interaction. From now on the only role that gas disk plays is to provide a modest degree of aerodynamic damping of protoplanetary eccentricity and inclination. Using this assumption, the physics involved is simple and the problem of terrestrial planet formation is well posed even if it is not easy to solve. It would take $4\text{x}10^9$ planetesimals with a radius of 5 km to build the Solar System's terrestrial planets, and it is inadvisable to directly simulate the N-body evolution of such a number of objects. Thus, for the earliest phases of terrestrial planet formation a statistical approach is both accurate and efficient. Then, when the

number of dynamically significant bodies has dropped to a manageable number, direct N-body simulations become feasible, and these are used to study the final assembly of the terrestrial planets.
As mentioned above, terrestrial planets form from planetesimals as the endpoint of a cascade of pairwise collisions. When two of these objects collide they could both destroy each other or stick together. Thanks to the strong gravity we can assume that most of the mass of two colliding bodies ends up agglomerating into a single larger object. Moreover, the cross section is enhanced by the gravity of the bodies in an effect called *gravitational focusing*. Indeed, a massive planet will deflect the trajectories of other bodies toward it and, as a result, has a collisional cross-section that is much larger than its physical one. Instead for smaller bodies with large impact velocities the assumption of perfect accretion can fail. In this case we have to take into account the strength of the bodies explicitly to determine whether collisions lead to agglomeration or fragmentation.
When many planetesimals have succeed in forming a unique body, this latter, once large enough, will gravitationally attract smaller objects enhancing further its mass. We first estimate the radius within which the gravity of the protoplanet, with mass M_p and orbital radius a_p, dominates over the stellar tidal field, which is given by the radius of the *Hill sphere*

$$r_H = \left(\frac{M_p}{3M_*}\right)^{1/3} a_p. \tag{2.11}$$

Particles on near circular orbits that pass more than a few r_H from the protoplanet are essentially unperturbed by the presence of the protoplanet and will not collide. Even particles that are on orbits that are too close in radius to the protoplanet fail to enter the Hill sphere and do not contribute to accretion because they follow what are referred to as horseshoe (or tadpole) orbits. Therefore, the perturbation from the protoplanet is able to bring the test particle into the region where a collision can occur only for a range of intermediate separations.
When two solid bodies, called the impactor that is the smaller one and the target that is the most massive one, physically collide the result of the collision can be divided into three different categories:

- *Accretion*, in which all or most of the mass of the impactor becomes part of the final body, which remains solid. Small fragments may be ejected, but overall there is net growth;
- *Shattering*, in which the impact breaks up the target body into a number of pieces, but these pieces remain part of a single body (perhaps after accumulating gravitationally). The structure of the shattered object resembles that of a rubble pile;
- *Dispersal*, in which the impact fragments the target into two or more pieces that do not remain bound.

To delineate the boundaries between these regimes quantitatively, we consider an impactor of mass m colliding with a larger body of mass M at velocity v. We define the specific energy Q that will tell us in which regimes the collision is. Q is given by

$$Q = \frac{mv^2}{2M}, \tag{2.12}$$

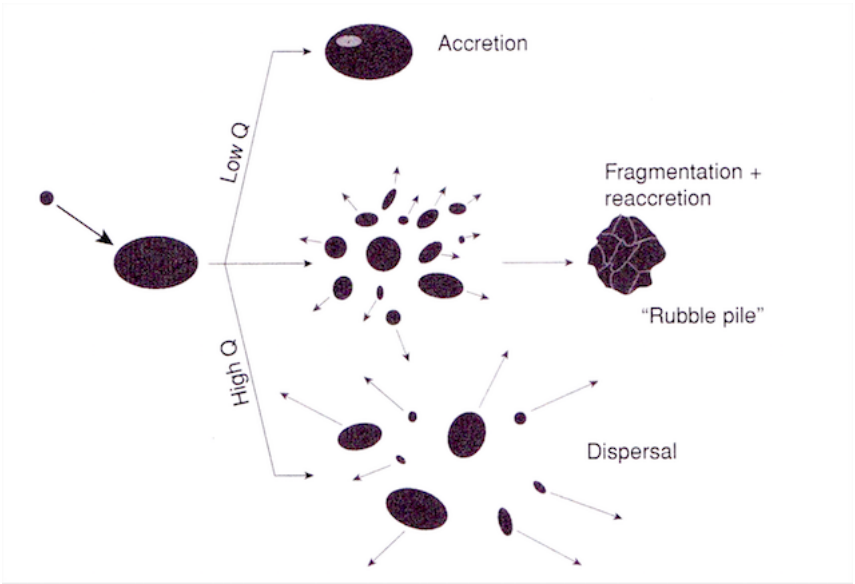

Figure 2.2: Three different results of collision between two bodies. Credits: [1]

Conventionally, we define the threshold for catastrophic disruption Q_D^* as the minimum specific energy needed to disperse the target in two or more pieces, with the largest one having a mass of $M/2$. Similarly Q_S^* is the threshold for shattering the body. More work is required to disperse a body than to shatter it, so evidently $Q_D^* > Q_S^*$. It is worth keeping in mind that the outcome of a particular collision will depend upon many factors, including the mass ratio between the target and the impactor, the angle of impact, the shape and rotation rate of the bodies involved.

We can summarize the steps before the final assembly in the terrestrial planet zone in two main phases: a first runaway growth of a limited number of quite small bodies caused by the combined influence of dynamical friction and gravitational focusing. Indeed, since there are no large bodies, the velocities of planetesimals are set by viscous stirring among planetesimals themselves and damping via gas drag. A second oligarchic growth, that starts when the rate of viscous stirring by means of the largest bodies first exceeds the rate of self-stirring among the planetesimals. The resulting boost in the strength of viscous stirring increases the equilibrium values of planetesimals eccentricity and inclination, partially limiting the gravitationally enhanced cross-section of the protoplanets. In this regime the growth of these newly formed large objects continues to outrun that of planetesimals, but the dominance is local rather than global. Across the disk many oligarchs grow at similar rates by consuming planetesimals within their own largely independent feeding zones.

Initial stages of terrestrial planet formation are rapid (0.01 Myr-1 Myr) and result in the formation of 10^2 to 10^3 large bodies across the terrestrial planets zone. These massive objects of 10^{-2} $M_\oplus$ to 0.1 $M_\oplus$, comparable to the mass of the Moon or Mercury, are not yet terrestrial planet. The final assembly of terrestrial planets starts once the oligarchs have depleted the planetesimal disk to the point that dynamical friction can no longer maintain low eccentricities

and inclinations of the oligarchs. Beyond this point the assumption that each oligarch grows in isolation breaks down, and the largest bodies start to interact strongly, collide, and scatter smaller bodies across a significant radial extent of the disk, continuing out to at last 10 Myr. Recent calculations suggest that the typical outcome of terrestrial planet formation varies depending upon the surface density of the planetesimal disk- higher Σ_p typically yields a smaller number of more massive planets.

2.4 Giant planets

We know from direct experience of our Solar System that other kind of planets different from terrestrial ones do exist. We group them under the class of giant planets, since they are much more massive than rocky planets and are characterize by a conspicuous gaseous envelope. Therefore, in order to understand the formation process of such planets we have once again to compare gas and solid components in the protoplanetary disk.
Two different theories have been proposed to account for the formation of massive gaseous planets. The first one is the *core accretion theory* which consists in the acquisition of massive envelope of gas as the final step of a mechanism that starts with the formation of a core of rock and ice via successive pairwise collisions (see paragraph 2.3). The core accretion model then is based on one fundamental assumption: the rocky core has to grow rapidly enough so that it can exceed a certain critical mass prior to the dissipation of the gas in the disk. If this condition is satisfied, the core triggers a hydrodynamic instability that causes large quantities of gas to accrete on to the core. Since the critical core mass is typically of the order of 10 $M_\oplus$, the end result is a largely gaseous planet that at least qualitatively resembles Jupiter or Saturn. In order to derive the time scale for giant planet formation in core accretion model we have to know how quickly the core can be assembled and how rapidly the gas in the envelope can cool and accrete on to the core.
The other theory is called *disk instability theory* and instead proposes that giant planets form promptly via the gravitational fragmentation of an unstable protoplanetary disk. This is a gaseous analog of the Goldreich-Ward mechanism for planetesimals formation, whereas in this model the solid component plays only an indirect role in the process of planet formation. The disk instability model is based on the assumption that the gaseous protoplanetary disk is massive enough to be subjected to instabilities arising from its own self-gravity, and so that the outcome is a fragmentation into massive planets. Moreover, in order to achieve such fragmented configuration, it is required that the disk is able to cool on a relatively short time scale, and whether these conditions are realized within disks is the main theoretical issue that remains unresolved.
Even if these two models are presented in contrast, there is no physical reason why they should be mutual exclusive. Rather it seems that it depends on the single case of the system under analysis. Purely theoretical considerations do not give an unambiguous answer as to whether giant planets can form from disk instability, and they also fail to specify which of the many possible variants of core accretion is most commonly realized in real systems.

2.5 Early planetary systems

Once terrestrial and giant planets have formed, they can interact with the surrounding environment or with each other during close encounters and determine the stability/instability and the dynamical evolution of the newly formed planetary system.
For example, from classical theories of giant planet formation (see paragraph 2.4) we would expect that massive planets move on approximately circular orbits, with a strong preference to form in the outer disk at a few AU from the star or beyond. However, unlike the planets of the Solar System, many known extrasolar giant planets are very close to the star (Hot Jupiter) and/or have very pronounced eccentricities. We have to look for other kinds of mechanism in order to describe these observed extrasolar planetary systems properties.
The common feature of all these mechanisms is an exchange between energy and angular momentum either among newly formed planets, or between planets and leftover solid or gaseous debris in the system.
For what concerns exchange of angular momentum between the planet and the surrounding gaseous protoplanetary disk, the result is a migration of the planet that changes its semi-major axis. Such exchange is mediated by gravitational torques between the planet and the disk. No torque is exerted on a planet by an axisymmetric disk, so gas disk migration can only take place if the planet excites non axisymmetric structure. In addition to angular momentum, energy is also exchanged between the planet and the disk. Therefore, the net result may be changes not just in semi-major axis a_p but also in eccentricity e_p and inclination angle i with respect to the plane of the disk.
We can have two different kinds of interactions between planet and gas: if the orbit of the planet is interior to the gas, they interact in such a way that the orbit increases the angular momentum of the gas, and decreases the angular momentum of the planet. Thus, the planet will tend to migrate inward, and the gas will be repelled from the planet. On the other hand, if the gas is interior to the orbit of the planet, the orbit decreases the angular momentum of the gas and increases that of the planet. In this scenario the interior gas is also repelled, but the planet tends to migrate outward.
In the common circumstance where there is gas both interior and exterior to the orbit of the planet, the net torque (and sense of migration) will evidently depend upon which of the above effects dominates.
Migration is potentially important whenever a fully formed planet co-exists with a gaseous disk, and so it is a very important effect for newly formed gas giants and for cores of giant planets forming via core accretion. On the other hand, for terrestrial planets the gas disk is assumed to have dissipated prior to their final assembly, then most likely fully formed rocky planets never interact with a significant amount of gas. Accordingly migration is often ignored in studies of terrestrial planet formation. The only different scenario is the one in which terrestrial planet formation occurs more rapidly, and in this case we can not exclude that gas disk migration may occur.
We can distinguish between two types of migration:

- *Type 1 migration* occurs for low-mass planets whose interaction with the disk is weak enough to leave the disk structure almost unperturbed. This will certainly be true if the local exchange of angular momentum between

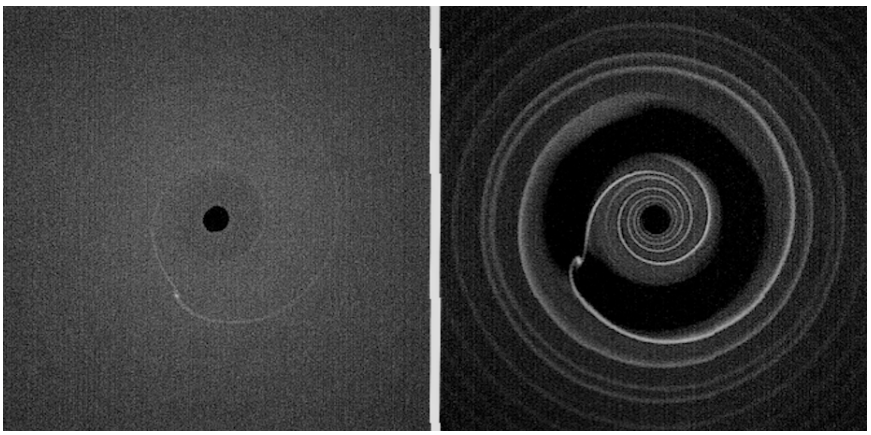

Figure 2.3: Interaction between the planet and protoplanetary disk for Type 1 (left) and Type 2 (right) regimes. Credits: [1]

the planet and the disk is negligible compared to the redistribution of angular momentum due to disk viscosity. Thus, the planet remains fully embedded within the gas disk. In this regime the net torque scales as M_p^2, while the orbital angular momentum of the planet is directly proportional to the mass. The migration time scale is thus inversely proportional to mass, so that more massive planets migrate faster.

- *Type 2 migration* occurs for higher mass planets whose gravitational torques locally dominate angular momentum transport within the disk. As we have already noted, gravitational torques exerted by the planet act to repel disk gas away from its orbit, so in this regime the planet opens an annular gap within which the disk surface density is reduced compared to its unperturbed value. For Type 2 the nominal migration time scale is independent of mass and it is determined instead by the angular momentum transport properties of the disk.

The most rapid migration is predicted to occur at the boundary between the Type 1 and Type 2 regimes. For typical disk models this corresponds to planet masses of the order of 0.1 M_J.
Let us now analyze exchange of energy and angular momentum that do not involve the gas component. The first effect we outline is that of resonances between two or more planets or between planets and solid leftover particles of the disk. A resonance occurs when there is a near-exact commensurability among the characteristic frequencies of one or more bodies. The condition for resonance between two planets can be written as

$$\frac{P_{in}}{P_{out}} = \frac{p}{p+q} \tag{2.13}$$

where P_{in} and P_{out} are the orbital periods of the two planets and p and q are integers. We first assume that the planets are in exact resonance. We can define $n = 2\pi/P$, such that

$$\frac{n_{out}}{n_{in}} = \frac{p}{p+q}. \tag{2.14}$$

If we can ignore any perturbation between the planets, the angle λ between the radius vector to one of the planets and a reference direction advances linearly with time. Defining $t = 0$ and $\lambda = 0$ to coincide with a moment when the two planets are in conjunction, we have

$$\lambda_{in} = n_{in}t \tag{2.15}$$

$$\lambda_{out} = n_{out}t, \tag{2.16}$$

and resonance condition becomes

$$(p + q)\lambda_{out} = p\lambda_{in}. \tag{2.17}$$

We can define a resonant argument

$$\theta = (p + q)\lambda_{out} - p\lambda_{in}, \tag{2.18}$$

which will evidently remain zero for all time if the planets are in exact resonance. For planets on general circular orbits λ_{in} and λ_{out} still advance linearly with time, but no small p and q can be found so that θ remains constant. We can then identify a resonance when θ assumes one or more bounded values, while there is no resonance if the θ assumes all possible values in the range $[0, 2\pi]$.
If we consider restricted three bodies problem the system is in resonance if θ librates, thus the resonant argument may be time-dependent but varies only across some limited range of angles. Instead it is out of resonance if θ circulates, taking on all values between 0 and 2π.
Since resonances have finite widths, there is some probability that two planets in a randomly assembled planetary system will happen to find themselves in a mean motion resonance. For example, 20% of Kuiper Belt Objects with well-determined orbits are in mean motion resonances with Neptune, with $3 : 2$ resonance occupied by Pluto being the most heavily populated. Among satellites too there are numerous known resonances, of which the most striking is the $4 : 2 : 1$ resonance that involves three of the Galilean satellites of Jupiter (Io, Europa and Ganymede). Mean motion resonances between planets themselves also appear to be common among extrasolar planetary systems.
There is no evidence to suggest that planets in the Solar System experienced close encounters with each other in the past, or that the early Solar System harbored additional planets that have subsequently been lost through collisions or ejections. However, thanks to some perturbed regions of the Kuiper belt scientists have postulated the presence of a ninth planet. This object would orbit the Sun at distances much grater than Neptune and it is supposed to be on a high eccentric orbit. Many hypothesis have been made to justify its orbital parameters, as for example the ejection of another planet via planet-planet scattering with the Ninth planet, even if the most quoted assumption is that our Solar System stole this object from another planetary system during a close encounter with the other star.
Therefore, with the exception of the eventual Ninth planet, the lives and evolutions through times of the planets in our Solar System seem to be quite quiet and the primary motivation for studying the evolution of unstable planetary systems comes mostly from extrasolar ones whose typically eccentric orbits immediately suggest that the observed planets may be survivors of violent planet-planet scattering events that occurred early on.

In general, an initially unstable planetary system can evolve ("relax") via four distinct channels:

- one or more planets are ejected, either as a result of a close encounter between planets or via numerous weaker perturbations;
- one or more planets have their semi-major axis and eccentricity changed in such a way that the system becomes stable;
- two planets physically collide and merge;
- one or more planets impact the star;

Once the system becomes stable, it will stay so and the only changes are due to later evolution of the star or encounters with other systems. However, it could takes very long for a planetary system to reach the stability and for this reason it becomes quite difficult to estimate if an observed one will evolve further.

Chapter 3

Debris disk

Once a planetary system gets older and older, its elements, such as planets and planetesimals, evolve toward a stable configuration. The preliminary step that we can do to guess possible architectures of exoplanetary systems is obviously a survey of our own Solar System: eight known planets (maybe a ninth one) are arranged into two groups, four terrestrial ones and four giants; the main asteroid belt between two groups of planets, terrestrial and giant ones, at ~ 3 AU is made of planetesimals that had failed to grow to planets because of the strong perturbations of Jupiter; and the Edgeworth-Kuiper belt exterior to Neptune orbits at ~ 30 AU, made of planetesimals that did not grow further because of the low density of the outer solar nebula. Both the asteroid and the Kuiper belt are evidently sculptured by planets, predominantly by Jupiter and Neptune respectively.
The interesting question is thus if our solar system is special for its complex architecture or if it has common features that can be found in extrasolar systems. From a theoretical point of view, at the end of the protoplanetary phase a star is expected to be possibly surrounded by different components such as planets (from sub-Earth to super-Jupiter sizes), dust and gas from the protoplanetary disk itself, planetesimal belts in which growth or collisional mechanisms may go on generating larger bodies or dust, respectively. Objects of planetesimals dimension down to dust dimension form a single structure called *debris disk*, that thus covers all the size range from μm to tens of km. And, indeed, beyond the theory we have prove both of the presence of planets and debris disks. In particular, these latter can be revealed by observations of the thermal emission and stellar light scattered by the dust.
In this chapter we will focus on the debris components, on their characteristics and physical effects that act on such objects. Indeed, even in mature systems where the planet formation has long been completed, debris disks continue to evolve collisionally and dynamically, are gravitationally sculptured by planets, and the dust produced by planetesimals through collisional cascades responds sensitively to electromagnetic and corpuscolar radiation of the central star. For a deeper and more complete treatment of debris disks see [17], [9].

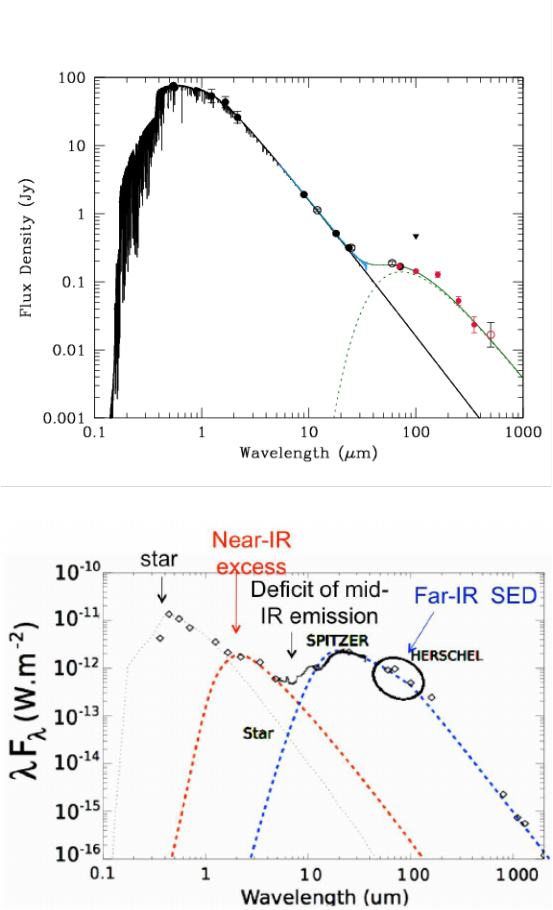

Figure 3.1: Spectral energy distribution for γ Doradus (up) and HD139614 (down). It is clearly visible the excess in the far IR in both cases. The SED of γ Doradus was modeled using two blackbodies: one associated with the star and the other with the excess in the far infrared. This latter peaks around 70 μm thus it indicates the presence of a cold debris disk. The SED of HD139614, instead, was modeled with two different blackbody temperatures to represent the excess in the IR, one in the near IR for the warm component ($T \sim 1000K$) and the other in the mid IR for the cold component ($T \sim 200 - 400K$). Credits [10] and [3]

3.1 Observational methods

An efficient way of detecting circumstellar dust is the infrared photometry. If dust is present around a star, it comes to a thermal equilibrium with the stellar radiation. Since equilibrium temperatures of dust orbiting a solar-type star at several tens of AU are typically several tens of Kelvin, using a black-body model (see paragraph 3.4) we can deduce that dust re-emits the absorbed stellar light at wavelengths of several tens of micrometers, i.e. from the mid IR to the far IR,

depending on the distance from the star and on the compositions of the particles. As a result, the dust IR emission flux may exceed the stellar photospheric flux at the same wavelength by two-three orders of magnitude, producing visible peaks in the spectral energy distribution of the star. Observations were done mostly between $\sim 25\ \mu m$ and $\sim 100\ \mu m$ with instruments like MIPS photometer (it works principally at 40 μm and at 70 μm) or the more recent WISE instrument. We show two examples of systems with excess in the infrared in

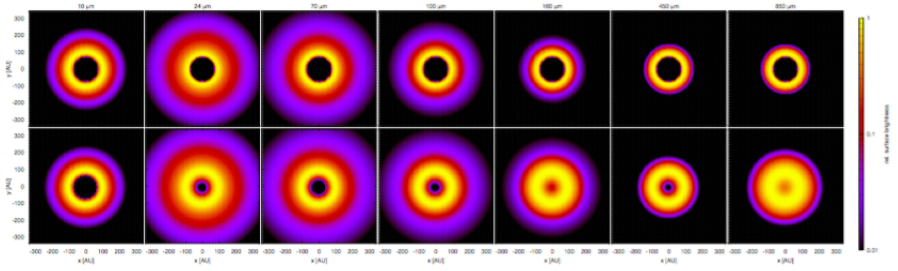

Figure 3.2: Appearance of a debris disk at different wavelengths from 10 to 850 μm. On the top row the Vega's debris disk is represented using theoretical models whereas in the bottom row it has been convolved with a Gaussian Point Spread Function (PSF). Credits [9]

figure 3.1.
Another illuminating observational technique to reveal debris disk is direct imaging. This method, as its name suggests, furnishes a direct insight of the system since it provides spatially resolved images of it at various wavelengths, from visual through mid and far infrared to sub-mm and radio. Obviously, the system will never be equal to itself when observed at different wavelengths, since each component emits at certain λ. We show an example of such situation in figure 3.2. Even if direct imaging is an extraordinary tool in order to characterize debris disks, the informations that provides are often affected by large uncertainties. For example, some instruments use angular differential rotation fields that tend to erase all the homogenous contributions while underline edges, clumps etc. (an homogenous face-on disk would be completely invisible if analyzed in this way). In the far infrared, instead, the images are obtained by means of point spread functions (PSF) so that it is important to choose the most suitable one in order to avoid large errors.
In order to have a more complete view of direct imaging technique we refer to paragraph 4.2 in which we describe this method for the research of exoplanets.

3.2 Forces acting on debris disks particles

Every debris disk is composed of solids that belong to a huge range of sizes, from hundreds of kilometers bodies (large planetesimals) down to a fraction of micrometer particles (fine dust). These objects orbit the central star and the largest ones may interact with each other trough collisions. The force that keeps a planetesimal or a dust grain on a closed orbit is the central star's gravity, given

by

$$\mathbf{F_g} = -\frac{GM_*m}{r^3}\mathbf{r}, \tag{3.1}$$

where G is the gravitational constant, M_* the stellar mass, $\mathbf{r}$ the radius vector from the star to the object and m its mass. We neglect the contribution to the gravitational force due to the presence of planets in the system and mutual gravitational interactions between objects in the debris disk. At dust sizes ($s \leq 1$ mm), solids feel another force that is the radiation pressure caused by the central star. Like stellar gravity, radiation pressure scales as the reciprocal of the square distance from the star, but is directed outward on the contrary of the gravitational force. For a dust particle at rest, the radiation force exerted by the stellar photons on the particle is given by

$$\mathbf{F_{rad}} = \frac{S}{h\nu}\frac{h\nu}{c}Q_{pr}A\hat{\mathbf{r}} \tag{3.2}$$

where $S/(h\nu)$ is the flux of incoming photons, $h\nu/c$ is the momentum per photon and $Q_{pr}A$ is the particle cross section for radiation pressure. Moreover, A is the particle geometric cross section $A = \pi s^2$ and Q_{pr}, expressed as a function of the grain optical properties (size, shape and chemical composition), is the dimensionless radiation pressure factor averaged over the stellar spectrum that gives the fraction of energy that is scattered and/or absorbed by the grains. Q_{pr} takes values in the range $[0, 2]$, where 0 is for a perfect transmitter, whereas 2 for perfect backscatters. Substituting the expression for the energy flux density $S = \frac{L_*}{4\pi r^2}$, we can write

$$\mathbf{F_{rad}} = \frac{L_*Q_{pr}s^2}{4r^3c}\mathbf{r} \tag{3.3}$$

where L_* is the stellar luminosity, s is the particle radius and r is the heliocentric distance.
Thus the two forces can be combined into unique component that we can call *photogravitational force* given by

$$\mathbf{F_{pg}} = -\frac{GM_*(1-\beta)m}{r^3}\mathbf{r}. \tag{3.4}$$

β is the radiation pressure to gravity ratio and it depends on the grain size and optical properties. In order to have an expression for β we have to make some assumptions about the characteristics of the particles. The simplest guess is that of spherical and compact grains with radius s, bulk density ρ, and radiation pressure efficiency Q_{pr}. Taking in mind that an ideal absorber has a radiation pressure efficiency that equals unity we get

$$\beta = 0.574\frac{L_*}{L_\odot}\frac{M_\odot}{M_*}\frac{1gcm^{-3}}{\rho}\frac{1\mu m}{s} \tag{3.5}$$

where $L_*/L_\odot$ and $M_*/M_\odot$ are luminosity and mass of the star in solar units.
If smaller grains are released from larger bodies due to fragmentation or erosive processes, the radiation force becomes important and the particles feel a photogravitational force instead of the only gravitational one experienced by larger objects. Moreover, the smaller the grains, the more the radiation pressure they experienced compensates the central star's gravity. Thus the orbits

of small particles differ from those of their parent bodies. For example, let us take a parent body on a circular orbit from which a small particles is release at a certain time. The fragments will move on a bound elliptic orbit (thus with larger semi-major axis and eccentricity with respect to the large particles) for values of β up to 0.5; otherwise if $0.5 < \beta < 1$, the grain possible orbits will be hyperbolic and thus unbound.
Instead, for parent bodies in elliptic orbits, the boundaries between bound and unbound orbits of dust particles are not so clearly defined, because they depend on the ejection point. However we can say that all grains with $\beta < 1$ will orbit the star on Keplerian trajectories at velocities reduced by a factor $\sqrt{1-\beta}$ compared to macroscopic bodies, whereas below the critical size for which $\beta \geq 1$ the effective force is repelling more than attractive, and the grains will move on anomalous hyperbolic orbits.
The derivation of the photogravitational force described above was merely from a classical point of view. A more accurate derivation can be done taking into account special relativity that leads to an additional velocity-dependent term to be added in the right-hand side of equation (3.4), to give the so called *Poynting-Robertson force*

$$\mathbf{F_{PR}} = -\frac{GM_*\beta m}{r^2}\Big[\Big(\frac{\mathbf{vr}}{cr}\Big)\frac{\mathbf{r}}{r} + \frac{\mathbf{v}}{c}\Big], \tag{3.6}$$

with $\mathbf{v}$ being the velocity vector of the particle. The last term is the relativistic contribution mentioned above and it can be explained in the following way: in the reference frame of the particle, the stellar radiation appears to come at a small angle forward from the radial direction (due to aberration of light) that results in a force with a component against the direction of motion; on the other hand, in the reference frame of the star, the radiation appears to come from the radial direction, but the particle reemits more momentum into the forward direction due to the photons blueshifted by the Doppler effect, resulting in a drag force. Being dissipative, this new expression for the force causes a particle to lose gradually its orbital energy and angular momentum. On timescales of thousand of years or more trajectories shrink to the star.
Another interesting effect that generates a force acting on dust particles is due to stellar wind (the stellar particulate radiation). Similarly to the net radiation pressure force, the total stellar wind force can be decomposed to direct stellar wind pressure and stellar wind drag. For most of the stars, the momentum and energy flux carried by the stellar wind are by several orders of magnitude smaller than that carried by the stellar photons, so that the direct stellar wind pressure is negligibly small. However, the stellar wind drag forces cannot be ignored because the stellar wind velocity v_{sw}, to replace c in equation (3.6), is much smaller than c. Stellar wind forces can be very important in debris disk around late-type stars.

3.3 Collisional processes

Since dust in planetary systems has a short life, a debris disks must produce fresh debris continuously, so that destructive collisions have to be a dominant process operating in these systems. For collisions to be destructive and to occur at sufficient rates, a certain minimum level of relative velocities is then necessary. In protoplanetary disks relative velocities are strongly damped by a great amount

of still present gas, so that all the orbits have low eccentricities and inclinations that inhibit collisions. In contrast, debris disk are gas-poor, and damping is not efficient at all. However, even if the absence of damping is necessary, it is not sufficient for relative velocities to be high. As a protoplanetary disk gets elder, transforming itself into a debris disk, solids are expected to preserve the low velocities dispersions they had before the gas removal. Accordingly, to let the destructive collisions phase started, debris disks must be stirred by some mechanism. These can be actuated by the largest planetesimals (self-stirring) or by stirring by planets orbiting in the inner gap of the disk. Further possibilities, which however are quite unusual, include fast ignition by the sudden injection of a planet into the disk after planet-planet scattering or external events such as stellar flybys.
Once the disk is sufficiently stirred, the collisional cascade sets in. The material is ground all the way down to dust sizes, until the smallest fragments with $\beta \geq 0.5$ are blown away from the disk by radiation pressure (see paragraph 3.2). Note that at dust sizes, stirring is no longer required because the typical eccentricities of grains are of the same order of their β-ratio so that radiation pressure ensures the impact velocities to be sufficiently high.
Since particles of different sizes are affected differently by the forces that act on the system, we expect to find a spatial distribution depending on s to describe a debris disk. The size distribution most commonly adopted for debris dust is

$$n(s) \sim s^{-q} ds, \tag{3.7}$$

with $q = 3.5$ the most suitable value. It results from considering the system as subjected to a collisional cascade, assuming that the strength of the particle does not depend on the target size (even if, actually, it does), and a quasi-steady state, i.e. the same amount of mass that enters one size bin as larger particles break down, leaves the size bin as the particles continue to break in smaller pieces. Obviously, the bins at the two extremes would not be in a steady state and the reservoir of large particles would get depleted with time.
If we take different values of the power law index q in equation (3.7) we can take into account debris disks with different characteristics. For example, for $q = 3.5$, we would get a system where the mass is dominated by the large grains whereas the cross-section is dominated by the small ones. Instead, in a size distribution with $q = 3$, we would obtain a debris disk in which each size bin will contain an equal amount of cross-section area, while for $q = 4$, each size bin will contain an equal amount of mass.
We now take a more quantitative look at collisional mechanisms. An important parameter in the collisional prescription is the critical specific energy for disruption and dispersal, Q_D^*. It is defined as the impact energy per unit target mass that results in the largest remnant containing a half of the original target mass. For small objects, Q_D^* is determined solely by the strength of the material, while for objects larger than $\sim 100m$, the gravitational binding energy dominates. As a result, Q_D^* is commonly described by the sum of two power laws

$$Q_D^* = Q_s \Big(\frac{s}{1m}\Big)^{-b_s} + Q_g \Big(\frac{s}{1km}\Big)^{b_g}, \tag{3.8}$$

where the subscript s stands for strength regime and g for gravity one. The values of Q_s and Q_g lie in the range $\sim 10^5 - 10^7\ erg/g$, b_s is between 0 and 0.5,

and b_g between 1 and 2. The critical energy Q_D^* reaches a minimum ($\sim 10^4 - 10^6$ erg/g) at sub-km sizes. At dust sizes, equation (3.8) suggests $Q_D^* \sim 10^8$ $ergg^{-1}$, but true value remains unknown because this size regime has never been proved experimentally.
We can also link the specific energy Q_D^* with the relative velocity between particles. Indeed, when two particles collide, they are both disrupted if their relative velocity v_{rel} exceeds

$$v_{cr} = \sqrt{\frac{2(m_t + m_p)^2}{m_t m_p} Q_D^*} \tag{3.9}$$

where m_t and m_p are the masses of the two colliders. Thus two objects with the same size (i.e. with the same mass if we assume that they are composed of the same material) will be destroyed if they collide at a speed exceeding $\sqrt{8Q_D^*}$. For two dust grains, for example, the critical speed is several hundreds of m/s and if we consider a distance of several tens of AU from a star, this would imply eccentricities of ~ 0.1 or higher. Such eccentricities can be easily reached by dust grains with $\beta \sim 0.1$ as result of the radiation pressure effect described above.
The size distribution of debris disks with power-law index $q = 3.5$ needs very restrictive assumptions that can be relaxed taking into account much more realistic phenomena such as a size-dependent particles strength, the removal of the smallest particles by radiation pressure and the effect of collisions with grains coming from the inner regions on highly eccentric orbits. In fact, the actual physics of collisions in debris disks is much more complicated than the description we gave above. Collisions occur across a size range that is ~ 12 orders of magnitude wide and at quite different velocities. Statistically, collisions between objects of very dissimilar sizes outnumber those between like-sized objects and they are more likely to occur by oblique impacts instead of frontal ones. All this leads to a spectrum of possible collisional outcomes that take place simultaneously in the same disk, comprising further growth of large planetesimals, partial destruction (cratering) of one or both projectiles with or without accumulation of fragments, as well as a complete disruption of small planetesimals and dust particles. It is enough clear how difficult and complicated is a complete treatment of collisions in such systems. Moreover, the steady scenario mentioned above cannot be sustained for an indefinite period of time because the reservoir of large particles that feeds the collisional cascade gets depleted, resulting in a decay of the amount of dust in the system. In the simplest scenario, the dust is derived from the grinding down of planetesimals, the planetesimals are destroyed after one collision and the number of collisions is proportional to the square of the number of planetesimals, N. In this case, $\frac{dN}{dt} \propto N^2$ and $N \propto 1/t$. In a collisional cascade, the dust production rate, R_{prod}, would be proportional to the loss rate of planetesimals times a proportionality constant,

$$R_{prod} = C \frac{dN}{dt} \left(\frac{s_d}{s_p}\right)^{-3.5} \tag{3.10}$$

where s_d and s_p are the sizes of dust and parent bodies, respectively. In this scenario, s_d/s_p is independent of time and one gets $R_{prod} \propto \frac{dN}{dt} \propto N^2 \propto 1/t^2$.
We can solve for the amount of dust in the disk in steady state by equating the dust production rate to the dust loss rate, R_{loss}. Depending on the number

density of dust, n, there are two different solutions. The first one is for low number density of dust particles and, in this case, the disk is in the regime where the dust loss rate is determined by P-R drag (thus, calling t_c is the collisional timescale and t_{pr} the P-R timescale, we get $t_c > t_{pr}$). With this assumption the dust loss rate is proportional to the number density of particles, $R_{loss} \propto n$, and from $R_{prod} = R_{loss}$ one gets $n \propto 1/t^2$. If instead the number density of dust is high, the disk is in the collision-dominated regime, where the main dust removal process is grain-grain collisions ($t_c < t_{pr}$). In this case, the dust loss rate is given by $R_{loss} \propto n^2$, and from $R_{prod} = R_{loss}$ one gets $n \propto 1/t$, i.e. both the dust mass and the number of parent bodies (and therefore the total disk mass) decay as $1/t$ with a characteristic timescale that is inversely proportional to the initial disk mass.

3.4 Modelling debris disk

As already discussed in previous paragraphs, each debris disk can be treated as a collection of objects of different sizes (from dust to planetesimals) that orbit the star under the influence of gravity, radiation pressure and other forces. In addition, they experience collisions which destroy or erode these objects and produce new ones. Such a system can be modeled by a variety of methods that can be classified into three major groups: N-body simulations, statistical approach and hybrid methods.
N-body codes follow trajectories of individual disk objects by numerically integrating their equations of motion. During numerical integrations, instantaneous positions and velocities of particles are stored. Assuming that the objects are produced and lost at constant rates, this allows us to calculate a steady state spatial distribution of particles in the disk. Then, collisional velocities and rates can be computed and collisions can be applied. It is usually assumed that each pair of objects that come in contact at sufficiently high relative velocity is eliminated from the system without generating smaller fragments or producing a certain number of fragments of equal size. The N-body simulations are able to handle an arbitrary large ensemble of forces and complex dynamical behaviors of disk solids driven by these forces. Therefore, such method is the best one to study structures in debris disk arising from interactions with planets, ambient gas or interstellar medium. However, with N-body codes we can not treat a large number of objects sufficient to cover a wide range of particle masses and thus is less successful in modeling, for example, the collisional cascade. Particularly, an accurate characterization of the size distribution with N-body codes is hardly possible.
Statistical method effectively replaces particles themselves with their distribution functions in an appropriate phase space, associating at each ensemble of objects the velocities as obtained from Boltzmann equation and the mass (or size) distribution as given by the coagulation equation.
On the midway between the these two methods are hybrid codes that combine N-body integrations of a few large bodies (planets, planetary embryos, biggest planetesimals) with a statistical simulation of numerous small planetesimals and dust.
The straightest way (even if not much realistic) to describe a debris disk, however, is, as alway, to make very simple assumptions and then obtain analytical

formulations. A standard model of a debris disk can be derived considering two major effects, stellar photogravity and collisions, and neglecting drag forces and all other processes. Imagine a relatively narrow belt of planetesimals (the so called "parent ring" or "birth ring") in orbits with moderate eccentricities and inclinations, exemplified by the classical Kuiper belt in the Solar System. The planetesimals moving in the birth ring collide with each other grinding the larger solids down to dust. At smallest dust sizes, stellar radiation pressure effectively reduces the gravitational effect of the mass of the central star and sends the grains into more eccentric orbits, with their pericenters still residing within the birth ring while their apocenters are located outside the ring. As a result, the dust disk extends outward from the planetesimal belt. The smaller the grains, the more extended their partial disk. The tiniest dust grains, for which the radiation pressure effectively reduces the physical mass by half, are blown out of the system in hyperbolic orbits. The radiation pressure blowout of the smallest collisional debris represents the main mass loss channel in such a disk.

We would like to find a scenario in which the production of dust by collisional cascades is equal to losses of small particles due to radiation pressure blowout. If such an equilibrium does exist, the amounts of particles with different sizes on different orbits stay constant relative to each other, and the debris disk is said to be in a quasi-steady state. However, the absolute amounts should decrease with time, because the material at the top and at the end of the size distribution is not replenished (therefore "quasi"). For brevity, "quasi" is often omitted and steady state is used.

The steady state evolutionary regime can be perturbed, for instance, by occasional collisional break-ups of largest planetesimals or by shake-down of the system due to instability of nearby planets. After such events, the disk needs some time to relax to a new steady state.

The standard model just described is only valid if the collisional timescale is shorter than the characteristic timescale of the drag forces ($t_c < t_d$), so that we can neglect these latter. If this is the case, at dust sizes we will say that the disk is collision dominated whereas, if $t_c > t_d$, the disk will be in the transport regime and we get radial migration of dust material. Thus, additional removal mechanisms may play a significant role. For example, P-R drag can bring grains close to the star where they would sublimate or deliver them into the planetary region where they would be scattered by planets. To be transport dominated, the system should either have an optical depth below current detection limits or be subjected to transport mechanisms other than P-R drag, such as strong stellar winds (typical around late type stars). Most of debris disks detected so far are thought to be collision dominated and transport dominated systems will be not treated. Moreover, at sufficiently large particles sizes, all disks are dominated by collisions. This is because the lifetime against catastrophic collision in a disk with the $s^{-3.5}$ size distribution scales as $\propto \sqrt{s}$, whereas any drag force is proportional to the ratio of the mass and cross section, i.e. $\propto s$.

We want now give some simple instruments and argumentations (that will be use massively in the following analysis) in order to convert observations of debris disks into quantitative informations about its components. Indeed, if we could resolve a debris disk by direct imaging methods we will obtain that at different wavelengths the appearance of the disk look quite different (as mentioned in paragraph 3.1). How to explain such a peculiar fact? The answer regards the

tight bound between the size of the particles and their temperatures. Measurements at longer wavelengths (sub-mm) probe larger grains, because they are cooler and thus trace the parent ring. At shorter wavelengths (far-IR, mid-IR), instead, smaller and so warmer grains are probed and thus the same disk appears much larger. At sub-mm wavelengths the disk may reveal clumps, if for instance there is a planet just interior to the inner edge of the parent ring, and planetesimals and their debris are trapped in external resonances. However, at shorter wavelengths such features are not present because strong radiation pressure and non-negligible relative velocities would liberate small particles from resonance. As a result, they would form an extended disk regardless of wether their parent bodies are resonant or not. Finally, at shortest wavelengths of thermal emission, only the hottest closest-in grains are evident in the observations, and thus again only the parent ring is seen.
Beyond direct imaging, the other powerful instrument that we have to detect the presence of a debris disk is the analysis of the spectral energy distribution (SED) of the star. In fact, if a debris disk does exist we expect to find a peculiar excess in the IR wavelengths that will deviate from the quasi-blackbody spectrum of the star that peaks in the visible (see paragraph 3.1 and figure 3.1). We are in the most simple case when photometric points indicative of the IR excess can be fitted with a spectral energy distribution (SED) of a blackbody with a single temperature. Two useful quantities that can be derived from such fitting are the dust temperature T_d and the dust fractional luminosity f_d, defined as the ratio of the bolometric luminosities of the dust and the star. Both T_d and f_d can be estimated from the wavelength where the dust emission flux peaks, $\lambda_{d,max}$, and from the maximum stellar radiation flux, $F_{d,max}$. If dust behaves as a blackbody, Wien's displacement law gives

$$T_d = 5100K\Big(\frac{1\mu m}{\lambda_{d,max}}\Big) \tag{3.11}$$

Assuming that also the stellar photosphere emits as a blackbody, it is straightforward to find

$$f_d = \frac{F_{d,max}}{F^*_{max}}\frac{\lambda_{d,max}}{\lambda^*_{max}} \tag{3.12}$$

where λ^*_{max} and F^*_{max} are the wavelength at which the stellar radiation flux has a maximum and the maximum flux itself, respectively. A more accurate method to determine f_d that does not imply any blackbody assumption is using its definition: one calculates the bolometric dust luminosity from the SED, uses the bolometric luminosity of the star from catalogs, and take their ratio.
Keeping the assumption that the dust interacts with the stellar radiation as a blackbody and making some assumptions about the disk geometry, a number of further useful physical parameters can be derived from T_d and f_d. For instance, assuming the disk to be a narrow ring between $r-dr$ and $r+dr$, dust temperature gives the distance from the star

$$r = \Big(\frac{278K}{T_d}\Big)^2\Big(\frac{L_*}{L_\odot}\Big)^{0.5}, \tag{3.13}$$

whereas f_d is directly related to the total cross-section area of dust, σ_d, by

$$\sigma_d = 4\pi r^2 f_d, \tag{3.14}$$

and to the normal geometrical optical depth, $\tau_\perp$, by

$$\tau_\perp = (r/dr) f_d. \tag{3.15}$$

Dust mass M_d can be derived from fractional luminosity as well. However, this estimation requires further assumptions about the dust bulk density ρ_d and the typical dust size s_d (which is poorly defined, because f_d and M_d have different characteristic sizes). Then,

$$M_d = \frac{16}{3} \pi \rho_d s_d r^2 f_d. \tag{3.16}$$

More detailed analysis goes beyond the assumption of blackbody, confinement of dust to a narrow radial zone and dust grains of equal size. A usual and more accurate procedure is to assume for dust particles a given chemical composition, a radial distribution from r_{min} to r_{max} and a size distribution from s_{min} to s_{max}. Both distributions are usually postulated to be power laws. The limits and slopes of these latter laws are treated as free parameters, and their values are found by fitting the SED and, if available, the resolved images.
This procedure is very efficient even though it presents two problems. One is that relaxing the blackbody assumption we would get temperature dependent not only on dust location, but also on the particle sizes. Smaller grains at the same distance are warmer than larger ones. This leads to a fundamental degeneracy between distance and size, as the same SED can be produced equally well by a disk of smaller grains further out from the star or by a disk of larger particles closer in. One way to break this degeneracy is to invoke information from resolved images as they show where most of the emitting dust is located. The other problem of the fitting approach is that it roots in the assumption that radial and size distributions are both power laws, independent of each other. This is not what is expected from the debris disk physics from which, on the exact contrary, we may assume the size distribution to strongly depend on distance and conversely. Thus radial distribution can substantially depart from single power law.
Most of the systems have SED consistent with a single, radially narrow dust disk. The typical dust temperatures are of orders of several tens of Kelvin, which corresponds to dust disk located at several tens to hundred AU from the star. We can refer to them as "outer disks". Such distances readily suggest that the outer disks are likely produced by the Edgeworth-Kuiper belt analogs around those stars. There are also systems that cannot be explained with a single outer dust disk and are best fitted by two or more blackbody. Indeed, some stars show the presence of dust within $\sim$ 10 AU. The majority of such inner disks may be associated with collisionally evolving asteroid-like belt or sustained by the cometary activity. Yet closer-in to the central star, within 1 AU, the so called *exozodiacal clouds* have been detected with near-IR interferometry.

3.5 Debris disk evolution

The study of the frequency and properties of debris disks around stars of different ages can shed light on the evolution of debris disks with time. The main challenge in this case is that the ages of main sequence stars, in particular those

that are not in clusters or groups, are difficult to determine. Collisional models predict that the steady erosion of planetesimals will naturally lead to a decrease in the dust production rate. This slow decay will be punctuated by short-term episodes of increased activity triggered by large collisional events that can make the disk look an order of magnitude brighter. These models agree broadly with the observations derived from the *Spitzer* surveys. It is found that the frequency and fractional luminosities ($f = L_{dust}/L_*$) of debris disks around FGK stars with ages in the range $0.01 - 1$ Gyr decline in a timescales of $100 - 400$ Myr, but there is no clear evidence of a decline in the $1 - 10$ Gyr age range. This indicates that different physical processes might dominate the evolution of the dust around the younger and the older systems. A possible scenario is that, at young ages, stochastic dust production due to individual collisions is more prominent, while at older ages, the steady grinding down of planetesimals dominates.
The *Spitzer* surveys also showed that the evolution of dust around both A-type and FGK stars proceeds differently in the inner and outer regions, with the warmer dust (dominating the emission at 24 μm) declining faster than the colder one (seen at 70 μm). This indicates that the clearing of the disk in the inner regions is more efficient, as would be expected from the shorter dynamical timescales.
The duration of the dust production events (expect to be short if stochastic collisions dominate, and long otherwise) is critical to estimate what percentage of stars shows evidence of dust production throughout their lives. This is an important question to address because terrestrial planet formation is expected to result in the production of large quantities of dust in these regions (observable at 24 μm), so the fraction of stars showing excess emission at these wavelengths can shed light on the frequency of formed planets. If the dust-producing events are very long-lived, the stars that show dust excesses in one age bin will also show dust excesses at later times, and this may result in that $< 20\%$ of the FGK stars in these surveys show evidence of planetesimals formation near the terrestrial planet region. On the other hand, if the dust-producing events are shorter than the age bins, the stars showing excesses in one age bin are not the same as the stars showing excesses in another age bin, and this might result in that $> 60\%$ of these stars show evidence of planetesimals formation (assuming that each star only has one epoch of high dust production).

3.6 Planetesimals and planets

Beyond dust that, as we have seen above, is quite constrained from a physical and observational points of view, other objects populate a dusty planetary system. The bigger amongst them are planetesimals. Since planetesimals are not detectable because of their cool temperatures, nothing can be tell from data (neither photometric or imaging data) about them. Therefore, many of the basic parameters of the debris disk remain obscure. For instance, while the cross-section area of the disk and thus the observed luminosity are dominated by small particles at dust sizes, the bulk of a debris disk's mass is hidden in invisible parent bodies and cannot be directly constrained from analysis of dust emission. Equally, it remains unknown where exactly the planetesimals are lo-

cated, although one expects that they orbit the star roughly where most of the dust is seen. Many properties of the planetesimals, such as their dynamical excitation, size distribution, mechanical strength, etc. remain completely unclear. There is no direct way to infer the properties of invisible planetesimals populations from the observed dust emission. Dust and planetesimals can only be linked through models. This is done in two steps. Firstly, collisional models can be used to predict, for a given planetesimals family (mass, location, age, etc.), the distribution of dust. After that, thermal emission models have to be used to compute the resulting dust emission. Comparison of that emission to the one actually observed would then reveal probable properties of the dust producing planetesimals families.
The best constraints of planetesimals and their collisional evolution can be found from a combined analysis of the SED and resolved images.
Even if, at the moment, planetesimals remain quite a mystery under many points of view, they are extremely interesting for what regards their interactions with planets. More in general, debris disks gravitationally interact with possible planets at every moment in their life, and various footprints of those interactions can be evident in direct observations of debris dust. Planets may stir planetesimal disks, launching the collisional cascade. Beside the stirring, a variety of more direct fingerprints of planets can exist in the disks. Inner gaps tens of AU in radius commonly observed in resolved debris disk images and inferred from the debris disks statistics are likely the result of clearance by planets. We will treat these arguments very deeply in the following chapters focusing on those planetary systems that, like our Solar System, are known to contain, apart the central star and eventually one or more planets, an outer and inner planetesimal belt, divided by a wide gap of several tens of AU. A handful of such systems in this sense have been found so far, but only first steps have been taken to elucidate their detailed structure.
An example is the system HR8799 (see paragraph 5.3), a nearby A-type star with four confirmed planets. Apart from these latter, HR8799 has long been known to harbor cold circumstellar dust responsible for excess emission in the far-IR. The dust disk was resolved with Spitzer/MIPS at 24 and 70 μm. Additionally, Spitzer/IRS measurements provided evidence of warm dust emission in the mid-IR. Both cold and warm dust emissions are indicative of two dust-producing planetesimal belts. HR8799 is, then, a very complex planetary system that has an asteroid-like dust-producing inner belt at ~ 10 AU, four planets of a few Jupiter masses and an outer Kuiper-like planetesimal belt at 100 AU, associated with a tenuous dust disk that extends to several hundreds of AU from the star. Although many parameters of this system are very different from those of the Solar one, as for example the young age of HR8799, the arrangements of these components appear similar.
Another example is HD95086 system (see paragraph 5.3) which has an inner belt at ~ 9 AU and an outer one at ~ 63 AU. Recently, one planet of $\sim 5\ M_J$ has been detected by direct imaging near to the external belt and it's orbit is under astrometric analysis. The new data look like to point toward a nearly circular orbit and, as we will see later, even if the planet is very likely to be the responsible for the inner sculptured edge of the external belt, it is however not sufficient to dig the entire gap. We then would expect one or more planet to orbit interior to the detected one.

Many other systems have been discovered to be similar to our own, but we

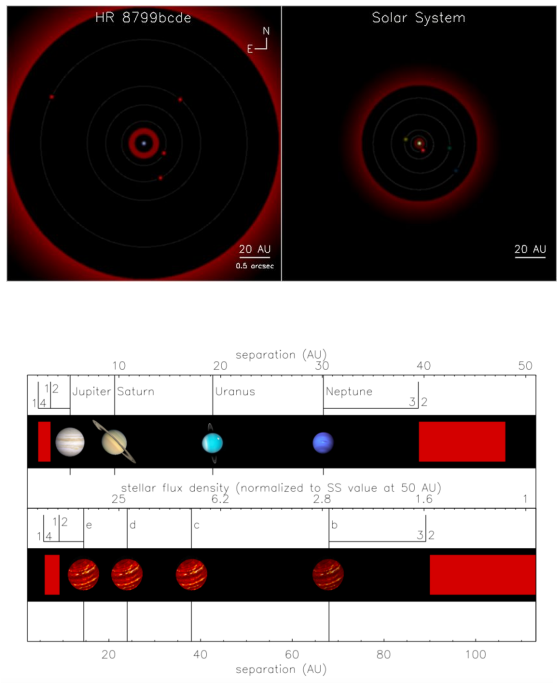

Figure 3.3: Ideal images of HR8799 compared with the solar system as seen from face-on (up) and edge-on (down). Credits: NRC-HIA and [13]

do not know yet which combination of planets and dusty planetesimal belts is common, how these components are typically arranged and which circumstances are decisive to set one or another type of architecture.
We conclude this section presenting some of the mechanisms that set in due to gravitational forces exerted by planets on debris disk. If the dust particles are constantly being released by a planetesimals belt, P-R drag and radiation pressure would create a dust disk of wide radial extent and uniform surface density. However, if one or more planets are present in the system, on their journey toward the central star, the dust grains will be affected by gravitational perturbations that will modify their spatial distribution. Indeed, as the particle drifts inward, diminishing its semi-major axis and eccentricity, it might get trapped in a mean motion resonance with one of the planets. Mean motion resonances are located where the orbital period of the dust particle, t_d, is related to the one of the planet, t_p, by

$$t_d = \frac{p+q}{p} t_p, \tag{3.17}$$

where p and q are integers, $p > 0$ and $p+q \geq 1$. While the planet orbital period is

$$t_p = 2\pi \Big(\frac{a_p^3}{GM_*} \Big)^{1/2}, \tag{3.18}$$

the effect of radiation pressure results in a dust particle orbital period of

$$t_d = 2\pi\Big(\frac{a_d^3}{GM_*(1-\beta)}\Big)^{1/2}, \tag{3.19}$$

because the particles feel a less massive star by a factor $1-\beta$. Therefore mean motion resonances take place when

$$a_d = a_p(1-\beta)^{1/3}\Big(\frac{p+q}{p}\Big)^{2/3}. \tag{3.20}$$

The particle is trapped when, in the reference frame co-rotating with the planet, the closest approach between the particle and the planet is always at the same point(s) along the particle orbit. At these location(s) the particle receives repetitive kicks from the perturbing planet that are always in the same direction and can balance the energy loss due to P-R drag, halting the particle migration. While trapped, the particle semi-major axis stays constant, while its eccentricity slowly increases. The particle escapes from the resonance when its eccentricity becomes sufficiently high. After escaping, it keeps spiraling inward under P-R and stellar wind drag. Even though the width of resonant regions are finite, these narrow zones of parameters space can become densely populated with dust because they are constantly being fed by the inward migration of dust particles. This effect is more pronounced for larger grains because they have a greater trapping probability due to their slower migration velocity, which is proportional to $1/s$. Generally, more massive planets exert a stronger perturbing force and allows the trapping of dust particles at resonances located further away from its position.

Another effect that could feel a dust particle spiraling inward and encountering a giant planet is a sudden perturbation to its orbit due to the presence of the latter. The orbit, then, becomes chaotic and the particle is subjected to gravitational ejection. This chaotic region extends from $a_p - \Delta a \leq a \leq a_p + \Delta a$, where a_p is the planet semi-major axis and Δa is the semi-amplitude of the chaotic zone, proportional to the semi-major axis of the planet and to a power law of the ratio between the mass of the planet and the mass of the star, $\mu = M_p/M_*$ (see chapter 6).

The gravitational force on dust particles exerted by planetary companions is described by a sum of many terms that compose the so called perturbing function. The average of these contributions on the long term gives rise to secular perturbation effects. Unlike the resonant perturbations described above, secular perturbations are non-periodic in nature and act on longer timescale (> 0.1 Myr). They can be thought of as the perturbations that would arise if the mass of the perturbing planet were to be spread out along its orbit, weighting the mass density to reflect how much time the planet spends in each region. Thus, a planet on an eccentric orbit can force an eccentricity on the debris particles. If the planet and the particles are not coplanar, the secular perturbation will tend to align their orbits while it will not affect the semi-major axis of the particles. If there is only one perturbing planet, the strength of the perturbation is dependent on its mass, but the smaller the mass the longer the secular timescale. If there is more than one perturbing planet, particles with precession rates that coincide with the eigenfrequencies of the planetary system (resulting from secular perturbations between the planets) will be strongly affected by secular perturbations, resulting in the ejection of these particles from the secular

resonant region.
Combining the effects of secular perturbations and mean motion resonances inferred by planets on dust and planetesimals, we get particular features in the disk's structure. For example, resonant rings are created when the dust particles are on nearly circular orbits and because they spend a significant part of their lifetime trapped at certain semi-major axis, corresponding to the most favorable mean motion resonances. Moreover, the presence of asymmetric clumps happens when the particles are on eccentric orbits in mean motion resonance and avoids being close to the perturbing planet. Secular perturbations can also produce warps, spirals and brightness asymmetries.
Most of the structural features described above depend on the mass and orbit of the planet and the structure is sensitive even to small planets and planets located far from the star. This opens the possibility of using the study of dusty disk structure as a sort of detection technique of planets of a wide range of masses and semi-major axis.

Chapter 4

Detecting techniques

Detecting planets is a very challenging aim because they are relative small and cool objects far away from us. For these reasons for many years they have been undetectable and quite unknown. However, with increasing technologies and extremely efficient instruments, we have reached in recent times a wider catalog of planets (up to some hundred of detected planets) of many different sizes and types, and we expect great improvements in the exoplanet research field thanks to dedicated space missions and surveys that will start in the next future, such as PLATO 2.0. There exist few methods to detect a planet but each of these techniques is suitable in reveal objects at different distances from the star and with different masses. To date nearly 2000 planets have been found using the methods described beneath. We show in figure 4.1, updated at 2016, the entire database of known exoplanets plotting their masses against semi-major axis and indicating the techniques with which they were detected. In this chapter we thus describe detection techniques used to find exoplanets, with particular attention to radial velocity and direct imaging.

4.1 Radial Velocities

This method, as its name suggests, uses a change in the radial velocity of the star in order to guess the presence of a planet. Indeed, when two massive objects mutually attract each other due to gravitational interactions, they move on elliptic (in the more general case) orbits around their center of mass. When these two objects are a star and a planet, the mass of the first is much bigger than the latter so that the center of mass will be almost coincident with the center of the star. This little displacement, however, is sufficient to produce periodic variations in the radial velocity of the star detectable from the Doppler shift of the stellar spectrum, which can be measured with a precision of the order of a m/s.
In order to understand how we can deduce the mass of a planet using radial velocity method let us assume the simple case of circular orbits around the center of mass. Consider a planet of mass M_p around a star of mass M_* on circular orbit of semi-major axis a_p. Since $M_p << M_*$, we can approximate the

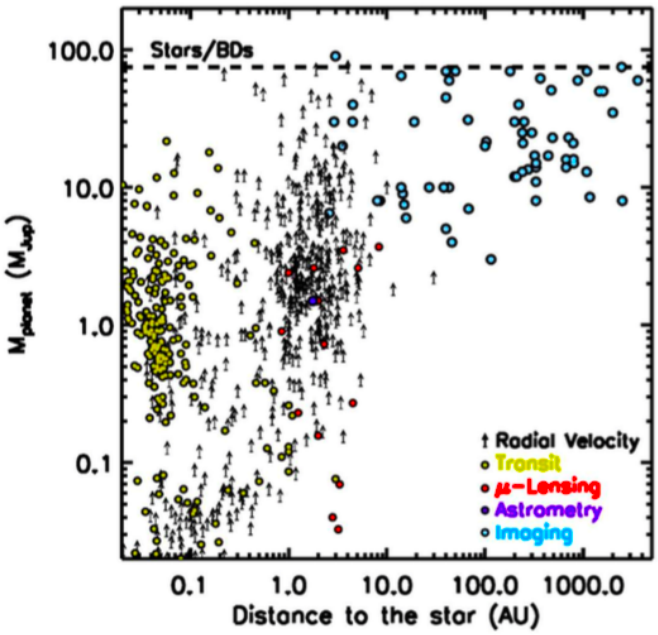

Figure 4.1: All exoplanets known to date, plotted as a function of their masses, semi-major axis and detection techniques used. Credits: G. Chauvin

orbital velocity of the planet with the Keplerian velocity

$$v_K = \sqrt{\frac{GM_*}{a_p}}. \tag{4.1}$$

From the conservation of linear momentum, $M_* v_* = M_p v_K$, we can obtain an expression for v_*. We have, however, to take into account also the inclination angle i under which we are observing the system. Then the radial velocity of the star varies sinusoidally with a semi-amplitude

$$K = v_* \sin i = \left(\frac{M_p}{M_*}\right)\sqrt{\frac{GM_*}{a_p}} \sin i, \tag{4.2}$$

and K is a directly observable quantity. If the stellar mass can be estimated independently but the inclination is unknown, as in common situation, then we have two equations and three unknowns and we can only establish a lower limit to the planet mass imposing $i = \pi/2$ in $M_p \sin i$ that corresponds to observe the system as face on. However, since the average value of i for randomly inclined orbits is $\pi/4$ statistical correction between the minimum and true mass is not large.
In order to have an idea of the magnitude of the signals that we can get from radial velocity, we can look at the Solar System: for Jupiter $v_* = 12.5 m/s$ while for the Earth $v_* = 0.09 m/s$. For planets of a given mass there is a selection bias in favor of finding planets with small a_p.

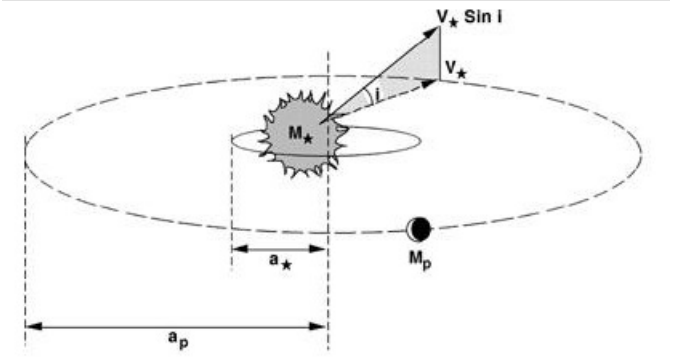

Figure 4.2: Representation of a system with a star and a planet orbiting their center of mass.

For real applications it is necessary to consider the radial velocity signature produced by planets on eccentric orbits. Thus, let us call the eccentricity of the orbit of the planet e_p, the semi-major axis a_p, and the period P. The orbital radius thus varies between the apocenter $a_p(1+e_p)$ and the pericenter $a_p(1-e_p)$. Let us, then, suppose that the passage of the planet at the pericenter occurs at t_{peri}, then we can define implicitly the eccentric anomaly E by Kepler's equation

$$2\pi \frac{t - t_{peri}}{P} = E - e_p \sin E \tag{4.3}$$

This equation can be solved only numerically and once E is known we can express the true anomaly f, i.e. the angle between the vector joining the bodies and the pericenter direction, through

$$\tan \frac{f}{2} = \sqrt{\frac{1+e_p}{1-e_p}} \tan \frac{E}{2}. \tag{4.4}$$

Finally we can express the radial velocity of the star as

$$v_*(t) = K[\cos(f + \bar{\omega}) + e_p \cos \bar{\omega}], \tag{4.5}$$

where $\bar{\omega}$ is called the longitude of pericenter and is the angle in the orbital plane between pericenter and the line of sight to the system. The eccentric generalization of equation (4.2) in the limit $M_p << M_*$ is

$$K = \frac{1}{\sqrt{1-e_p^2}} \left(\frac{M_p}{M_*}\right) \sqrt{\frac{GM_*}{a_p}} \sin i. \tag{4.6}$$

For a planet of given mass and semi-major axis, the amplitude of the radial velocity signature thus increases with increasing e_p, due to the rapid motion of

the planet (and star) close to pericenter passage. Compared to a circular orbit of equal period, a planet on an eccentric orbit produces a stellar radial velocity signal of greater amplitude when near to the pericenter, but there are also long periods near apocenter in which the signal is fainter compared to the circular one. For this reason planets on circular or eccentric orbits are equally likely to be found and there is no proper bias toward eccentric planets.
This method is certainly one of the most successful in finding exoplanets of masses down to $\sim M_\oplus$, but it let us discover only objects quite near to their star, since wider orbits needs extremely long observations. Moreover, small Mercury-like planets cause perturbations to the orbit of the star that are too small to be reveled. Thus, radial velocities studies work well to characterize part of the inner system but fails in detecting further out planets and we have to elaborate other observational strategies.
We will study in chapter 8 nearly ten systems in which one or more planets have been found orbiting their stars using radial velocity method.

4.2 Direct Imaging

The first idea that one may have to detect an extrasolar planet is to actually image it with the telescope. However get an image in which the light from the planet and the the star are spatially separated is not at all an easy task because of the extreme contrast between the two bodies. A planet of radius R_p, orbital radius a_p and albedo A intercepts and reflects a fraction of the incident stellar light that is given by

$$f = \Big(\frac{\pi R_p^2}{4\pi a_p^2}\Big)A = 1.4x10^{-10}\Big(\frac{A}{0.3}\Big)\Big(\frac{R_p}{R_\oplus}\Big)^2\Big(\frac{a_p}{1AU}\Big)^{-2}. \tag{4.7}$$

Thus for a terrestrial planet similar to our own this contrast is very unfavorable. Additionally, Earth-like planet are $24-25$ magnitudes fainter than their host star. Thus really deep exposure are needed in order to directly imaging an exoplanet.
We would have better results in imaging a planetary system in its thermal emission: if we suppose the planet to emit like a blackbody at temperature T, from the Planck function we get

$$B_\nu(T) = \frac{2h\nu^3}{c^2}\frac{1}{e^{\frac{h\nu}{k_BT}}-1}, \tag{4.8}$$

where ν is frequency, c the speed of light, h the Planck's constant and k_B the Boltzmann's constant. From the Wien's law we know that this function has a maximum at $h\nu_{max} = 2.8k_BT$ which, for typical temperature of terrestrial planets, lies in the mid-infrared ($\nu_{max} \sim 20\mu m$ for the Earth with $T = 290K$). If we use the hypothesis of blackbody also for the star, the flux ratio f at frequency ν is given by

$$f = \Big(\frac{R_p}{R_*}\Big)^2\frac{e^{\frac{h\nu}{k_BT_*}}-1}{e^{\frac{h\nu}{k_BT}}-1}, \tag{4.9}$$

where R_* and T_* are the radius and temperature of the star, respectively. Using values for Earth and Sun analogs we now get $f = 10^{-6}$, that is four orders bigger

than the flux ratio for reflected light. However, the infrared observations present other kinds of challenging problems. Indeed, the spatial resolution of a telescope is

$$\theta \sim 1.22\frac{\lambda}{D}, \tag{4.10}$$

where D is the diameter of the telescope and λ the wavelength at which it works. Then, we can see that obtain high spatial resolution at longer wavelengths requires telescopes with large diameters. For example, in the infrared in order to have acceptable spatial resolutions we would need instruments with D of tens of meters (moreover, they should be positioned above the atmosphere since it absorbs the great part of the radiation in this range of wavelengths). On the other hand, in the visible quite small telescope (of the order of some meters) are suitable.
Another important observation about direct imaging is that while it can quite easily reveals giant planets orbiting far from the star, it has a much harder work in detecting terrestrial planet in the so called habitable zone, i.e. the area in which the water can survive in liquid form, and other techniques (at the moment) are much more efficient. Nevertheless, this method is an extremely useful tool even if so challenging since it offers complementary information to other techniques (for example, for radial velocities it resolves the $\sin i$ ambiguity) and allows mass measurements of individual exoplanet. Moreover, direct imaging can characterize some elements such as atmospheres and signatures of life (presence of ozone, oxygen or methane) that are determinant to discriminate between habitable and inhabitable planets.
Some complementary techniques are under study in order to overcome the contrast problem, blocking or canceling the stellar contribution. One of these uses a device that blocks the starlight, directly with an occulting mask or modifying the shape or transmission of the pupil. Such instrument is called coronagraph and can reach starlight suppression factor of the order of 10^{10}.
Direct imaging is an extraordinary source of informations since it could not only revealed the presence of planets, but it can also spatially resolve systems in which debris disks are present (see paragraph 3.1), providing a more complete and deeper comprehension of the whole architecture.

4.2.1 SPHERE

The instrument with which the great part of the systems that we are going to study (see chapter 5) have been observed is SPHERE, a second generation instrument at VLT. It stands for Spectro Polarimetric High-contrast Exoplanet and provides high contrast direct imaging data by combining extreme adaptive optics (XAO), coronagraphy, accurate calibration of path instrumental aberrations and post-observational data calibration through various differential methods. The instrument is integrated on a large optical table that contains all the common-path optics including the XAO module and infrastructure such as the calibration source module. Three scientific instruments are attached to this main bench: a differential near-infrared imaging camera and spectrograph (IRDIS, InfraRed Dual Imaging Spectrograph), a near-infrared low spectral resolution Integral Field Spectrograph (IFS) and a visible imaging differential polarimeter (ZIMPOL, Zurich Imaging Polarimeter).
Thanks to its high performances, SPHERE is capable of detect giant planets of

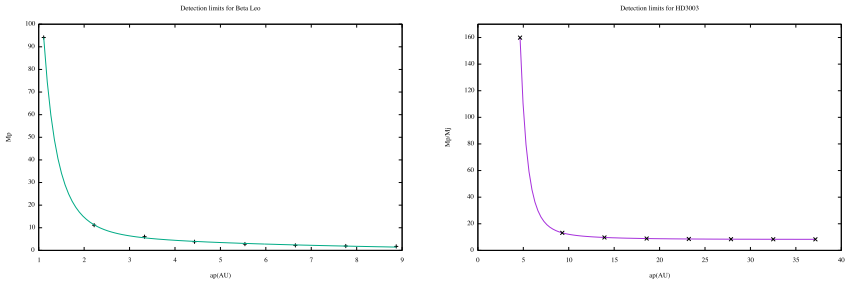

(a) (b)

Figure 4.3: Fig. (a):Detection limits for Beta Leo Fig.(b): Detection limits for HD3003

some Jupiter masses orbiting their stars at some AU of distance. Characteristic curves of this instrument are called detection limits that plot the mass of the planet, M_p, as a function of its distance, a_p, from the star. In order to get such curves we have to convert available data of apparent magnitude in planet mass. This process consists of two steps: in the first one we pass from apparent magnitude m to absolute magnitude M using the distance d of the star from the Sun; then we have to transform M into M_p and this is done using the age of the star and evolutionary models. Since both the distance, the age of the star and evolutionary models are affected by uncertainties (particularly the latter two) what we should get is not a line dividing neatly the detectable from undetectable zone, but most likely an entire region in proximity of the curve in which the planet could or could not be revealed. We show, as examples, detection limits for the systems Beta Leo and HD3003 in figure 4.3. All the point plenty above the curve are detectable whereas all the point sharply beneath it are undetectable, and in proximity of it we have an uncertain region. As we will see later, the same planet could be always visible or invisible using SPHERE but, in many cases, if it moves on eccentric orbit thus varying its orbital radius, it can enter into and exit from different detection zones. For this reason, to exclude the presence of a planet in a direct imagined system more observations in a wide range of time are needed. From these two graphics we can also see clearly the difficulty in detecting planets with small masses and/or quite near to the star. Obviously, detection limits vary from system to system: for example one planet of 10 M_J on circular orbit at 4 AU around Beta Leo is detectable whereas it is not in HD3003 system. However, in neither of them planets under one jovian mass could be revealed.
Since this work is based on the study of systems direct imagined with SPHERE, it will focus on the study of giant planets orbiting quite far from their star. More characteristic of such systems (age, distance from us, presence of debris disk, etc.) will be discussed in the following chapter. We present in Appendix A all detection limits available for the systems take into account.

4.3 Other techniques

The systems that we are going to study later in this work have been analyzed using radial velocities or direct imaging. However, there exists other methods to detect exoplanets.
One of these is astrometry: it measures the stellar reflex motion in the plane of the sky due to the presence of planets. From the definition of the center of mass we can express the semi-major axis of the star as $a_* = (M_p/M_*)a_p$. For a star at distance d from the Earth the angular displacement of the stellar photocenter during the course of an orbit has a characteristic scale, given by

$$\theta = \Big(\frac{M_p}{M_*}\Big)\frac{a_p}{d}. \tag{4.11}$$

Thus, astrometry favors planets with large semi-major axis and it measures two independent components of the stellar motion yielding to more constraints on the orbit. Expressing θ as a function of typical values we get

$$\theta = 5x10^{-4}\Big(\frac{M_p}{M_*}\Big)\Big(\frac{M_*}{M_\odot}\Big)^{-1}\Big(\frac{a_p}{5AU}\Big)\Big(\frac{d}{10pc}\Big)^{-1} arcsec. \tag{4.12}$$

Even if this is a very small displacement, high precision instruments are capable of detecting such small variation so that astrometry can be used to detect a wide range of hypothetical planets.
However, up to date, astrometry has not been widely used in finding exoplanets since, as we have seen, it needs such resolutions that are quite unattainable from the ground due to atmospheric perturbations. Indeed, astrometry is mostly used to perform further follow-up on objects that have already been detected with other techniques. Nevertheless, when the space mission GAIA (2016) will take off, astrometry will occupy a primary role in detecting exoplanets since it is based on this observing method.
Another method that we briefly illustrate is photometric transits: a planet that, at a certain time during its orbit, goes ahead its star causes a dimming in the stellar flux. We show this situation in figure 4.4. The amplitude of the transit signal is independent of the distance between the planet and the star and provides a measure of the relative size between the two bodies. If a planet of radius R_p occults a star of radius R_* the fractional decrement f in the stellar flux during the transit is

$$f = \Big(\frac{R_p}{R_*}\Big)^2. \tag{4.13}$$

Register a transit becomes more complicated if the system is seen from an angle far from the edge-on configuration (for example a face-on system has no transits at all).
For a giant Jupiter-like planet orbiting a Sun-like star we get $f = 0.01$ while for a Earth-like planet $f = 8.4x10^{-5}$. The photometric precision of ground-based observations is limited by atmospheric fluctuations and it is possible to detect only giant planets. In order to detect terrestrial planets observations from space are necessary. The *Kepler* space mission has indeed showed the powerfulness of transit technique detecting hundreds of terrestrial planets and many of the future space mission (PLATO 2.0, TESS, etc.) will use this method to find the twin of the Earth. However, this method furnishes only the radius of the

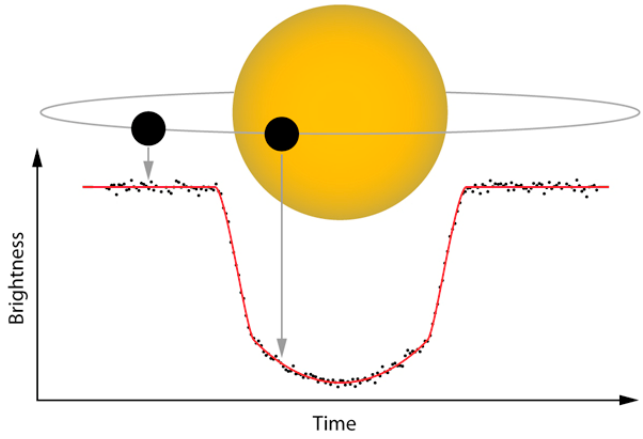

Figure 4.4: Photometric transit of a planet seen edge-on ($i = 0$)

hypothetical planet and in order to know also its mass further follow up are needed (for example radial velocity techniques). Transits are particularly useful in searching very small objects, down to 0.01 $M_{\oplus}$ for instruments above the atmosphere, and thus unique in this sense.
The left two methods are gravitational microlensing and timing.
Timing techniques detect planets studying the variations of durations of periodic phenomena on stars inducing by the presence of substellar companions (for example, variation in pulsar frequency) or on planets in the same system due to their mutual gravitational interaction (as for example, the different duration of their orbital periods or transits in front of the star). Timing itself is not sufficient to fully characterize an object and is mostly associated with other detection methods.
Gravitational microlensing, instead, uses the relativistic effect of the deviation of light due to a massive object. Indeed, if we have a star (the source in the background) that is aligned with a further one (the lens in the foreground), photons from the source travel toward the lens plane and, when they reach it, they will be deflected of a certain angle α. This causes a distortion of the image of the background star that will be seen, if perfectly aligned, as a ring (the Einstein ring) around the lens. If a planet orbits the source, thus more perturbations to the light curve are expected. This method is applied on very distant systems (near to the galactic centre) that can not be observed with any of the previous methods that, instead, work well only on quite near stars. The usefulness of gravitational microlensing is thus a statistic one since it can tell us how many stars own one or more exoplanets but we are not able to fully characterize them.

Chapter 5

Choice of the targets

The first practical step of this work is the choice of the targets to analyze. For this purpose, we use a published catalog (Chen et al. 2014, [4]) in which are presented some hundreds of systems with debris disk detected by the *Spitzer Space Telescope*. Such disks have been modeled analyzing the excesses in the infrared of the spectral energy distribution of each system and assuming zero, one and two debris components. We select amongst them only the ones best described by double dust component. Moreover, since our main interest is to analyze planetary systems detected using direct imaging, we cross this restricted selection of objects of the Chen's catalog with the list of targets of SPHERE. We match also this catalog with systems with known exoplanet revealed by means of radial velocity but we present this study in chapter 8.
In this chapter we are going to illustrate how the Chen's catalog has been created and how the SPHERE targets have been chosen. We then provide the final list of systems that we will consider later for our dynamical analysis.

5.1 Chen catalogue

Since the presence of a debris disk seems to be a quite common and really much interesting feature around a wide range of kind of stars (see chapter 3), many works have been elaborated on this subject. Christine Chen and her collaborators released in 2014 a catalog (from now on C14) of candidates systems to own a debris disk, using principally data from the *Spitzer Space Telescope* cryogenic mission. The most interesting result for our purposes provided by this list is the temperature of the grains, T_{gr}, from which their position is inferable from blackbody assumptions.
Let us illustrate how the C14 has been obtained. They have calibrated the spectra of 571 stars looking for excess in the infrared from 5.5 μm to 35 μm (from the *Spitzer* survey) and when available (for 473 systems) they used also the MIPS 24 μm and/or 70 μm photometry to calibrate and better constraint the targets SEDs. These systems cover a wide range of spectral type (from B9 to K5, corresponding to stellar masses from 0.5 $M_{\odot}$ to 5.5 $M_{\odot}$) and ages (from 10 Myr to 1 Gyr) with the majority of targets within 200 pc from the Sun.
Since debris disks dissipate with time and evolve dynamically, it is of great importance to estimate the age of the system. Thus, they proceeded in the

following way: if, in literature, the star was identify as a member of a stellar kinematic group or cluster, they deduced its age placing all the stars of the group/cluster in the same Hertzsprung-Russel diagram (H-R) and tracing the isochrone (this is the most precise method); if the star does not belong to a group, they used the gyrochronology age present in literature (as solar-mass stars get older, they lose angular momentum via stellar winds that break their rotation; therefore their activity and rotation period decline as they age); for stars without measured rotation periods but with measured Ca II H and K activity indices ($\log R'_{HK}$), $\log R'_{HK}$ can be used to calculate stellar rotation period and thus the age of the star; finally, for the remained stars they used H-R diagram ages, that are the least robust with typical errors of a factor of two. The samples they analyzed is composed of one third of stars with ages < 100 Myr, another third with ages in the range [100 Myr, 1 Gyr] and the final third with ages from 1 Gyr to 10 Gyr.
The other fundamental property of a star that is needed to better describe the evolution and characteristics of its debris disk is its mass. They estimated star masses in two ways: for stars in group/cluster whose ages were deduced using H-R diagram fitting, they used masses obtained from isochrones; otherwise they used the mass-luminosity relationship.
Finally, they constructed stellar photosphere models using minimum χ^2 fitting to model stellar atmospheres and moved to analyze the excesses in the infrared. They measured the fluxes for all 571 sources in two bands, one at $8.5-13$ μm that was developed to search for weak 10 μm silicate emission and another at $30-34$ μm to search for long wavelengths excess of cold grains. Then, they modeled the excesses of SEDs using zero, one and two blackbodies (see paragraph 3.4) because debris disks spectra typically do not posses strong spectral features and temperatures. In the zero-blackbody model, they allowed for the possibility that the targets did not posses any excess flux at any wavelength. For each model (zero, one and two debris components) and given data, they defined a grid of parameters space to be explored and calculated the probability of each set of parameters. Then, they selected the best model using Bayesian parameter estimation. They found that two dust components are common, with $\sim 66\%$ of debris disk systems containing such structure and thus two planetesimals belts.

For what regards temperatures and positions of grains they obtained quite different results for systems with one or two components. Indeed, they found that the single-belt systems are well fitted using T_{gr} in the wide range $100-500$ K. However the majority of them are cooler than our asteroid belt ($T_{gr} < 200K$). Instead, in the two-belts systems the warm component assumes T_{gr} from 100 K to 500 K and the cold one from 50 to 150 K, analogous to the asteroid belt with $T_{gr} \sim 230K$ and to the Kuiper belt at $T_{gr} \sim 40K$. They noted also that the grain temperature distribution for the one and two belts are distinguishable since the warm component of the latter has much higher temperatures than the first one and similarly for the cold particles which are much cooler in double than in single belt systems. In addition, the grains' temperature distribution for the one-belt system is substantially different from that of the average of the warm and cold dust components of the double-belts system. For these reasons, is quite simple to distinguish between targets with one or two dust components. They tried also to confront one and two belts systems with respect to their stellar properties, t_* and M_*. The expected results were that two-belts are located around younger and/or more massive stars because such systems own,

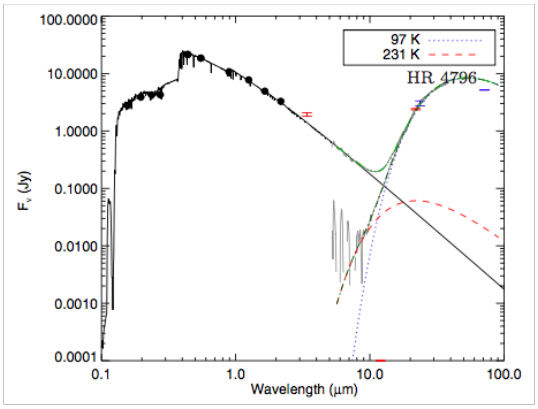

(a)

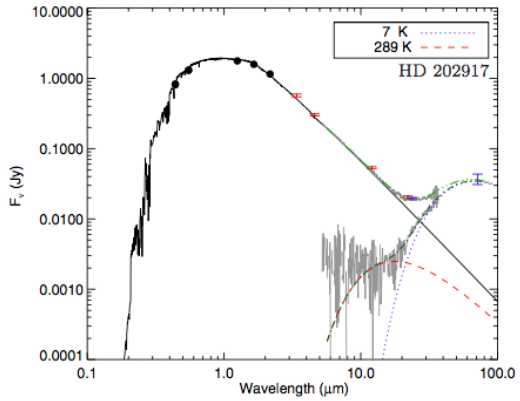

(b)

Figure 5.1: Two SEDs with excesses in the infrared better fitted by double blackbody temperatures. The red dashed curves represent the warm component while the blue dotted ones the cold component. Fig.(a): Spectral energy distribution for HR4796 ($T_{d,1} = 231K$ and $T_{d,2} = 97K$) Fig.(b): Spectral energy distribution for HD202917 ($T_{d,1} = 289K$ and $T_{d,2} = 7K$). Credits:[4].

on average, more dust than the single belt ones. Indeed, they found that the mean age and mass for the latter are $\sim$ 300 Myr and 1.4 $M_{\odot}$ whereas for two-belts systems $\sim$ 70 Myr and 1.6 $M_{\odot}$, thus confirming the expectations. The cumulative distribution fraction for the entire sample of one and two belts systems in C10 catalog are shown in figure 5.2 and are plotted as functions of the age and of the mass of the stars.
We will be interested in the following by systems with double belts that, as we have just seen, are quite common around main sequence stars.

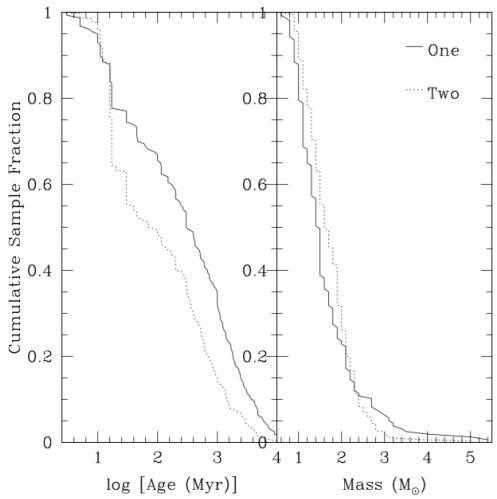

Figure 5.2: Cumulative distribution fractions for single (solid) and double (dotted) belt systems as a function of age (left) and mass (right) of the stars. Credits:[4].

5.2 SPHERE targets

SPHERE, as we have already said above, is an high contrast direct imaging instrument. This kind of technique is particularly interesting because it is able to provide informations on the atmosphere of the planet and thus on its habitability, on the dynamical stability and evolution of the system and on the connection between the exoplanet and the disk that surrounds the star.
The survey from which we are going to select our list of systems has 260 guaranteed nights at VLT, spent from February 2015 over to the next 5 years. The time of the survey has been divided in fuor science programs:

- SHINE, a survey in the near infrared for exoplanets around $400-600$ stars (200 nights);
- DISK, a survey that aims to individuate and characterize protoplanetary and debris disks (20 nights);
- REFPLANETS, a survey that looks for exoplanets in the visible and /or reflected light (18 nights);
- OSCIENCE, a complementary survey of target of interest such as evolved stars, clusters, etc. (12 nights).

The great part of the attention is thus focused on exoplanets, particularly on giant young ones, that are capable yet to emit in the infrared.
The preselection of the targets to point was based on few important parameters. Obviously, all the targets are near the Sun (particularly, targets of our list stay beneath 150 pc) in order to spatially resolved the star from its components (planets, debris disks). Moreover, all systems are quite young ($t < 1$ Gyr) because at such ages giant gaseous planets have just formed and are still cooling

down and thus detectable through their thermal emission. Other important parameters were the brightness of the target, the declination of the system and the binarity. The statistical sample obtained following these parameters is formed of 400 objects plus other 400 back-up systems, at which they have added other systems of particular interest (stars with debris disk or known substellar companion, etc.). We show in figure 5.3 the distribution of the entire sample for what regards mass, age and magnitude in V-band of the star and distance from the Sun.

Up to May 2016, 70.5 nights of the survey were completed ($\sim$ 35%) and 240

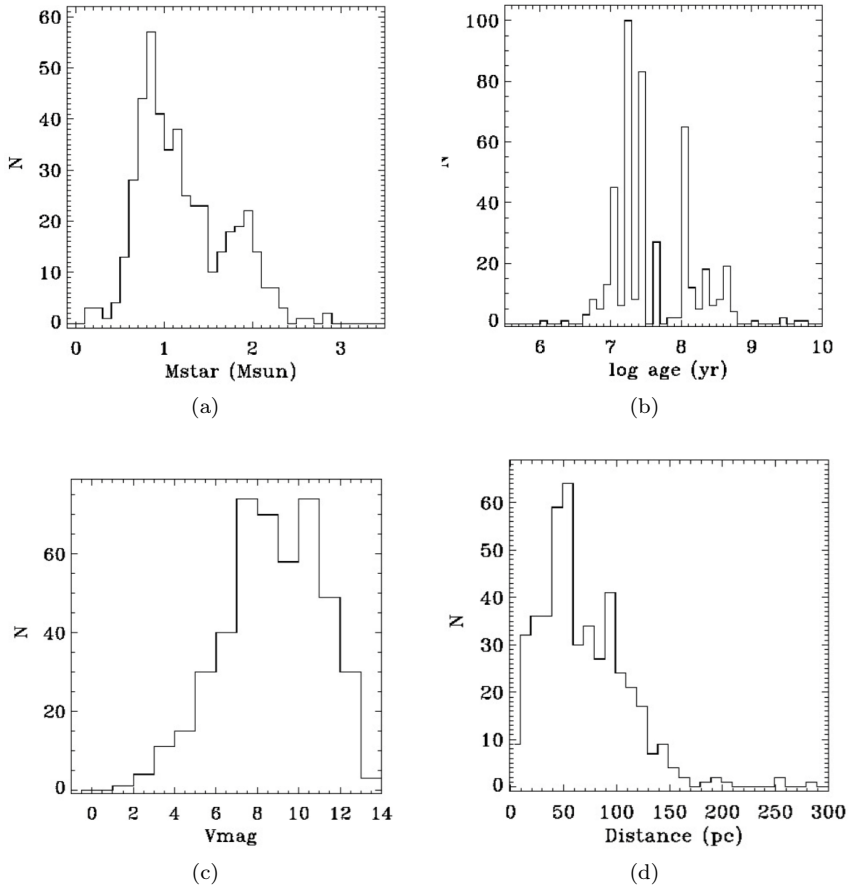

Figure 5.3: Number of stars as a function of stellar mass (up left), age (up right), magnitude in V-band (down left) and distance from the Sun (down right) for the sample of SPHERE. Credits: M. Langlois

targets were observed.

As mentioned before, the SPHERE instrument is capable to reveal massive planets of the order of some jovian mass at, at least, intermediate separations of some AU. For these reasons our work is concentrated on the possible presence of giant planets in systems with double belts as responsible for the gap between the two, not caring about eventual terrestrial planets that from protoplanetary

evolutionary models, however, are expected to be in the inner part of the system in analogy to the Solar one.
Before we show the complete list of systems to analyze, we want to underline that the choice of targets have been done during the survey and so we include in our analysis also some objects for which, during later observations, data have not been validated. For such systems no detection limits are available but we perform anyway their dynamical analysis (see chapter 6 and 7). Moreover, the survey has already a long lifetime and many other systems are going to be observed, therefore, providing a much larger sample of double debris belts systems on which apply the studies that we are going to illustrate.

5.3 Planetary systems examined

The first step in order to establish the final ensemble of systems on which perform our dynamical studies is to select from C14 (available on the Vizier server) all elements in which two dust temperatures were present, $T_{gr,1}$ and $T_{gr,2}$, that implies the presence of two planetesimals belts. Then we cross this first selection with the targets of SPHERE observed until March 2016 and finally get forty suitable objects. Many additional targets are in the SPHERE GTO sample, then allowing a more extended investigation in coming years. We show the selected systems in the following tables: in the first one we list the stellar parameters of the systems under analysis while in the the second we show the temperatures and distances from the central star of the two debris belts present in each system. In table 5.1 we can clearly see all the characteristics of the sample of objects mentioned above. Indeed, they are main-sequence young stars ($t < 500Myr$) in a wide range of spectral types, beneath 120 pc from the Sun.
We have already seen, in chapter 3, that the link between the temperature of dust and its position, deducible from blackbody model and a ring-like geometry, is affected by degeneracy if we let fall the first of the two assumptions. Indeed, if the grains do not behave like perfect blackbody a third component, the size of dust particles, must be take into account. Thus now the same SED could be produced by bigger grains further out or smaller particles closer to the star. Therefore, in order to break this degeneracy, we search in literature for that debris disks in our sample that have been previously spatially resolved using direct imaging. In table 5.2 we show for each system the temperature of the inner and the outer belt, $T_{gr,1}$ and $T_{gr,2}$, the positions of the outer edge of the inner belt and the inner edge of the external one, d_1 and d_2 respectively. In columns 3 and 5 the positions of the rings is taken from C14, as obtained from blackbody assumption; instead in columns 7 and 8 positions come from direct imaging data. We find 13 resolved objects that we will describe in details beneath. Obviously, for the excess SED analysis, using d_1 and d_2 as outer and inner edge is only an approximation since they should represent the position at which most of the dust is concentrated, thus the mid-radius of the planetesimal belt. From direct imaging data instead many peculiar features are clearly visible and sculptured edges are much better constrained. We want to underline that most of these systems are resolved only in their further component (actually, just two objects, HD95086 and HD71155, have both the inner and the outer belt imaged) since the inner belt is very near to the star so that we are not able to separate its contribution from the flux of the star itself.

Let us now briefly described the resolved systems.

HD181327 (see [22]). It is a main sequence star with a strong thermal emission ($L_{IR}/L_* = 0.25\%$, L_{IR} is the luminosity in the infrared of the dust). HD 181327 is a member of the β Pic moving group so that its age is well constrained. It has been a target of high-contrast (coronagraphic) imaging investigations at both near-IR and visible wavelengths. An optically thin bright light-scattering debris disk circumscribing HD181327 ($F_{disk}/F_* = 0.17\%$ at 1.1 μm) was first observed and then it was analyzed in the mid-infrared with IR spectroscopy. Together, those observations revealed the existence of a relatively narrow ring-like debris belt responsible for $\sim 70\%$ of the total disk and it is surrounded by a much larger and asymmetric halo. The ring is inclined at $102^\circ \pm 4^\circ$ with respect to the plane of the star and we see the entire system at an angle $i = 30.1^\circ \pm 1.2^\circ$ from face on. The much more recent direct imaging data of this debris disk improve the HD181327 science. A newly discovered radial variation in the apparent scattering phase function may imply the presence of a yet unimaged planetary-mass perturber. It also reveals previously unseen substructures and brightness asymmetries along the ring.
Morphologically, the HD181327 debris disk appears as an asymmetrically bright narrow elliptical ring at 88.5 AU cleared of scattering material in the interior and in the exterior surrounded by a larger, fainter diffuse region. The most interesting feature for our analysis is that the narrow ring presents a well sculptured inner edge at ~ 80 AU, at which we thus place d_2.

Eta Tel (see [24]). It is too a member of the β Pictoris moving group, with a well estimated age. Eta Tel was first identified as a star with a debris disk using IRAS measurements which indicate that excesses emissions were present at 12, 25 and 60 μm. The excess measurement at 12 μm is particularly rare as debris disks are typically characterized by dust at several tens of AU which is too cool to emit at 12 μm.
Eta Tel was imaged at 11.7 and 18.3 μm, with the T-ReCS instrument on Gemini South which indeed shows a resolved debris disk at 18.3 μm. The analysis of Eta Tel was done taking into account different models, the better one of which is a two free parameters model that assumes the disk emission as composed by a narrow ring of radius r and an unresolved component. Thus it emerges that Eta Tel owns a resolved component at 24 AU and an unresolved one at 3.9 AU (from SED analysis).

HD15115 (see [21]). HD15115 is a nearby star with an edge-on asymmetric debris disk spatially resolved in the visible and near infrared. The star is believed to be young for several reasons: it has shared kinematics with the 12 Myr old β Pictoris moving group, it is believed to be on the zero-age main sequence and it has a high fractional luminosity circumstellar disk ($f_d = 4.9x10^{-4}$), which is more commonly seen for younger stars. However other indicators, such as Ca II H and K lines and X-ray emission, may point to a much older age, perhaps $100-500$ Myr. In C10 the used age is of 12 Myr, but there is a great uncertainty about this feature.
HD15115 circumstellar disk is believed to be gas-poor and has 0.047 $M_\oplus$ in dust mass. Therefore, the disk is considered to be predominantly debris. At visible wavelengths, the disk is highly asymmetric, with the western lobe extending in

a needle-like feature.
It has been estimated the dust grain size ($\sim 3\mu m$) from the disk color and the surface brightness (SB) of the disk and such results, together with previous SEDs studies, confirmed the presence of a gap ending at the inner edge of the external belt at 45 AU.

HD202917 (see [23] and [25]). HD202917 is a member of the Tucana Horologium association with an infrared excess $L_{IR}/L_* \sim 2.5x10^{-3}$. The debris disk was previously resolved at visible wavelengths in formally unpublished images obtained with *Hubble Space Telescope*'s ACS coronagraph. Later its images were reprocessed through two filters and two telescope orientations and those robustly confirm the preliminary ACS detection, including the strong asymmetry between the east and west sides. The detection extends to projected distances of approximately 107 AU from the star and the inner edge of the outer belt is at ~ 55.4 AU. The disk exhibits an asymmetric arc of a partial ring inclined $\sim 70°$ to the line of sight with a major axis position angle $PA \sim 300°$. The northwest side is significantly brighter and more extended than the southeast side which, together with the similarly asymmetric ACS image, suggests a highly perturbed disk.

HD30447 (see [25]). HD30447 is a member of the Columba moving group, which also contains the exoplanet host star HR8799. Its disk appears nearly edge on with a position angle $PA \sim 35° \pm 5°$. The disk extends between projected distances of $\sim 60 - 200$ AU from the star. The brightness and extent of the northeast side of the disk are about twice those of the southwest side. The system has an infrared excess $L_{IR}/L_* \sim 7.9x10^{-4}$.

HD71155 (see [16] and [2]). It is resolved at 10.4 μm and the extent implies a disk radius of 2.0 ± 0.1 AU, at which the blackbody temperature is 499 ± 3 K. The excess was fitted with emitting particles that are efficient absorbers but inefficient emitters. This may be the case for particles which are larger than the peak wavelength of stellar emission but smaller than the peak wavelength of particle thermal emission.
HD71155 is also resolved at 70 μm and marginally at 100 μm. The weak constraints at 100 and 160 μm mean that this system is easily fit by a narrow ring with a radius of 68.7 AU and inclination of 56°.

HD218396 (see [15]). This system is a member of the Columba moving group and is better known as HR8799. It hosts a directly imaged multi-planet system and shows evidence for warm and cold dust disk components. Four planetary companions have been detected at projected separations of 15, 24, 38 and 68 AU. Evidence for a circumstellar dust disk has been known for some time and *Spitzer* observations have revealed that the disk must contain multiple dust components. In particular, the disk can be divided in three parts: a warm central component, an outer cold component extending from 90 to 300 AU and an external halo of small grains extending to an outer radius of 1000 AU. The disk have been resolved at 70, 100, 160 and 250 μm and detected at 350 and 500 μm. From this observations the inner edge of the external belt is placed at 100 AU, and with strong constraints on the position of the inner ring due to the presence of the innermost planet at 15 AU.

HD131835 (see [7]). It is a system probably in the Upper Centaurus Lupus (UCL) moving group (a subgroup of the Sco–Cen association). It is one of the only four UCL/Lower Centaurus Crux A-type stars with $L_{IR}/L_* > 10^{-3}$. HD131835 has a debris disk spatially resolved at mid-IR wavelengths. The system has grains at multiple spatial locations: a hot continuous component extends from ~ 35 AU to ~ 310 AU, a warm ring located at 105 AU and a cold ring located at ~ 220 AU. Models indicate that the two separated narrow rings are indeed embedded in an extended disk component. Although not all the model components are completely spatially separated, it is quite probable that the dust is not concentrated in a single belt. Since the continuous component starts at 35 AU we place there the inner edge of the outer part of the system.

HD95086 (see [26]). This star is an early-type member of the Lower Centaurus Crux association. HD95086 has drawn a lot of attention because it hosts a directly imaged planet HD95086b, at a projected distance of 56 AU and it also has a prominent infrared excess with a dust fractional luminosity $f_d \sim 1.6x10^{-3}$. The debris disk is marginally resolved at far-infrared wavelengths with *Herschel*, suggesting a slightly inclined orientation from face on. The analyzed spectrum covers the range $55 - 95$ μm. HD95086 owns three dust components: an inner warm narrow ring, an outer cold extended disk and a wide halo that extends to hundreds of AU from the star.
The resolved structure in this system most likely arises from the disk halo component made only of small grains that can be warm enough to emit efficiently at far-infrared wavelengths in order to account for the extended structure seen in the images. The disk halo component is found to have a inner radius at ~ 120 AU, that represents the boundary where its emission becomes dominant, while the outer radius is at $\sim$ 800 AU. For the cold disk component it was adopted $q = 3.5$ in equation (3.7) because it is quite extended, from ~ 63 AU to ~ 190 AU and the particles distribution for an unperturbed wide disk is most likely to have such distribution. For the inner warm component, on the other hand, it was adopted a steeper power law, $q = 3.65$, based on the hypothesis that the warm component is a narrow belt closer to the star where collisional cascades are expected to reach the equilibrium As the warm component is less constrained, the uncertainty from the SED fitting is large. Assuming a flat disk density distribution, the warm component gives a consistent fit to the shape of the IRS spectrum, with radii ranging from ~ 7 AU to ~ 10 AU. Thus, we choose an intermediate separation, placing the belt at 9 AU.

HD106906 (see [11]). It is a member of the Lower Centaurus Crux (LCC) and recently it was demonstrated that it is a close binary system, therefore called HD106906AB, of mass probably greater than 2.5 $M_\odot$ (even if due to the great uncertainties, we will use the mass of 1.5 $M_\odot$ as given in C10). A giant planet of ~ 11 M_J was detected by direct imaging to orbit the two stars at a projected separation of 650 AU, thus it is called a circumbinary planet. The system owns also a circumbinary disk the has been spatially resolved by SPHERE with a fractional luminosity of $L_{IR}/L_* = 1.4x10^{-3}$. The disk appears mostly as a highly inclined ring structure ($PA \sim 104.4°$) with the inner edge at ~ 66 AU and it extends over 110 AU and shows strong asymmetries. Thus, the imaged planet lives far from the gap and will not affect our analysis.

HD115600 (see [5]). It is a member of the Lower Centaurus and it shows large infrared excess with a debris disk fractional luminosity $L_{IR}/L_* = 1.7x10^{-3}$ and mass $M_{disk} = 0.005M_{moon}$. From resolved images the semi-major axis of the disk is placed at ~ 48 AU, it is nearly edge-on with a position angle $PA \sim 24°$ and an inclination $i = 79.5°$. Moreover, the dust particles show common eccentricities in the range $[0.1, 0.2]$ that are very likely to point to the presence of planets interior to the belt.

For what regards the left systems, HR4796 and HD61005, we use data from resolved images taken with SPHERE. Since these results have not yet been published, we present only the position of the edges found without further discussion.
We show in figure 5.4 how much the results of SEDs analysis differ from data available in resolved systems for the outer belts. We can see a consistent difference for systems with the external belt placed beneath 50 AU and the ones with such component positioned further out. Indeed, whereas for the former objects SEDs and direct imaging results are in good agreement, for the latter the positions furnished by direct imaging data are significantly nearer to the star than those obtained by SED fitting. Then, it seems that spectral energy distribution analysis works well for components of the debris disk quite near to the star. This trend is also confirmed by systems revealed by radial velocities technique in chapter 8: in this case, we compare the position of the inner belt as given by SED and as obtained by chaotic zone analysis. As it is clearly visible from figure 8.1 the two positions are in very good agreement, thus confirming reliability of the excess fitting for dust components near to the star (particularly beneath 50 AU). We show also in figure 5.5 a cumulative graphic in which we present the entire set of point of both figure 5.4 (blue circles) and 8.1 (green circles).
Such results are not at all a surprise since dust grains placed so far from the centre of the system have low temperatures (thus longer wavelengths) so that their $\lambda_{d,max}$ is less constrained and more difficult to determine.
However, the high discordance at great distances between SED and direct imaging analysis could be caused by other factors. For example, we mentioned in chapter 3 that some instruments that perform direct imaging use differential rotation fields so that all homogeneous components would be deleted from the images and this is not the case for SED data. Moreover, the resolved systems are analyzed at certain wavelengths depending on the instrumentation used and the disk will appear quite different for each value of λ. Instead, the excesses in the spectral energy distributions identify only the dust component. Thus, it is possible that images obtained with direct imaging technique show a debris disk component different from the SED's dust grains and, consequently, quite different positions.
From the previous discussion, it should be clear that even if direct imaging help us to better constrained some features of the system it does not tell us all the truth about what we are observing and we can not invalidate by means of it results obtained by SED analysis.

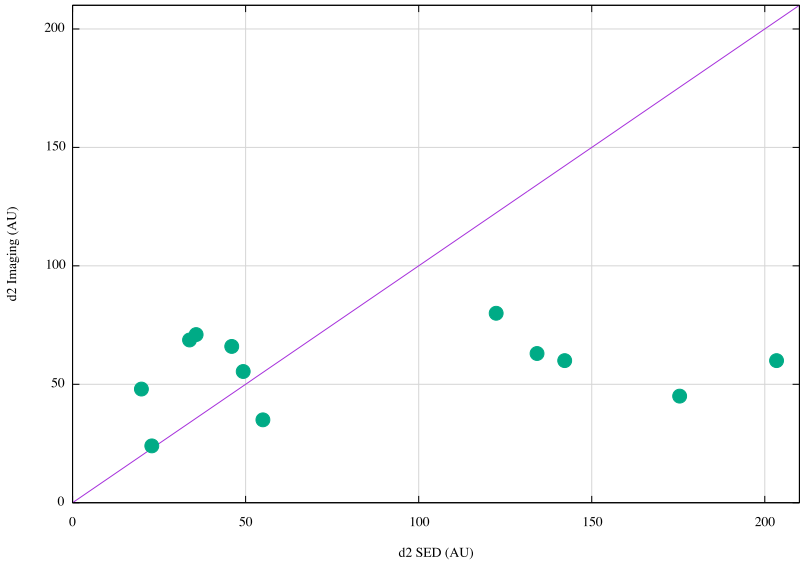

Figure 5.4: Position of the outer belts as obtained from SED analysis and from resolved systems. The purple line represents the bisector, id est when the two positions coincides.

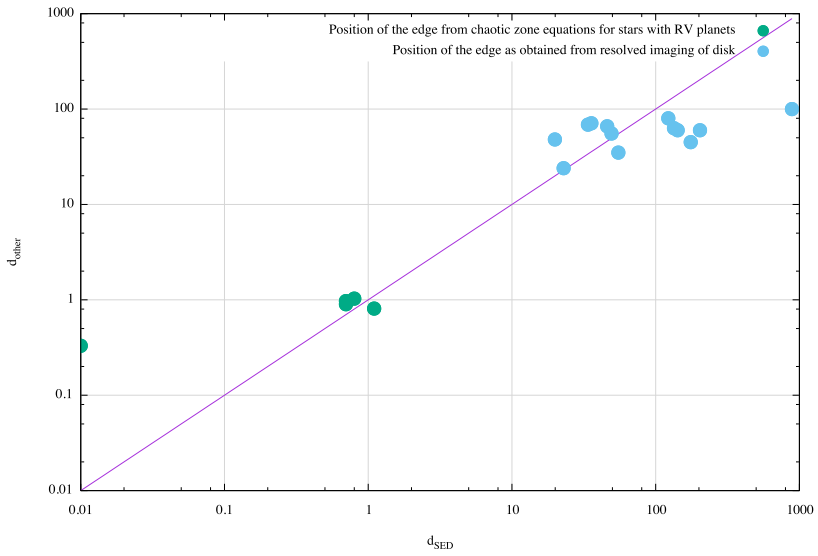

Figure 5.5: Positions of the belts as obtained from SED analysis and from resolved images of the disks (blue circles) or form chaotic zone analysis in systems with known radial velocities planets (green circles). The purple line represents the bisector, id est when the two positions coincides.

Table 5.1: Stellar parameters for direct imaged systems with SPHERE.

Name	Spectral Type	$\frac{M_*}{M_\odot}$	Age (Myr)	Distance (pc)
HD174429	G9	1	12	49.7
HD181327	F6	1.3	12	50.6
Eta Tel	A0	2.2	12	47.7
HD15115	F2	1.3	12	44.8
HD43989	F9	1.1	30	49.8
HD202917	G7	0.9	30	45.9
HD30447	F3	1.3	30	78.1
HD71155	A0	2.4	306	38.3
HR4796	A0	2.3	8	67.1
HD61005	G8	0.9	50	34.5
HD75416	B8	3	8	96.9
Beta Leo	A3	1.9	45	11.1
HD219482	F6	1	300	20.6
HD178253	A2	2.2	254	39.8
HD135379	A3	2	166	29.6
HD218396	A5	1.5	30	39.9
HD220825	A0	2.1	70	49.7
HD24636	F3	1.3	30	54.9
HD192425	A2	2.1	408	47.1
HD141378	A5	1.9	478	49.2
HD122705	A2	1.8	16	106.7
HD131835	A2	1.9	16	111.1
HD95086	A8	1.6	17	91.6
HD107301	B9	2.4	17	99
HD118588	A1	2	17	116
HD106906	F5	1.5	17	91.8
HD115600	F2	1.5	17	111.2
HD203	F3	1.4	12	39.1
HD164249	F5	1.3	12	46.9
HD1466	F8	1.1	30	41
HD3003	A0	2.1	30	46.5
HD32195	F7	1.1	30	60.4
HIP6276	G9	0.9	70	35.1
HD25457	F6	1.2	70	19.2
HD188228	A0	2.3	40	32.5
HD84075	G2	1.1	40	63
HD113457	A0	2.1	17	95.1
HD114082	F3	1.5	17	83.1
HD133803	A9	1.6	16	97.2
HD140840	B9	2.3	16	118.3

Table 5.2: Debris disks parameters for direct imaged systems with SPHERE.

Name	$T_{gr,1}$(K)	d_1(AU)	$T_{gr,2}$(K)	d_2(AU)	Solved	d_1(AU)	d_2(AU)
HD174429	460	0.7	39	439.4	NO		
HD181327	94	30	60	122.4	YES		80
Eta Tel	277	4	115	22.9	YES		24
HD15115	182	5	54	175.4	YES		45
HD43989	319	1.4	66	85.7	NO		
HD202917	289	2	75	49.3	YES		55.4
HD30447	106	20	57	142.2	YES		60
HD71155	499	2.5	109	33.8	YES	2	68.7
HR4796	231	6	97	35.7	YES		71
HD61005	78	42.7	48	203.4	YES		60
HD75416	393	5.1	124	45	NO		
Beta Leo	499	1.3	106	24.8	NO		
HD219482	423	0.9	78	46	NO		
HD178253	307	4.1	100	36.6	NO		
HD135379	387	2	155	11.1	NO		
HD218396	155	8.4	33	887.8	YES		100
HD220825	338	3.1	170	10.8	NO		
HD24636	319	1.6	103	23.2	NO		
HD192425	268	4.3	66	88.8	NO		
HD141378	347	2.2	69	78.2	NO		
HD122705	387	1.7	127	15	NO		
HD131835	216	5	78	55	YES		35
HD95086	225	4.1	57	134.2	YES	9	63
HD107301	246	7.4	127	26.4	NO		
HD118588	292	2.9	133	14.1	NO		
HD106906	124	14	81	46	YES		66
HD115600	499	1	109	19.9	YES		48
HD203	499	0.9	127	12.8	NO		
HD164249	100	24.6	57	147.2	NO		
HD1466	374	1.1	97	26.5	NO		
HD3003	472	1.6	173	9.2	NO		
HD32195	246	2.3	69	73	NO		
HIP6276	344	1	63	83.1	NO		
HD25457	185	4.7	63	105	NO		
HD188228	185	9.4	72	71.9	NO		
HD84075	149	7.7	54	167.2	NO		
HD113457	319	3.1	142	14.3	NO		
HD114082	499	0.8	112	18.9	NO		
HD133803	368	1.4	142	10.2	NO		
HD140840	341	2.6	88	43.3	NO		

Chapter 6

Single planets

The sample of objects shown in chapter 5 has one leading characteristic: all those systems own two planetesimals belts. Between the inner and the outer one, we assume the presence of a gap free from particles and, as responsible for this vacuum space, one or more planets. In fact, as we have seen before, a planet orbiting its star produces around its orbit an entire chaotic zone from which all particles are swept away. Thus, we are going to use the positions of the two belts and the gap in the middle as a signpost for planets.
In this chapter we are going to investigate the presence of a single planet in the system. In the first and second paragraph we are going to resume formulas obtained by previous works and the numerical simulations we have performed in order to adapt them to our necessities. Finally, we present our result for what regards the eccentricity, mass and detectability of the planet in each system.

6.1 General physics

We have already said that a planet sweeps an entire zone around its orbit that is proportional to its semi-major axis and to a certain power law of the ratio μ between its mass and the mass of the star.
One of the first to reach a fundamental result in this field was Wisdom ([27]) who performed the stability of dynamical systems for a non linear Hamiltonian with two degrees of freedom. He divided the phase space into regions which contain massless particles on quasi-periodic trajectories, for which long term stability is possible, and others in which trajectories had a random, non periodic character. Using the approximate criterion of the zero order resonance overlap for the planar circular-restricted three-body problem, he derived the famous formula for the chaotic zone that surrounds the planet

$$\Delta a = 1.3\mu^{2/7} a_p, \tag{6.1}$$

where Δa is the half width of the chaotic zone, μ the ratio between the mass of the planet and the star, a_p is the semi-major axis of the planet. As it is clear from the previous discussion, such result is only valid for planets on circular orbits around their stars.
After this analytic result, many numerical integrations have been performed in order to achieve similar equations. One particular interesting expression regards

the clearing zone of a planet on a circular orbit that was derived by Morrison & Malhotra ([18]). Differently from the chaotic region, in which particles become unstable after some time they spend in there, when a dust grain enters the clearing zone it is suddenly ejected from the area around the trajectory of the planet. The formulas for such zones interior and exterior to the orbit of the planet are

$$(\Delta a)_{in} = 1.2\mu^{0.28} a_p \tag{6.2}$$

$$(\Delta a)_{ext} = 1.7\mu^{0.31} a_p. \tag{6.3}$$

The last result we want to underline is the one obtained by Mustill & Wyatt ([20]) using again N-body integrations and taking into account also the eccentricities e of the particles. Indeed, particles in a debris disk can have many different eccentricities even if the majority of them follows a common stream with a certain value of e. The expression for the half width of the chaotic zone in this case is given by

$$\Delta a = 1.8\mu^{1/5} e^{1/5} a_p. \tag{6.4}$$

The chaotic zone is thus larger for greater eccentricities of particles. The equation (6.4) is only valid for values of e greater than a critical eccentricity, e_{crit}, given by

$$e_{crit} \sim 0.21\mu^{3/7}. \tag{6.5}$$

For $e < e_{crit}$ this result in not valid anymore and equation (6.1) is more suitable. Even if each particle can have an eccentricity due to interactions with other bodies in the disk, such as for example collisional scattering or disruption of planetesimals in smaller objects with resulting high values of e, one of the main effects that lies beneath global eccentricity in a debris disk is the presence of a planet on eccentric orbit. Indeed, Mustill & Wyatt ([19]) obtained another fundamental result for forced eccentricities on planetesimal and dust grains due to the close approach of a planet with high e_p, given by

$$e_{f,in} \sim \frac{5ae_p}{4a_p} \tag{6.6}$$

$$e_{f,ex} \sim \frac{5a_p e_p}{4a}, \tag{6.7}$$

where $e_{f,in}$ and $e_{f,ex}$ are the forced eccentricities for disk interior and exterior to the orbit of the planet, respectively; a_p and e_p are, as usual, semi-major axis and eccentricity of the planet, while a is the semi-major of the disk. It is of common use to take the eccentricities of the planet and disk as equal, because this latter is actually caused by the presence of the perturbing object. Such approximation is also confirmed by equations (6.6) and (6.7). Indeed, the term 5/4 is balanced by the ratio between the semi-major axis of the planet and that of the disk since, in our assumption, the planet gets very close to the edge of the belt and thus the values of a_p is not so different from that of a, giving $e_f \sim e_p$.

6.2 Numerical simulation

From the previous paragraph it should be clear that no real formulation does actually exists for the chaotic zone of a planet moving on an orbit with a certain eccentricity e_p. The first part of our analysis consists in taking one single planet

as the only responsible for the lack of particles between the edges of the inner and external belt. As we will see, but it is an expected conclusion, the hypothesis of circular motion is not suitable for almost all systems analyzed for masses under 21 M_J (well above the brown dwarf limit of 13 M_J). For this reason, introduce eccentric orbits is of extreme importance in order to derive a complete formulation for the case of single planet.
The approximation that we will use consists in a substitution in equations (6.1) and (6.4) of the value of the mean radius, a_p, with the positions of apoastron and periastron in turn. We thus get the following equations

$$(\Delta a)_{ex} = 1.3\mu^{2/7} apo \tag{6.8}$$

$$(\Delta a)_{in} = 1.3\mu^{2/7} peri, \tag{6.9}$$

which substitute Wisdom formula (6.1), and

$$(\Delta a)_{ex} = 1.8\mu^{1/5} e^{1/5} apo \tag{6.10}$$

$$(\Delta a)_{in} = 1.8\mu^{1/5} e^{1/5} peri, \tag{6.11}$$

which substitute Mustill & Wyatt's equation (6.4) and in which we choose to take as equal the eccentricities of the particles in the belt and that of the planet, $e = e_p$. The substitution of a_p with apoastron and periastron is somehow similar to consider the planet as split into two objects, one of which is moving on circular orbit at the periastron and the other on circular orbit at apoastron and both with mass M_p.
Before using our approximation, we want to verify it by means of N-body numerical integrations. Thus, we place a planet of 1 M_J around a star of 1 $M_\odot$ and two belts, external and internal to the orbit of the planet, composed of massless objects. The planet has a semi-major axis of 5 AU and eccentricities of 0, 0.3, 0.5 and 0.7 in turn in four different simulations. We firstly do a stability analysis on the semi-major axis of the particles and then modeled the disk with 4000 bodies, obtaining the limits on its radial distribution. We show our results for $e_p = 0.3$ in figure 6.1 where we plot the fraction of bodies that are not ejected from the system as a function of their radii. Green lines represent the results of the stability integration while red lines represent the radial distribution of the disk.

As next step, we have to choose where to place the inner and outer edges of the outer and inner belts. Arbitrarily, we choose as d_2 and d_1 the values for which the radial distribution is equal to 1/3 with respect to the peak. In order to have a term of comparison we also use the values for which it is 1/4 of the peak. We show these results in table 6.1 and 6.2. The first three columns regard our simulations and are the eccentricity of the planet, the cut off chosen (1/3 or 1/4) and the position obtained by the distributions; the last two columns are instead the positions of the belts that we obtained in first place, calculating the half width of the chaotic zone from equations (6.9) and (6.11) for the inner belt and (6.8) and (6.10) for the outer one, and then we use the relations

$$(\Delta a)_{in} = peri - d_1 \tag{6.12}$$

$$(\Delta a)_{ex} = d_2 - apo \tag{6.13}$$

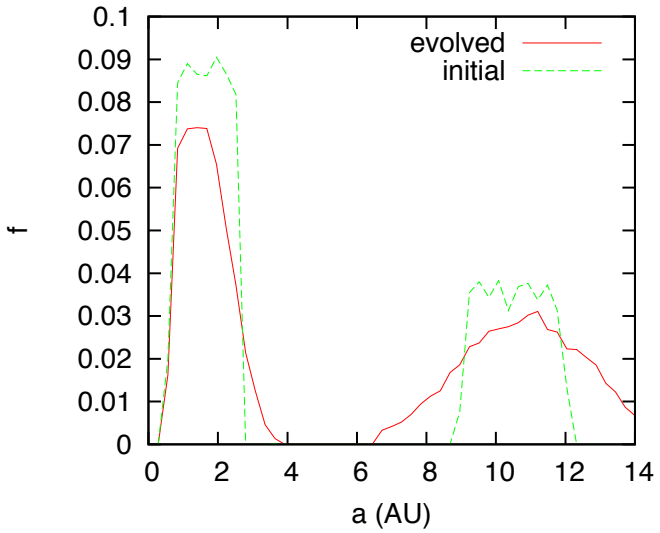

Figure 6.1: Numerical simulation for a planet of 1 M_J around a star of 1 $M_\odot$ with a semi-major axis of 5 AU and eccentricity of 0.3. We plot the fraction of bodies that are not ejected from the system as a function of the radius. Green lines represent the stability analysis on the semi-major axis of the disk. Red lines represent the radial distributions of 4000 objects.

obtaining, in the end, d_1 and d_2.
We plot the positions of the two belts against the eccentricity for cut off of 1/3 and 1/4 in figure 6.2. As we can see, results from simulations are in good agreement with our approximation. Particularly, we note how Wisdom is more suitable for eccentricities up to 0.3 (result that has already been proposed in a paper by Quillen ([12]) in which the main conclusion was that particles in the belt do not feel any difference if there is a planet on circular or eccentric orbit for $e_p \leq 0.3$), whereas for grater values of e_p also equations (6.10) and (6.11) give reliable results.

e_p	cut	d_1(AU)	Wisdom	Mustill
0	1/3	4.48	4.11	4.11
0	1/4	4.48	4.11	4.11
0.3	1/3	2.8	2.88	2.27
0.3	1/4	3.1	2.88	2.27
0.5	1/3	1.96	2.05	1.53
0.5	1/4	2.24	2.05	1.53
0.7	1/3	1.32	1.23	0.87
0.7	1/4	1.38	1.23	0.87

Table 6.1: Position of the inner belt

e_p	cut	d_2(AU)	Wisdom	Mustill
0	1/3	6.26	5.89	5.89
0	1/4	6.26	5.89	5.89
0.3	1/3	7.84	7.66	8.79
0.3	1/4	7.56	7.66	8.79
0.5	1/3	9.52	8.84	10.42
0.5	1/4	9.24	8.84	10.42
0.7	1/3	11.0	10.02	12.05
0.7	1/4	10.79	10.02	012.05

Table 6.2: Position of the outer belt

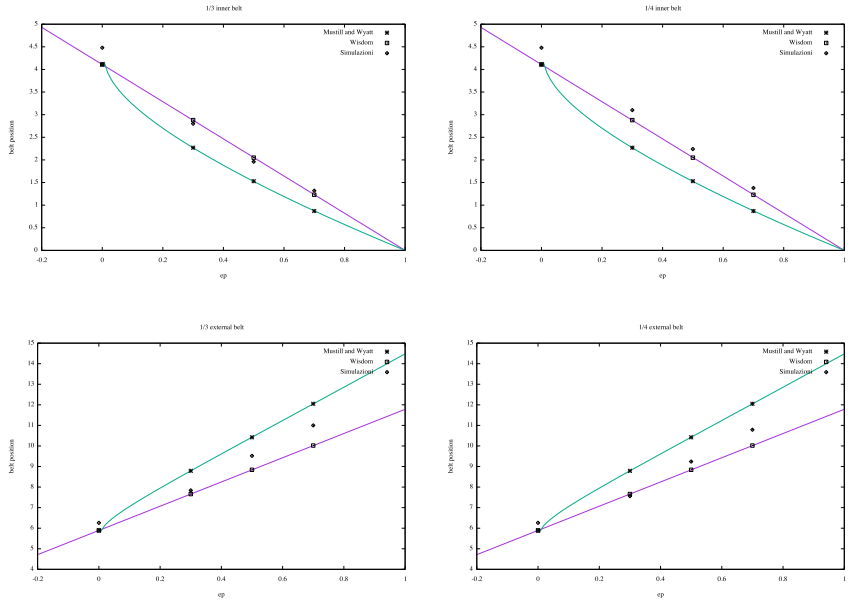

Figure 6.2: The upper figures represent the position of the inner belt for cuts off of 1/3 (left) and 1/4 (right). The lower images represent the position of the external belt for the same cuts off.

6.3 Data analysis

Once we have verified the goodness of our approximation, we can go on to analyze the dynamics of our systems.
The first assumption we test is a single planet on circular orbit around its star. We use the equations for the clearing zone of Morrison & Malhotra (6.2) and (6.3). We vary the mass of the planet between 0.1 M_J, i. e. Neptune/Uranus sizes, to 21 M_J (that is well over the brown dwarf limit of 13 M_J) in order to find the value of M_p, and the corresponding value of a_p, at which the planet would sweep an area as wide as the gap between the two belts. Since $(\Delta a)_{in}+(\Delta a)_{ex} = d_2 - d_1$, knowing M_p, we can obtain the semi-major axis of the planet by

$$a_p = \frac{d_2 - d_1}{1.2\mu^{0.28} + 1.7\mu^{0.31}}. \tag{6.14}$$

Just for one system, HD61005, we find a value for the planet on circular orbit in the range $[0.1, 21]$ M_J, precisely $M_p = 0.8$ M_J(well below the detection limits curve for this system), at a separation of 50 AU.
Since we get no satisfactory results for the circular case, we move to consider one planet on eccentric orbit. We use the approximation illustrated in the previous paragraph with one further assumption: we consider the apoastron of the planet as the point of the orbit nearest to the external belt while the periastron as the nearest point to the inner one. We let again vary the masses in the range $[0.1, 21]$ M_J and, from equations (6.8), (6.9), (6.10) and (6.11), we get the values of periastron and apoastron for both the Wisdom and Mustill &

Wyatt formulations, recalling also equations (6.12) and (6.13). Therefore, we can deduce the eccentricity of the planet through

$$e_p = \frac{apo - peri}{apo + peri}. \tag{6.15}$$

The careful reader should have noticed that the equation (6.4) contains itself the eccentricity of the planet e_p, that is our unknown. The expression to solve in this case is

$$e_p - \frac{d_2(1 - 1.8(\mu e_p)^{1/5}) - d_1(1 + 1.8(\mu e_p)^{1/5})}{d_2(1 - 1.8(\mu e_p)^{1/5}) + d_1(1 + 1.8(\mu e_p)^{1/5})} = 0 \tag{6.16}$$

and we are not able to find an analytic solution. We therefore perform an iterative analysis, varying, for each values of M_p, the eccentricity in the range [0.1,1] in order to find the best value of e_p for which the expression (6.16) is approximately verified. We can now plot the variation of the eccentricity as a function of the mass. We present two of this graphics, as examples, in figure 6.3 and all the others in Appendix B. In each graphic there are two curves (with

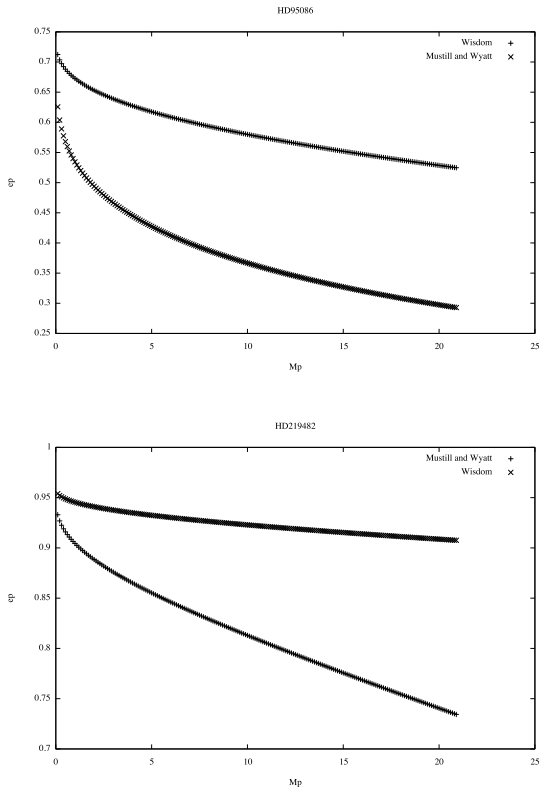

Figure 6.3: e_p VS M_p for HD95086 (up) and HD219482 (down)

the only exception of HD61005 that has three curves) one of which represents the analysis carried on with Wisdom formulation and the other with Mustill & Wyatt expressions. In both cases, the eccentricity decreases with increasing

planet mass. This is an expected result since a less massive planet has a tighter chaotic zone and needs to come nearer to the belts in order to separate them of an amount $d_2 - d_1$, that is fixed by the observations (and viceversa for a more massive planet that would have a wider Δa). Moreover, we note that the curve that represents Mustill & Wyatt's formulas decreases more rapidly than Mustill's curve does. This is due to the fact that equation (6.4) takes into account also the eccentricity of the planetesimals (in our case $e = e_p$) and thus Δa is wider.

Comparing the graphics of the two systems we note that whereas for HD95086, for increasing mass, the eccentricity reaches quite low values (~ 0.3), HD219482 needs planets on very high eccentric orbits even at large masses. Recalling table 6.1, the separation between the belts in HD95086 is of 54 AU whereas in HD219482 is only 45.1 AU. So how come that in the first system planets with smaller eccentricity are needed to dig a gap larger than the one in the second system? The explanation regards the positions of the two belts: HD95086 has the inner ring placed at 9 AU whereas HD219482 at 0.9 AU. From equations (6.1) and (6.4) we obtain a chaotic zone that is larger for further planets since it is proportional to a_p.

From the previous discussion, we deduce that many factors in debris disks are important in order to characterize the properties of the planetary architecture of a system, first of all the radial extent of the gap between the belts, the wider the more massive and/or eccentric planets needed, but also the positions of the belts (the nearer to the star, the more difficult to sculpture) and the mass of the star itself. For most of our systems the characteristics of the debris disks are not so favorable to host one single planets, since we would need very massive objects that have not been detected. For this reason we move to dynamically analyze the presence of two or three planets around each star.

Before moving to multiple planetary systems, however, we want to apply our analysis, with which we get the eccentricity, semi-major axis and mass of the planet, to the detection limits available in the ensemble. We show, as an example, the graphics for HD95086 in figure 6.4 in which we plot the detection limits curve, the positions of the two belts (the vertical black lines) and three values of the mass $M_p = 2, 5, 17 M_J$. From the previous method we can associate at each value of the mass a value of a_p and e_p. Thus, in the graphic, the bar plotted for each M_p represents the interval of distances covered by the planet during its orbit, from a minimum distance (periastron) to the maximum one (apoastron) from the star. Since, however, Wisdom and Mustill & Wyatt give different relations between e_p and M_p, we plot our results in two different graphics. Moreover, we choose these three values of masses because they represent well the three kinds of situations that we could find: for 2 M_J the planet is always under the curve of the detection limits and so never detectable; for 5 M_J the planet crosses the curve and thus it is at certain radii of its orbit detectable and at others undetectable (we note however that the planet spends more time at apoastron than at periastron so that it is more likely detectable in this case); the last value of M_p is always detectable, even when it is at its periastron, since always above the curve.

We present in Appendix B the analogous analysis for each system with detection limits curve available.

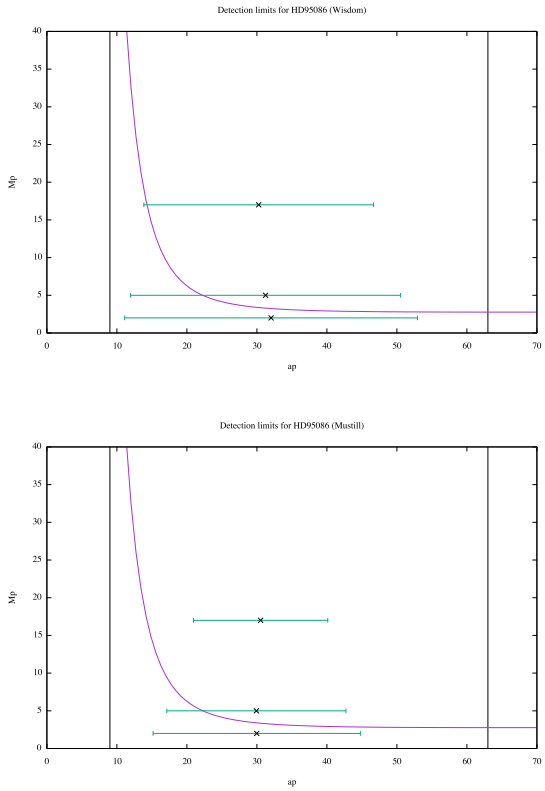

Figure 6.4: Detection limits for HD95086 compared by some of the results by previous analysis using Wisdom (up) and Mustill & Wyatt (down) formulations

Chapter 7

Multiple planets

In perfect analogy with our Solar System, we can imagine that in the space between the two belts lives more than one planet. Indeed, in the gap that goes from the asteroid to the Kuiper belt we find four giant planets quasi-coplanar on nearby circular orbits. Assuming the multiple-planetary architecture as a likely feature of extrasolar systems, in this chapter we want to analyze the characteristic of a system with two coplanar planets on circular and eccentric orbits and three planet on circular orbits.

7.1 General physics

7.1.1 Two planets

In order to analyze the stability of a system with two planets, we have to characterize the zone between the two. Indeed, untill now we have considered the system as composed by two massive objects, the star and the planet, and a great number of massless particles for which the stability regions were established by equations like Wisdom or Mustill & Wyatt. With two planets in the system, the massive bodies become three and we need another criterion in order to describe the interaction between the planets, the most used of which is the Hill one.
Let us consider a system with a star of mass M_*, the inner planet with mass $M_{p,1}$, semi-major axis of $a_{p,1}$ and eccentricity $e_{p,1}$, and the outer one with mass $M_{p,2}$, semi-major axis $a_{p,2}$ and eccentricity $e_{p,2}$. In the hypothesis of small planets' masses, i.e. $M_{p,1} << M_*$, $M_{p,2} << M_*$ and $M_{p,2} + M_{p,1} << M_*$, the system will be Hill stable (Gladman, [6]) if

$$\alpha^{-3}\Big(\mu_1 + \frac{\mu_2 2}{\delta^2}\Big)(\mu_1\gamma_1 + \mu_2\gamma_2\delta)^2 \geq 1 + 3^{4/3}\frac{\mu_1\mu_2}{\alpha^{4/3}}, \tag{7.1}$$

where μ_1 and μ_2 are the ratio between the mass of the inner/outer planet and the star respectively, $\alpha = \mu_1 + \mu_2$, $\delta = \sqrt{1 + \Delta/a_{p,1}}$ with $\Delta = a_{p,2} - a_{p,1}$ and, at the end, $\gamma_i = \sqrt{1 - e_{p,i}^2}$ with $i = 1, 2$.
If the two planets in the system have equal masses, the previous equation, taking $M_{p,2} = M_{p,1} = M_p$ and $\mu = M_p/M_*$, can be rewritten in the form

$$\alpha^{-3}\Big(\mu + \frac{\mu}{2\delta^2}\Big)(\mu\gamma_1 + \mu\gamma_2\delta)^2 - 1 - 3^{4/3}\frac{\mu^2}{\alpha^{4/3}} \geq 0 \tag{7.2}$$

and substituting the expressions for α, δ, Δ and γ_i we obtain

$$\frac{1}{8}\Big(1+\frac{a_{p,1}}{a_{p,2}}\Big)\Big(\sqrt{1-e_{p,1}^2}+\sqrt{1-e_{p,2}^2}\sqrt{\frac{a_{p,2}}{a_{p,1}}}\Big)^2-1-\Big(\frac{3}{2}\Big)^{4/3}\mu^{2/3}\geq 0. \quad (7.3)$$

Thus, the dependence of the stability on the mass of the two planets, in the case of equal masses, is very small since it appears only in the third term of the previous equation in the form $\mu^{2/3}$, with $0 \leq \mu \leq 1$. The leading terms that determine the dynamic of the system are the eccentricities $e_{p,1}$ and $e_{p,2}$. For this reason, we expect that small variation in the eccentricities will lead to great variation in masses.
A further simplification to the problem comes when we consider two equal-mass planets on circular orbits. In this case the stability equation (7.1) takes the contracted form

$$\Delta \geq 2\sqrt{3}R_H, \quad (7.4)$$

where Δ is the difference between the radii of the planets' orbits and R_H is the planets mutual Hill radius that, in the general situation, is given by

$$R_H = \Big(\frac{M_{p,1}+M_{p,2}}{3M_*}\Big)^{1/3}\Big(\frac{a_{p,1}+a_{p,2}}{2}\Big). \quad (7.5)$$

In the following, we will do analysis for both the circular and eccentric case with two planets of equal mass.

7.1.2 Three planets

The last case that we present is a system with three coplanar and equal-mass giant planets on circular orbits. The physics follows from the previous discussion since the stability zone between the first and the second planet, and between the second and the third is again well described by the Hill criterion. Once fixed the inner planet semi-major axis $a_{p,1}$, the semi-major axis of the second and third planet are given by

$$a_{p,i+1} = a_{p,i} + KR_{Hi,i+1} \quad (7.6)$$

where K is a constant that depends on the mass of the planets and $R_{Hi,i+1}$ is the mutual Hill radius between the first and the second planet for $i = 1$ and between the second and the third for $i = 2$. K produces parametrizations curves, called K-curves, that are weakly constrained. However, we can associate at K likely values that give us a clue of the architecture of the system. The most used values of K are:

- $K \sim 8$ for Neptune-size planets;
- $K \sim 7$ for Saturn-size planets;
- $K \sim 6$ for Jupiter-size planets .

There is no analysis in literature that explores the case of three or more planets with different masses and/or eccentric orbits. Thus, it would be worth doing further investigations even if they go beyond the intents of this work.

7.2 Data analysis

7.2.1 Two and three planets on circular orbits

The first kind of analysis that we perform consists in taking into account two coplanar planet on circular orbits. In this case, between the two belts the system is divided in three different zones from a stability point of view. The first one extends from the outer edge of the internal disk to the inner planet and it is determined from laws of interaction between two massive bodies (the star and the planet) and N massless objects. The second zone is included between the inner and the outer planet and is dominated by the Hill's stability. Eventually, the third zone goes from the outer planet to the inner edge of the external belt and is an analog of the first one.
From equation (7.4) we note that a system with two planets is stable if $\Delta = a_{p,2} - a_{p,1}$ is greater or equal to a certain quantity. However, since we do not observe any amount of dust grains in the region between the planets we expect it to be completely unstable for small particles. Therefore, in order to reach such situation but, nevertheless, to maintain the system Hill stable we have to impose the condition of max packing, thus

$$a_{p,2} - a_{p,1} = 2\sqrt{3}\Big(\frac{2M_p}{3M_*}\Big)^{1/3}\Big(\frac{a_{p,1} + a_{p,2}}{2}\Big). \tag{7.7}$$

The other two equations that we need are the ones of Morrison & Malhotra, (6.2) and (6.3), from which we obtain $a_{p,1}$ and $a_{p,2}$ in the form

$$a_{p,1} = \frac{d_1}{1 - 1.2\mu^{0.28}} \tag{7.8}$$

$$a_{p,2} = \frac{d_2}{1 + 1.7\mu^{0.31}} \tag{7.9}$$

and substituting in (7.7) we get

$$\begin{aligned} d_2 - d_1 = {} & \sqrt{3}\Big(\frac{2}{3}\Big)^{1/3}\mu^{1/3}(d_1 + d_2) + \\ & + \sqrt{3}\Big(\frac{2}{3}\Big)^{1/3}(d_1 1.7\mu^{0.31+1/3} - d_2 1.2\mu^{0.28+1/3}) + 1.2d_2\mu^{0.28} + d_1 1.7\mu^{0.31}. \end{aligned} \tag{7.10}$$

This is a very complex equation to solve for M_p and we need to make some simplifications. We note that all the exponents of μ have very similar values with the exception of the two μ in the third term on the right side of the equation in which, however, the exponents are about double of all others. Thus, we choose as a mean value $\mu^{0.31}$ and in the third term $\mu^{0.62}$ for both terms in the brackets. Calling $x = \mu^{0.31}$ we have now to solve the quadratic equation

$$\sqrt{3}\Big(\frac{2}{3}\Big)^{1/3}(1.2d_2 - 1.7d_1)x^2 - \Big(1.2d_2 + 1.7d_1 + \sqrt{3}\Big(\frac{2}{3}\Big)^{1/3}(d_1 + d_2)\Big)x + d_2 - d_1 = 0. \tag{7.11}$$

And now we can finally obtain the value of M_p, given the positions of the two belts and the mass of the star

$$M_p = M_* \left(\frac{1.2d_2 + 1.7d_1 + \sqrt{3}\left(\frac{2}{3}\right)^{1/3}(d_1 + d_2)}{2\sqrt{3}\left(\frac{2}{3}\right)^{1/3}(1.2d_2 - 1.7d_1)} - \right.$$
$$\left. - \frac{\sqrt{\left(1.2d_2 + 1.7d_1 + \sqrt{3}\left(\frac{2}{3}\right)^{1/3}(d_2 + d_1)\right)^2 - 4\sqrt{3}\left(\frac{2}{3}\right)^{1/3}(1.2d_2 - 1.7d_1)(d_2 - d_1)}}{2\sqrt{3}\left(\frac{2}{3}\right)^{1/3}(1.2d_2 - 1.7d_1)} \right)^{10/31}. \tag{7.12}$$

Even if this last is not an amenable formula, it works quite well, as confirmed by the iterative method that we have also applied to the case of two planets on circular orbit with equal mass. In this case we put no upper limit on the masses of the planets but we consider only masses bigger than 0.1 M_J. We note, however, that masses above 13 M_J have to be considered quite unlikely for this configuration.
The case of three planets of equal mass on circular orbits is quite similar. This time we have four zones of instability for the particles: the first and the fourth are determined by the inner and the outer planet assuming equations (6.2) and (6.3) respectively, while the second and the third by the Hill criterion.
Recalling equation (7.6), we can express the mutual dependence between the positions of the three planets as

$$a_{p,2} = a_{p,1} + K\left(\frac{2M_p}{M_*}\right)^{1/3} \frac{a_{p,1} + a_{p,2}}{2} \tag{7.13}$$

$$a_{p,3} = a_{p,3} + K\left(\frac{2M_p}{M_*}\right)^{1/3} \frac{a_{p,2} + a_{p,3}}{2}. \tag{7.14}$$

We can obtain $a_{p,2}$ from equation (7.13) and substituting it in (7.14) we get

$$a_{p,3} = a_{p,1} \frac{\left(1 + \frac{K}{2}\left(\frac{2}{3}\mu\right)^{1/3}\right)^2}{\left(1 - \frac{K}{2}\left(\frac{2}{3}\mu\right)^{1/3}\right)^2}, \tag{7.15}$$

where $a_{p,2}$ and $a_{p,3}$ are determined by equations (6.2) and (6.3). The final expression to solve for M_p becomes

$$\frac{d_2}{d_1}\frac{1 - 1.2\mu^{0.28}}{1 + 1.7\mu^{0.31}} = \frac{\left(1 + \frac{K}{2}\left(\frac{2}{3}\mu\right)^{1/3}\right)^2}{\left(1 - \frac{K}{2}\left(\frac{2}{3}\mu\right)^{1/3}\right)^2}. \tag{7.16}$$

In this case we use only the iterative method imposing, in analogy with the previous analysis, a lower limit on the mass at 0.1 M_j but not an upper one. The values of K are the ones described in the previous paragraph, with $K = 8$ for masses up to 0.3 M_J, $K = 7$ for masses in the range $[0.3, 0.9]M_J$ and $K = 6$ for $M_p \geq 1M_J$.

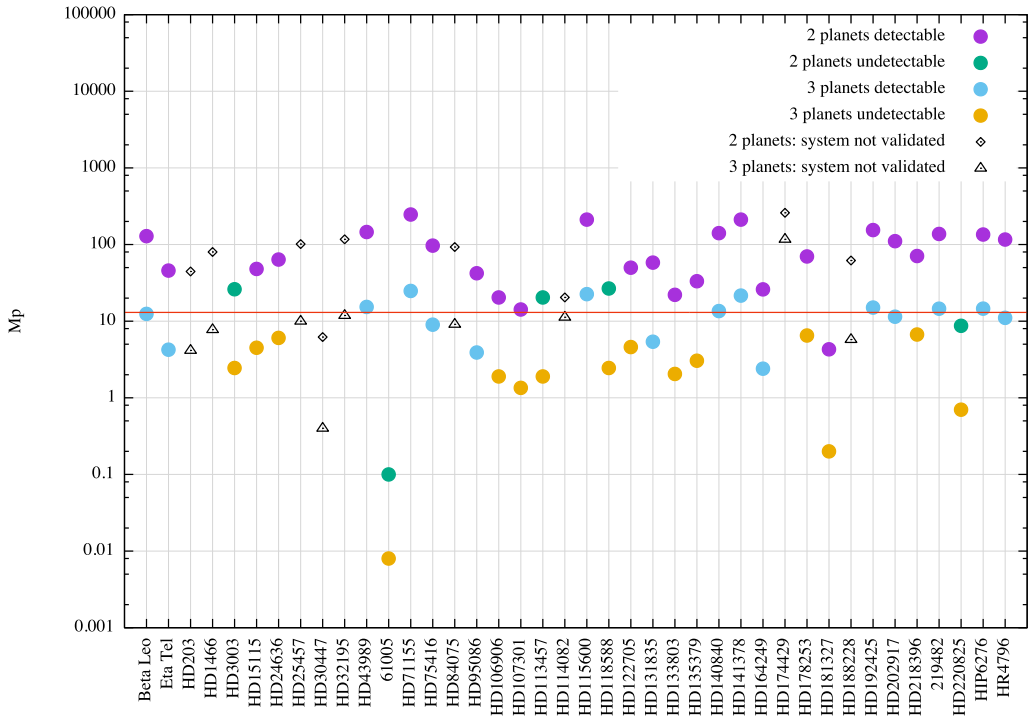

Figure 7.1: Masses (M_p/M_J) for the forty systems analyzed with two and three planets on circular orbits: purple and green circles represent a system with two planets that are detectable and undetectable respectively, while blue and yellow circles represent three planets detectable and undetectable respectively. Rhombus and triangles represent instead systems with two and three planets respectively for which observations where not validated and thus no detection limits curves are available.

Results of the analysis of two and three planets on circular orbits are shown in figure 7.1. For each system studied we plot the values of masses for the two and three planets models discussed in this paragraph. Together with these data, we indicate the detectability of such planets comparing their masses and semi-major axis with detection limits of Appendix A, when available. The condition for detectability in this case is that at least one object in the two or three planets model is above the detection limits curve. For systems with not validated observations and, thus, with no detection limits curves we merely plot the results of the previous analysis. As mentioned before, we put no upper limit to the range of masses but, however, we show the brown dwarf limit $M_p = 13 M_J$ that we assume as the upper acceptable value for the planets masses.
With the exception of HR4796 and HD95086, no giants planets have been discovered between the two belts in the systems of our ensemble using direct imaging techniques. Thus, we expect that if planets are indeed present, they must be undetectable for our instruments. In the great part of the systems, two planets on circular orbits would have been detected, since large masses, well above the 13 M_J, are required. The situation quite improves for the three planets model

because now many systems own undetectable objects. Therefore, in most cases, the assumption of three equal mass planets on circular orbits is more suitable than the one with two planets with the same characteristics.
Obviously in this paragraph we have made very restrictive hypothesis: circular orbits and equal mass planetary systems. Varying these two assumptions would give many suitable combinations in order to explain what we do (or do not) observe.

7.2.2 Two planets on eccentric orbits

The last model we want to investigate is two equal-mass planets on eccentric orbits. The system is again divisible in three regions of stability. The zone between the two planets follows the Hill criterion for the condition of max packing given by equation (7.3) with the equal sign. For the outer and inner regions the force is exerted by the planets on the massless bodies in the belts. This time, however, we will use Wisdom and Mustill & Wyatt expressions instead of Morrison & Malhotra's, suitable only for the circular case. Precisely, we apply the equation of Wisdom for eccentricities up to 0.3 whereas for greater values of e_p we use Mustill & Wyatt, together with the substitution of a_p with apoastron and periastron of the planets.
We have four different situations:

- if $e_{p,1}$ and $e_{p,2}$ are both ≤ 0.3, then we used equations of Wisdom (6.8) and (6.9), from which we obtain $a_{p,1}$ and $a_{p,2}$ in the form

$$a_{p,1} = \frac{d_1}{1 - 1.3\mu^{2/7}} \frac{1}{1 - e_{p,1}} \tag{7.17}$$

$$a_{p,2} = \frac{d_2}{1 + 1.3\mu^{2/7}} \frac{1}{1 + e_{p,2}}; \tag{7.18}$$

- if $e_{p,1} \leq 0.3$ and $e_{p,2} > 0.3$ we apply at the inner planet the equation of Wisdom (6.9) and at the outer one equation (6.10) from Mustill & Wyatt, thus obtaining

$$a_{p,1} = \frac{d_1}{1 - 1.3\mu^{2/7}} \frac{1}{1 - e_{p,1}} \tag{7.19}$$

$$a_{p,2} = \frac{d_2}{1 + 1.8\mu^{1/5} e_{p,2}^{1/5}} \frac{1}{1 + e_{p,2}}; \tag{7.20}$$

- if $e_{p,1} > 0.3$ and $e_{p,2} \leq 0.3$ we have the opposite situation with respect to the one described above, thus we use Mustill & Wyatt for the inner planet and Wisdom for the outer one

$$a_{p,1} = \frac{d_1}{1 - 1.8\mu^{1/5} e_{p,1}^{1/5}} \frac{1}{1 - e_{p,1}}; \tag{7.21}$$

$$a_{p,2} = \frac{d_2}{1 + 1.3\mu^{2/7}} \frac{1}{1 + e_{p,2}}; \tag{7.22}$$

- if $e_{p,1}$ and $e_{p,2}$ are both > 0.3 we use Mustill & Wyatt for the two planets

$$a_{p,1} = \frac{d_1}{1 - 1.8\mu^{1/5} e_{p,1}^{1/5}} \frac{1}{1 - e_{p,1}}; \tag{7.23}$$

$$a_{p,2} = \frac{d_2}{1 + 1.8\mu^{1/5} e_{p,2}^{1/5}} \frac{1}{1 + e_{p,2}}; \tag{7.24}$$

Thus, depending on the values of $e_{p,1}$ and $e_{p,2}$ we substitute in equation (7.3) expressions of $a_{p,1}$ and $a_{p,2}$ as obtained above. The final relation is quite complex and too difficult to solve in an analytical way. Therefore we use again iterative method in order to find, for mass values in the range $[0.1, 13]M_J$, the respective values of eccentricities for the two planets.
We show in figure 7.2 the results of this analysis for a couple of the systems in the sample and in Appendix C are presented all the others. For each system, we obtain a set of suitable points identified by the three coordinates $[e_{p,1}, e_{p,2}, M_p]$ (we recall that the two planets in the system have the same mass). Therefore, we prepare a grid with the two values of eccentricities on the axes and we associate a scale of colors to the mass range. Moreover, in order to determine which planets would have been detected we confront, as always, values of semi-major axis and mass with the detection limits curves and use as criterion of detectability the condition in which at least one of the two planets is above the curve even just in partial zones of its orbit.
In the graphics, we indicate with circles and ellipses planets that are detectable and undetectable respectively. For that systems with no detection limits curves we perform the analysis anyway and plot the entire set of data as circles. From figure 7.2 it is clearly visible how mass (and thus detectability) decreases with incrising eccentricities. Moreover, small variations of $e_{p,1}$ and/or $e_{p,2}$ cause a great damp in mass since, as already mentioned above, the stability depends very little on the mass of the two planets.
We are not able to perform this analysis only on the system HD61005 because it would have needed smaller mass than 0.1 M_J in order to take into account two planets on eccentric orbits as responsible for the gap between the two belts. From this study emerges that the apparent lack of giant planets in the sample of systems analyzed can easily be explained by taking quite eccentric planets of moderate masses that lay beneath detection limits curve. Indeed, large eccentricities are common features of exoplanets and thus we have not to abandon the hypothesis that gaps between two planetesimals belts are dig by the presence of massive objects that surround the central star.

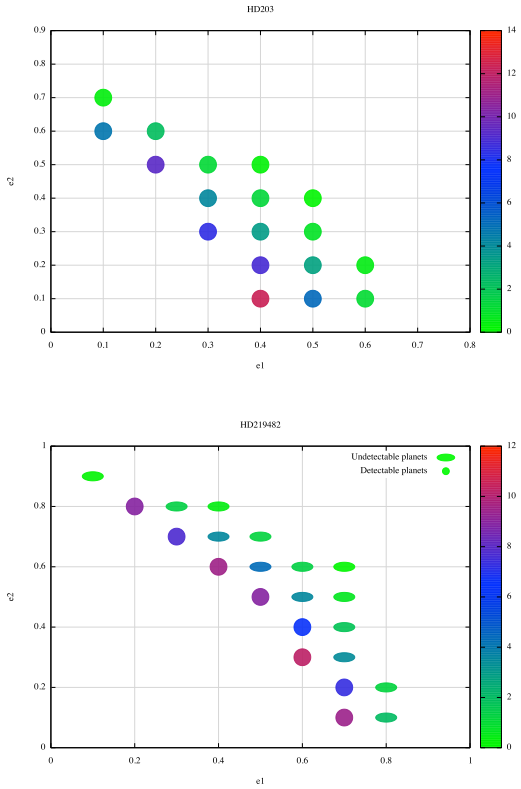

Figure 7.2: Analysis for HD203 and HD219482 with two equal-mass planets on eccentric orbits. On the axes the eccentricity of the inner (e_1) and outer (e_2) planet. The graduation of colors represent values of M_p. For HD203 no detection limits were available thus only the results of the study are shown, whereas for HD219482 detectable planets are represented with circles and undetectable ones with ellipses.

Chapter 8

Radial velocities planets

As a final check, we want to analyze systems with double debris belt in which planets were found using radial velocities technique. In this case we know the mass of the planets with an uncertainty of $\sin i$, its eccentricity, e_p, and semi-major axis, a_p, and we want to investigate at which distance the belt should be due to the presence of the planets. Obviously, as mentioned above, this method is suitable for objects quite near to the star so that only the inner belt will be possibly studied. Then we confront the position of the edges of the inner ring as obtained by the stability theory with the one constrained by SED's fitting.
As a first step, we take from the Chen catalog discussed in chapter 5 the systems with two blackbody temperatures, and thus two belts, and cross them with the Wright catalog (2011). This last is a database of well determined orbital parameters of detected planets (by radial velocities and/or transits methods) and their host stars' properties available on Vizier. It contains 427 planets orbiting 363 stars.
The final sample we obtain is shown in table 8.1 below and comprises 11 planetary systems detected only with radial velocities, some of them with multiple revealed planets. In table 8.1 we list the properties of the planets (mass, semi-major axis, eccentricity and orbital period), the mass of the star and the positions of the two belts as found in C14. From now on we will consider the minimum value of mass for the planets listed in the table (i.e. $\sin i = \pi/2$).
We can have two different situations: the planet could be interior or exterior to the belt and thus potentially affects the inner or outer edge respectively. Moreover, in this sample we have systems with one, two or three planets and we want to apply the analysis shown in chapter 6 and 7.
For systems with just one planet we calculate the extension of the chaotic zone using equations (6.8) and (6.9) for eccentricities ≤ 0.3 and equations (6.10) and (6.11) for $e_p > 0.3$. Then we sum $(\Delta a)_{in}$ and $(\Delta a)_{ex}$ to the periastron and apoastron of the planet respectively in order to constrain the width of the chaotic region and, thus, the edge of the belt.
In three of the seven systems, HD1461, HD10647 and HD168746, the planet is too far from the belt to be responsible for its position and therefore we expect the presence of more planets external to the one detected.
HD52265 and 70 Virgo have a planet interior to the belt and indeed, in both

$Name$	$M_p \sin i/M_J$	a_p(AU)	e_p	T(days)	$M_*/M_\odot$	d_1(AU)	d_2(AU)
HD1461 b	0.02	0.06	0.14	5.77	1	0.6	154.9
HD10647 b	0.93	2.02	0.16	1003	1.1	24	385.3
HD33636 b	9.27	3.27	0.48	2127.7	1.1	0.7	199.6
HD50554 b	4.4	2.26	0.44	1224	1.1	1.1	169.1
HD52265 b	1.07	0.5	0.33	119.29	1.2	0.7	146.8
HD82943 b	1.73	1.18	0.22	441.2	1.1	0.01	165
HD82943 c	1.99	0.74	0.36	219.5	1.1	0.01	165
61 Virgo b	0.02	0.05	0.12	4.22	1	9.2	149
61 Virgo c	0.03	0.22	0.14	38.02	1	9.2	149
61 Virgo d	0.07	0.47	0.35	123.01	1	9.2	149
70 Virgo b	7.46	0.48	0.4	116.69	1.1	0.8	292.5
HD128311 b	1.46	1.09	0.35	454.2	0.8	1.3	1211
HD128311 c	3.25	1.75	0.23	923.8	0.8	1.3	1211
HD168746 b	0.25	0.07	0.11	6.4	0.9	0.9	432.3
HD202206 b	16.82	0.81	0.44	255.87	1	2.9	131.8
HD202206 c	2.33	2.49	0.27	1383.4	1	2.9	131.8

Table 8.1: Planets and systems parameters

cases, it seems to be the direct responsible for the inner edge of the ring as we can see calculating the chaotic zones for the two exoplanets that extend to 1.03 AU for 70 Virgo ($d_1 = 0.8$ AU) and to 0.9 AU for HD52265 ($d_1 = 0.7$ AU). Even if the position of the belt in the two systems is a little bit nearer to the star in both cases (explainable by Poynting-Robertson effects), they confirm quite well our assumptions.

The two left systems, instead, own a planet that is placed beyond the inner ring and thus it would possibly affect its outer edge. Indeed, doing the stability analysis we find that the chaotic zone for HD33636 extends to 0.97 AU ($d_1 = 0.7$AU) and for HD50554 to 0.81 AU ($d_1 = 1.1$AU) and thus both systems confirm with accuracy the position of the belt as report in C10.

We then have three systems with two planets each, HD82943, HD128311 and HD202206. The kind of analysis suitable in this case is the one presented in chapter 7: the stability of the zone between the two massive objects is regulated by the Hill criterion of equation (7.1), while the chaotic regions inside the orbit of the inner planet and outside that of the external one are, as always, determined by Wisdom or Mustill & Wyatt.

HD82943 has both planets external to the belt so that only the inner one could be responsible for the outer edge. Its chaotic zone extends down to 0.33 AU and from table 8.1 we get $d_1 = 0.01$AU. Therefore we conclude once more that the two positions are in good agreement, taking into account P-R drag that causes dust particles to fall into nearer orbit around the star. Another interesting feature of this system is that the apoastron of the inner planet at 1 AU is placed further out than the periastron of the second at 0.92 AU, so that their orbits cross each other. Thus, the only way to have a stable system is the configuration in which the two planets are in resonance one with the other, precisely a $2:1$ resonance.

HD128311 and HD202206 are of great interest since the belt is placed between

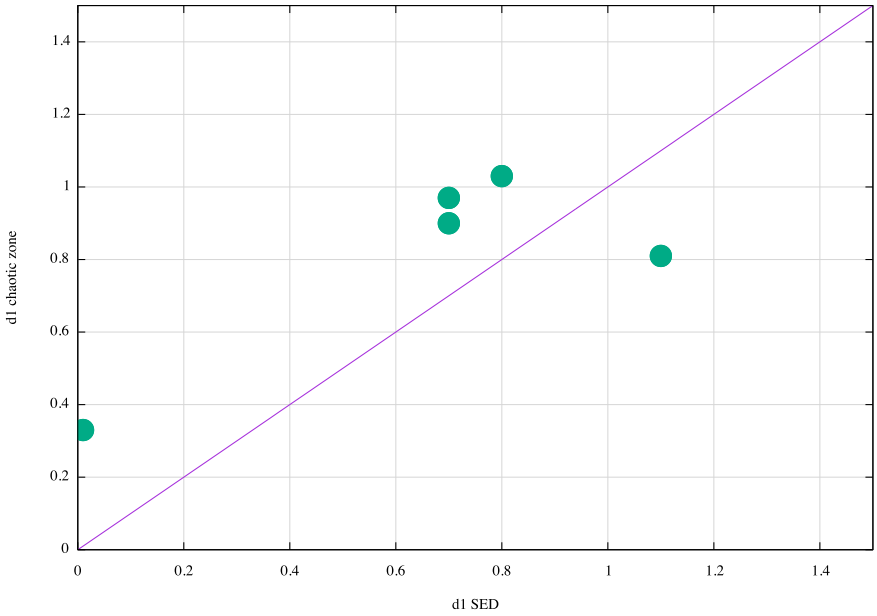

Figure 8.1: Positions of the internal belt for different systems as obtained by SED's fitting and by equations for the chaotic zone interior and exterior to the planet. The purple line represents points for which the two positions coincide.

the two planets. However, using the Hill criterion we find that the zone in the middle is completely unstable and no particle would survive in it. For HD202206 the chaotic zone extends from 0.23 AU to 3.88 AU and the belt should be at 2.9 AU. The only explanation seems to be that the SED's fitting is affected by an uncertainty of some AU. For HD128311, however, we can give another kind of justification: as in the case of HD82943, the orbits of the two planets cross each other and then the system in order to be stable should be locked in a $4:1$ or $5:1$ mean motion resonance. This last could be the responsible for a tiny stable region at ~ 1.3 AU in which dust particles would survive.
The last system is 61 Virgo and it owns three planets. Unfortunately, as mentioned above, the only case that we are able to treat is the one with equal- mass planets on circular orbits. Since for 61 Virgo this is not the case we can not tell much on its stability and further studies are needed.
We show in figure 8.1 the position of the inner belt as given by SED fitting and as obtained by means of equations for the width of the chaotic zone for HD52265, 70 Virgo, HD33636, HD50554 and HD82943 that are the only systems with planets able to constraint the position d_1 (for what regards HD128311 and HD202206 we can only infer if the belt could be placed between the two planets but we can not estimate its position using the stability analysis).
The conclusions that we get from this graphic and, more in general, from this chapter are quite rewarding since in most cases they confirm our expectations on the position of the inner belt. Therefore, we conclude that SED's fitting give quite precise results on the distances of the belts (at least the inner ones) and that the analysis of chapter 6 and 7 on single and double planetary systems are

reliable.

Chapter 9

Conclusions

In this work we studied systems that own two debris belts and a gap between them. The main assumption was that one or more planets were the responsible for the lack of particles in this area of the system, as observed in the case of Solar System. We compared the planets masses and separations for objects within the two belts as derived for the various models (one, two and three planets) with the detection limits of 40 systems observed as part of the SPHERE GTO survey. With the exception of HD218396 (HR8799) and HD95086, no planet has yet been revealed in such zones among the systems of our ensemble. Thus, we have two possibilities: the planets have masses or orbital parameters that make them invisible to actual instruments or some other phenomenon lies beneath the gap among which the most accredited is self-stirring due to the largest planetesimals.
We first investigated the presence of one single planet on circular orbit but for the systems in the sample, with the exception of HD61005, there was no result for masses up to 21 M_J.
We thus move to one planet on eccentric orbit obtaining the first theoretical formulation for such a situation. From our simulations emerged that previous equations, as the one of Wisdom or Mustill & Wyatt for the chaotic zone of a planet on circular orbit, were suitable also for the eccentric case with the substitution of the semi-major axis of the planet a_p with its positions at periastron and apoastron. With growing eccentricities, the mass of the planet decreases slightly but, however, extreme situations are needed. In fact, in order to have undetectable planets with masses beneath detection limits curves we predict unlikely values of e_p, greater than 0.7 in most systems. Thus, even if the hypothesis of one planet could be suitable in some cases, we conclude that it is most unlikely in the great part of the systems analyzed.
The second part of the work investigated the presence of two or three planets in the gap between the belts. The first model assumes two equal-mass planets on circular orbits. In most cases the masses deduce from this kind of analysis were too big, not only with respect to detection limits so that they would have been already revealed, but even to be properly a planet (they reach stars' masses).
However, the left two models were quite promising. Indeed, for the three equal-mass circular-orbit planetary model the great part of the systems showed results under detection limits curves and thus in agreement with the actual observations. Instead, considering two equal-mass planets on eccentric orbits demon-

strated that little variations in the eccentricities of one or both massive objects cause a steep collapse in the mass of the planets hiding them from possible detections.
Therefore, we conclude our work noticing that, even if very few objects have been detecting, we can not abandon the starting hypothesis that in systems with double debris belt the gap between the two is due to the presence of exoplanets. Indeed, adding more planets or considering higher eccentricities does the job. Both conditions are likely to be realized since many detected exoplanets move on highly eccentric orbits and multi-planetary systems, beyond the Solar one, have been discovered as for example HR8799 that own four giant planets between the two belts.
In order to have a further confirmation of the approximations used in chapter 6 and 7, beyond the numerical simulations, we analyzed systems with known radial velocities planets and double debris belt. Using the equations for the chaotic zone of the planet we constrained (for some of the RV systems in the sample) the position of the internal ring and compare it with d_1 presented in the C14 as obtained by SED fitting. The two positions were in very good agreement, thus confirming the reliability of the previous analysis.
We finally note that the SED's analysis of dust temperatures and models of belts' locations could be affected by uncertainties that cause, as a result, wrong placement of the birth rings, especially for what regards components placed beyond 50 AU (see chapter 5). In fact, we get quite different informations on the belts from system in which the debris disk has been spatially resolved, particularly on the Kuiper-like belts, whereas the inner asteroid-like rings seem to be best constrained as mentioned above. However, it is not very clear which technique between SED's fitting and direct imaging is the best one to constrain the position of the edges since also direct imaging could have systematic biases linked to the angular differential imaging technique. Then we conclude that our analysis for the stability of the systems is quite reliable even for unresolved ones, at least for $d_2 \leq 50$ AU.
We applied the method described in chapter 6 and 7 to the recently resolved system HIP67497 and we presented our results in the paper of Bonnefoy et al. (2016), submitted for the second time to *Astronomy and Astrophysics*. We show such analysis in appendix D.

Appendix A

Detection limits

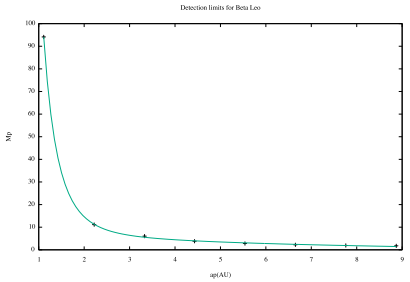

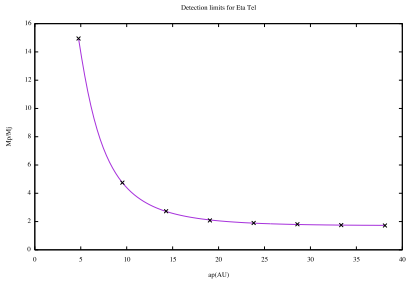

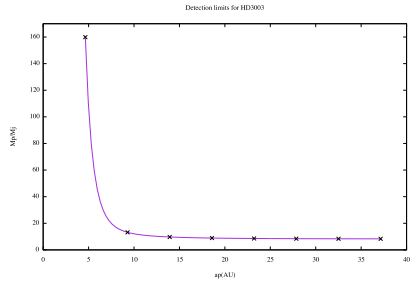

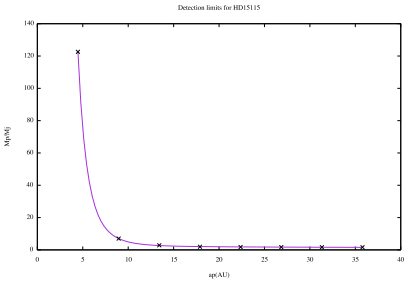

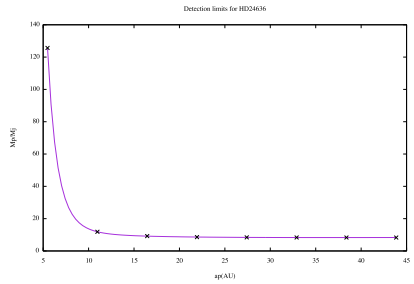

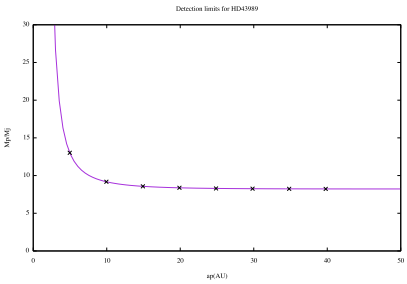

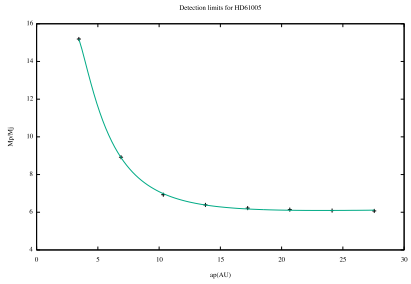
Detection limits for HD61005
Mp(Mj)
ap(AU)

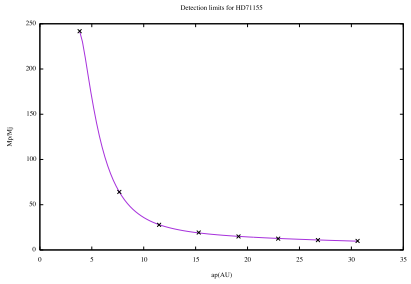
Detection limits for HD71155
Mp(Mj)
ap(AU)

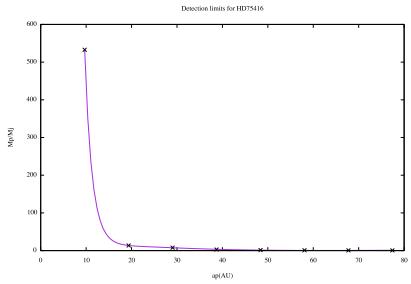
Detection limits for HD75416
Mp(Mj)
ap(AU)

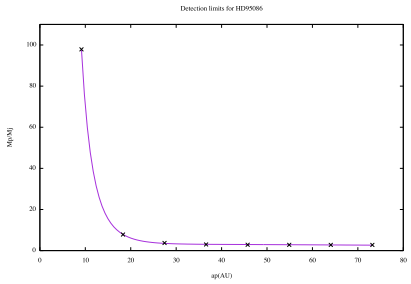
Detection limits for HD95086
Mp(Mj)
ap(AU)

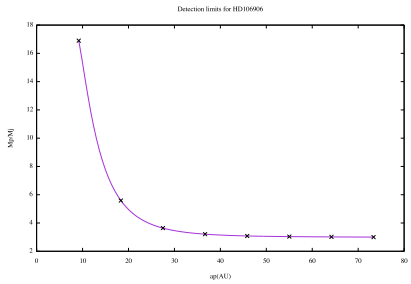
Detection limits for HD106906
Mp(Mj)
ap(AU)

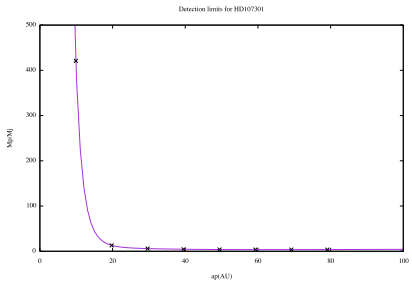
Detection limits for HD107301
Mp(Mj)
ap(AU)

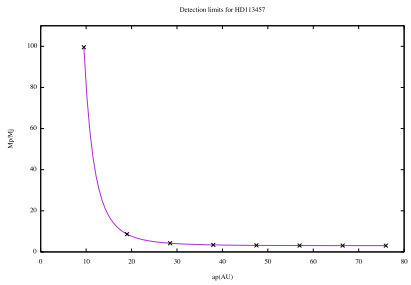
Detection limits for HD113457
Mp(Mj)
ap(AU)

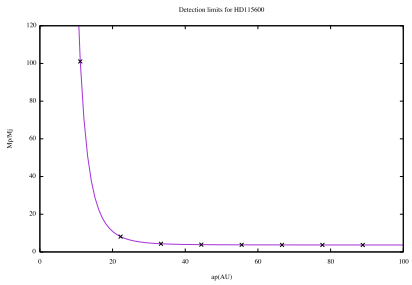
Detection limits for HD115600
Mp(Mj)
ap(AU)

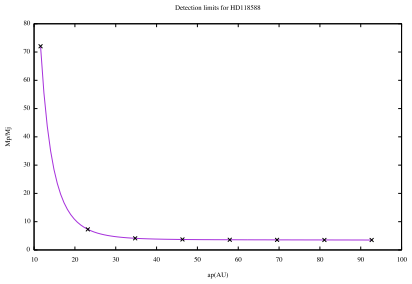
Detection limits for HD118588
Mp(Mj)
ap(AU)

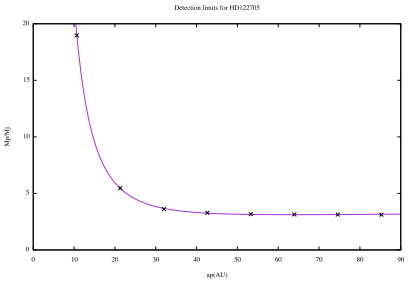
Detection limits for HD122705
Mp(Mj)
ap(AU)

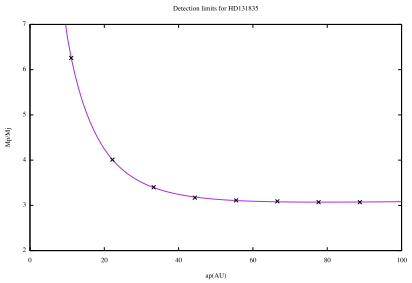
Detection limits for HD131835
Mp(Mj)
ap(AU)

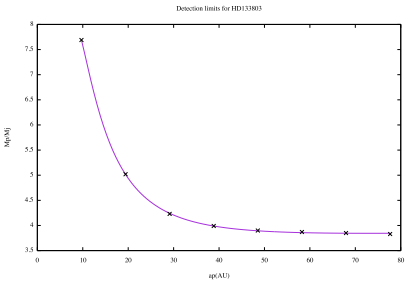
Detection limits for HD133803
Mp(Mj)
ap(AU)

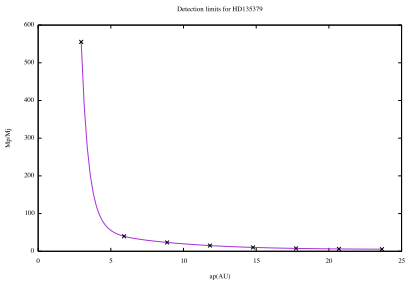
Detection limits for HD135379
Mp(Mj)
ap(AU)

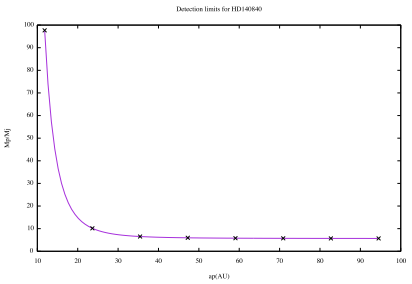
Detection limits for HD140840
Mp(Mj)
ap(AU)

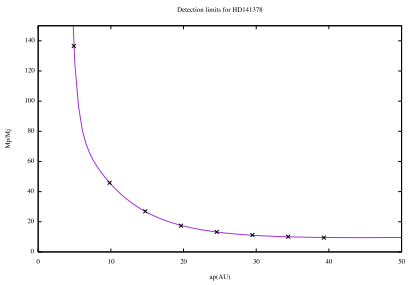
Detection limits for HD141378
Mp(Mj)
ap(AU)

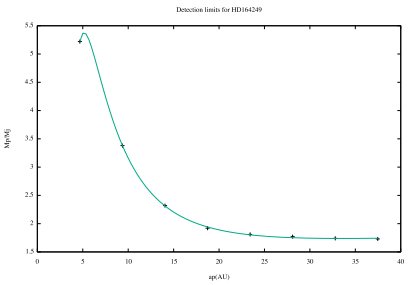
Detection limits for HD164249
Mp(Mj)
ap(AU)

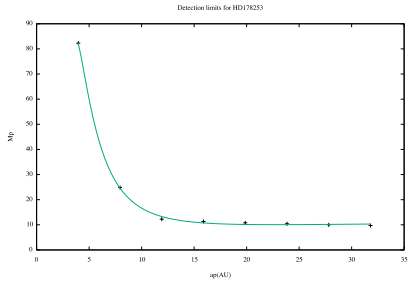
Detection limits for HD178253
Mp
ap(AU)

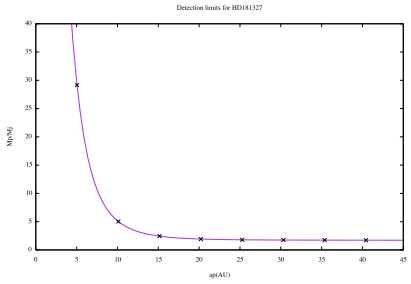
Detection limits for HD181327
Mp/Mj
ap(AU)

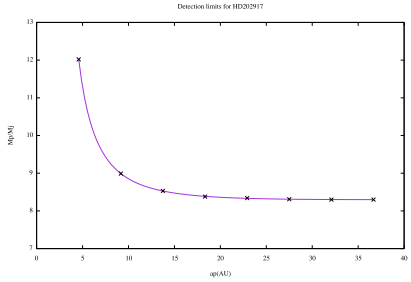
Detection limits for HD202917
Mp/Mj
ap(AU)

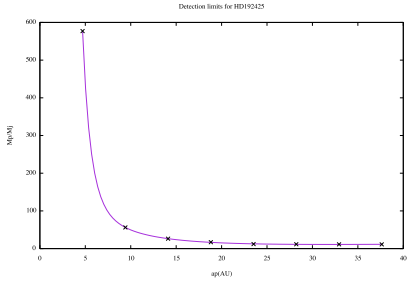
Detection limits for HD192425
Mp/Mj
ap(AU)

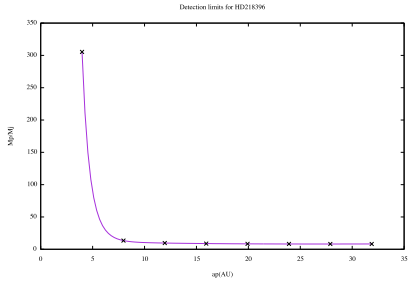
Detection limits for HD218396
Mp/Mj
ap(AU)

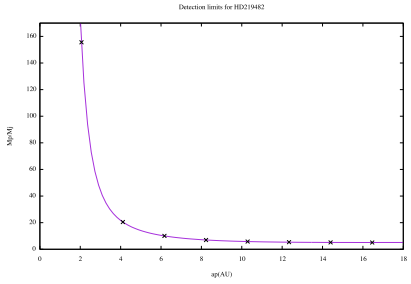
Detection limits for HD219482
Mp/Mj
ap(AU)

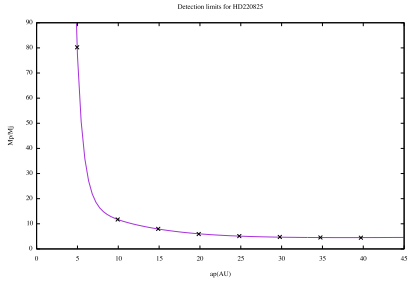
Detection limits for HD220825
Mp/Mj
ap(AU)

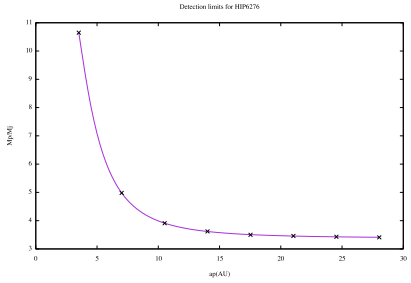
Detection limits for HIP96276
Mp/Mj
ap(AU)

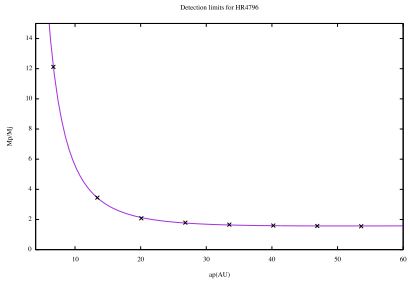
Detection limits for HR4796
M(jvN)
ap(AU)
0
2
4
6
8
10
12
14
10
20
30
40
50
60

Appendix B

Single planet

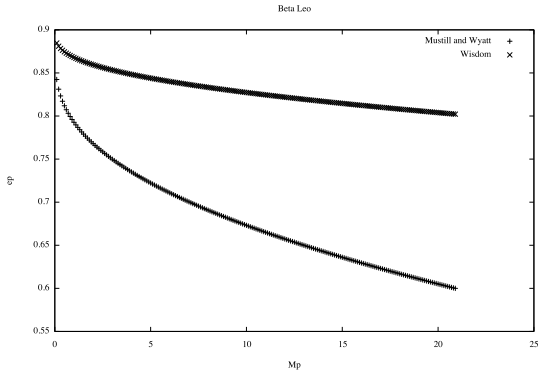

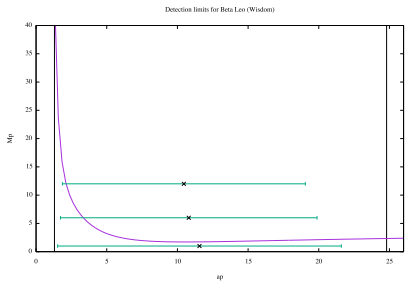

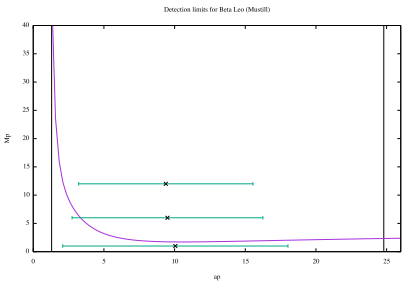

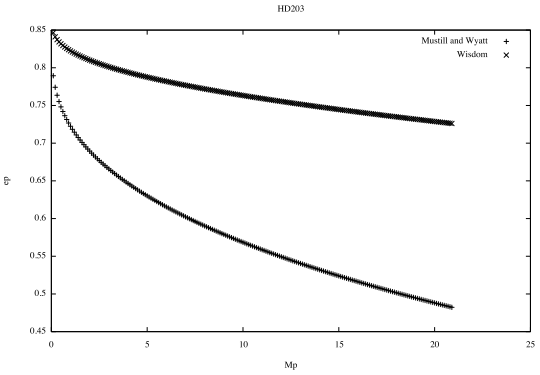
HD203
Mustill and Wyatt
Wisdom
ep
Mp

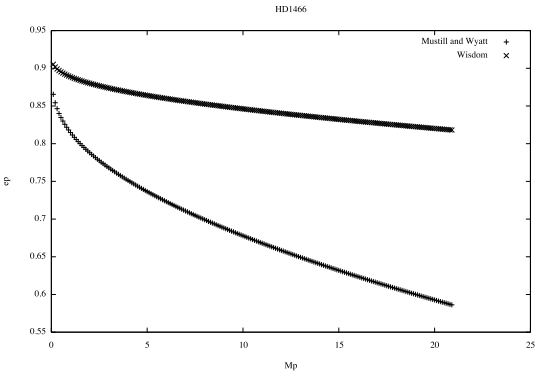
HD1466
Mustill and Wyatt
Wisdom
ep
Mp

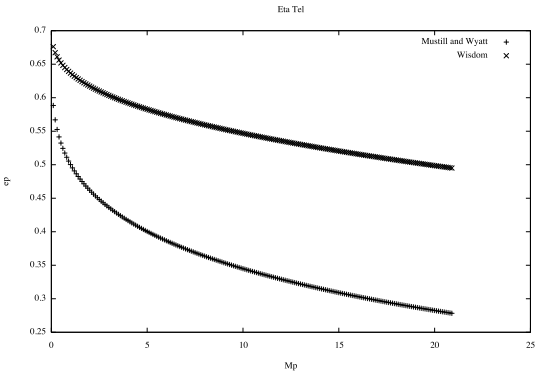
Eta Tel
Mustill and Wyatt
Wisdom
ep
Mp

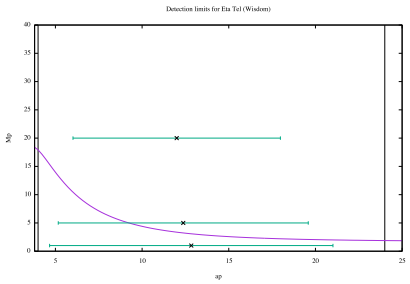
Detection limits for Eta Tel (Wisdom)
Mp
ap

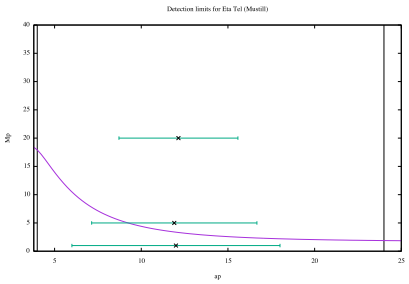
Detection limits for Eta Tel (Mustill)
Mp
ap

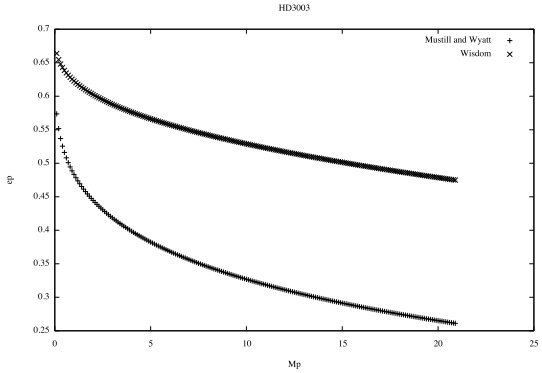
HD3003
Mustill and Wyatt
Wisdom
ep
Mp

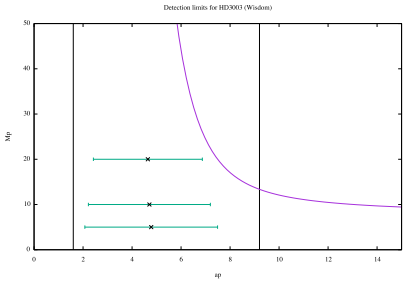
Detection limits for HD3003 (Wisdom)
Mp
ep

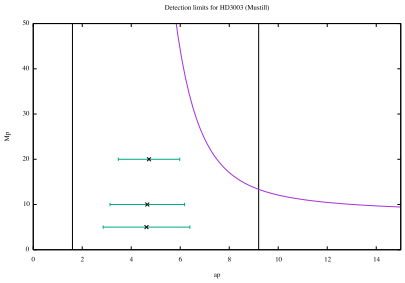
Detection limits for HD3003 (Mustill)
Mp
ep

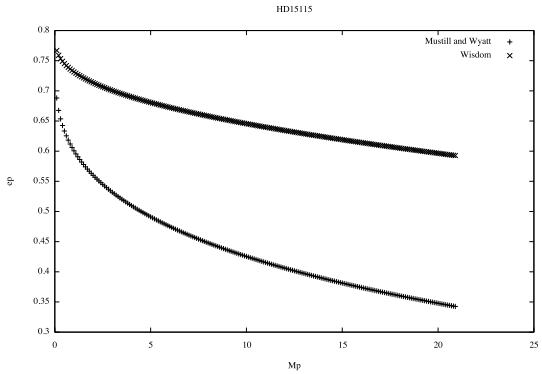
HD15115
Mustill and Wyatt
Wisdom
ep
Mp

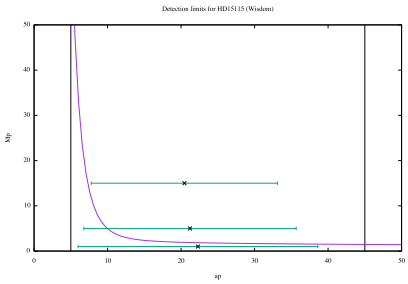
Detection limits for HD15115 (Wisdom)
Mp
ep

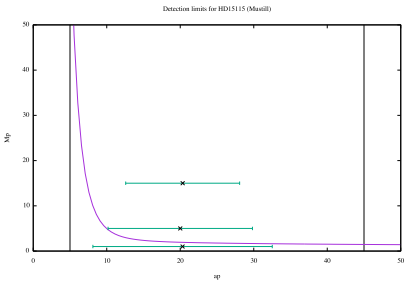
Detection limits for HD15115 (Mustill)
Mp
ep

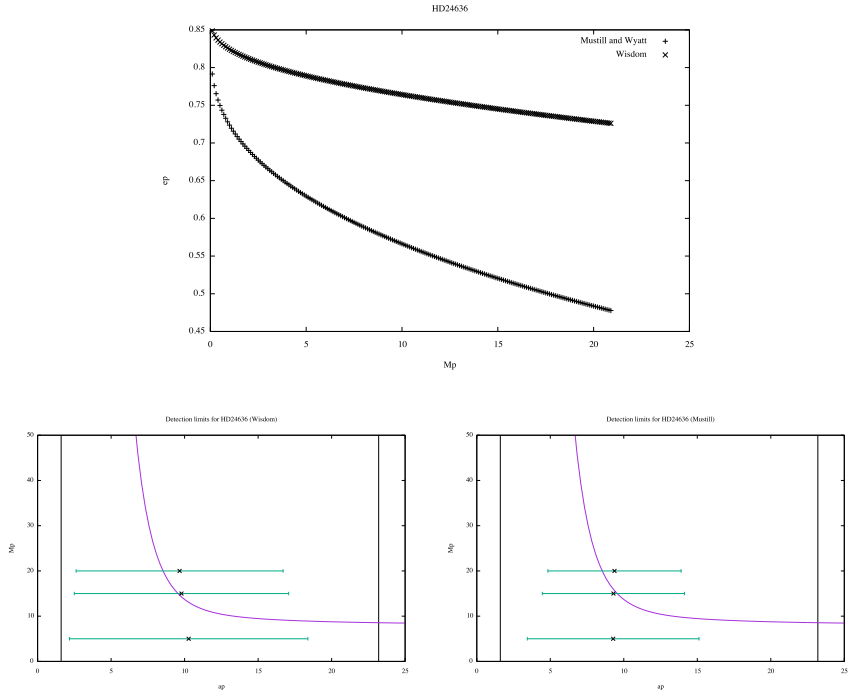
HD24636
Mustill and Wyatt
Wisdom
ep
Mp
Detection limits for HD24636 (Wisdom)
Mp
ap
Detection limits for HD24636 (Mustill)
Mp
ap

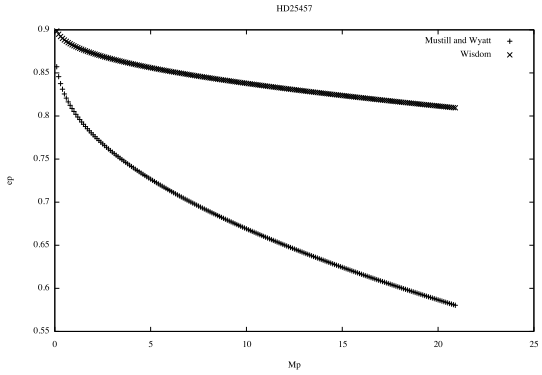
HD25457
Mustill and Wyatt
Wisdom
ep
Mp
0.9
0.85
0.8
0.75
0.7
0.65
0.6
0.55
0
5
10
15
20
25

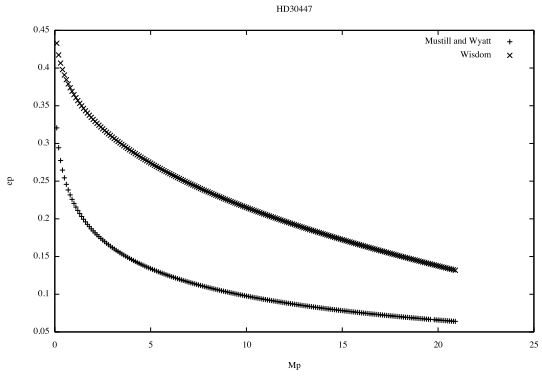
HD30447
Mustill and Wyatt
Wisdom
ep
Mp
0.45
0.4
0.35
0.3
0.25
0.2
0.15
0.1
0.05
0
5
10
15
20
25

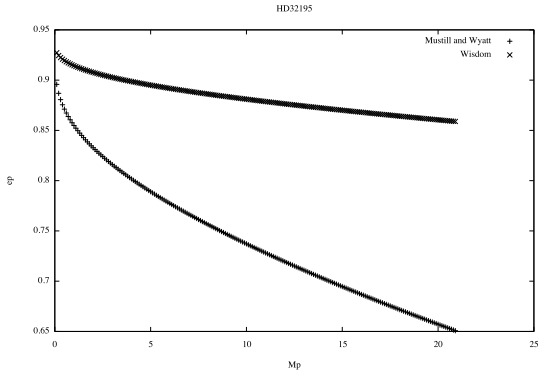
HD32195
Mustill and Wyatt
Wisdom
ep
Mp
0.95
0.9
0.85
0.8
0.75
0.7
0.65
0
5
10
15
20
25

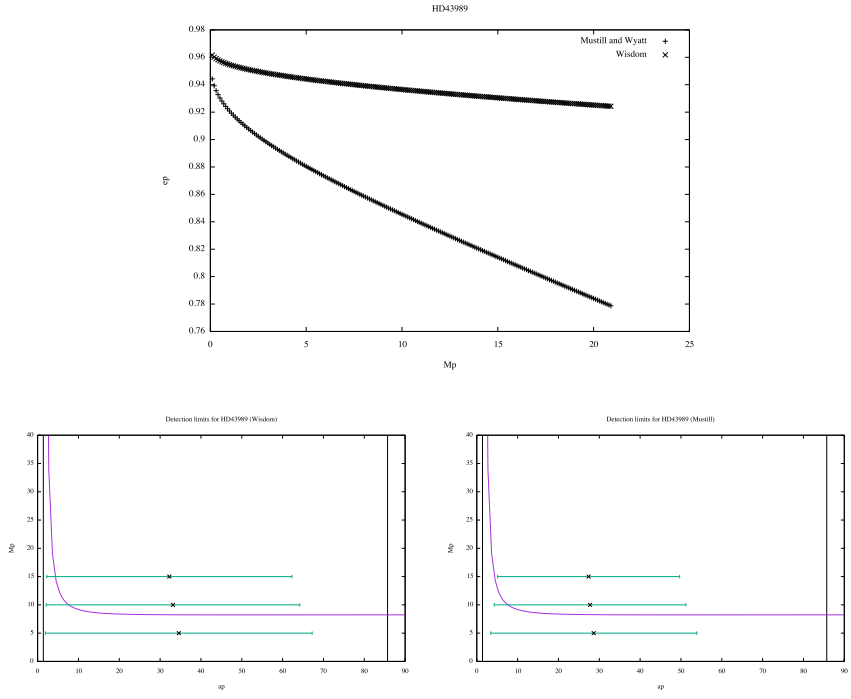
HD43989
Mustill and Wyatt
Wisdom
ep
Mp
Detection limits for HD43989 (Wisdom)
Mp
ap
Detection limits for HD43989 (Mustill)
Mp
ap

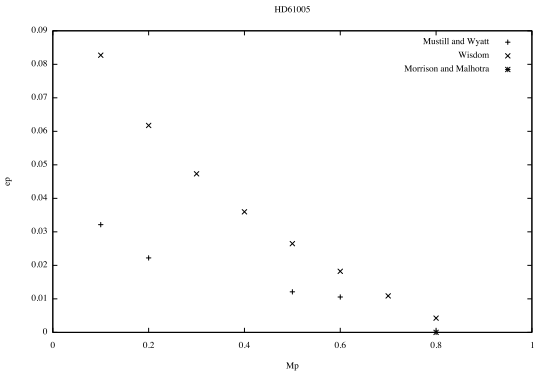
HD61005
Mustill and Wyatt
Wisdom
Morrison and Malhotra
ep
Mp

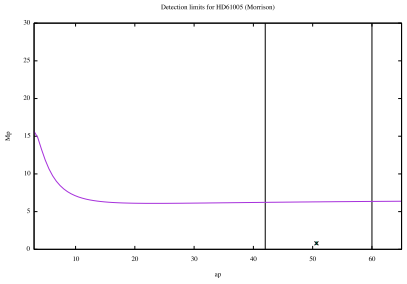
Detection limits for HD61005 (Morrison)
Mp
ap

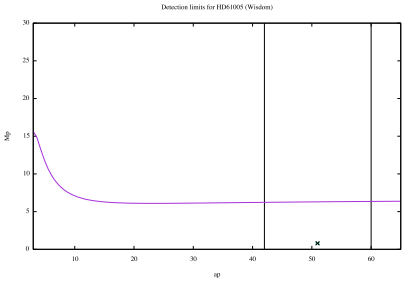
Detection limits for HD61005 (Wisdom)
Mp
ap

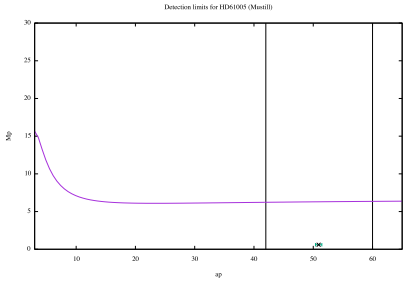
Detection limits for HD61005 (Mustill)
Mp
ap

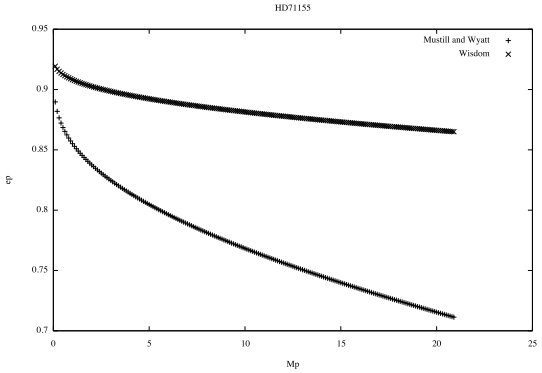
HD71155
Mustill and Wyatt
Wisdom
ep
Mp

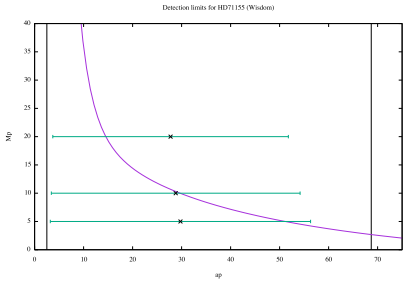
Detection limits for HD71155 (Wisdom)
Mp
ap

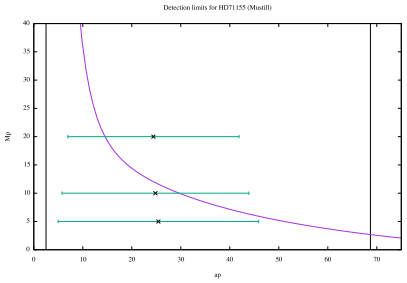
Detection limits for HD71155 (Mustill)
Mp
ap

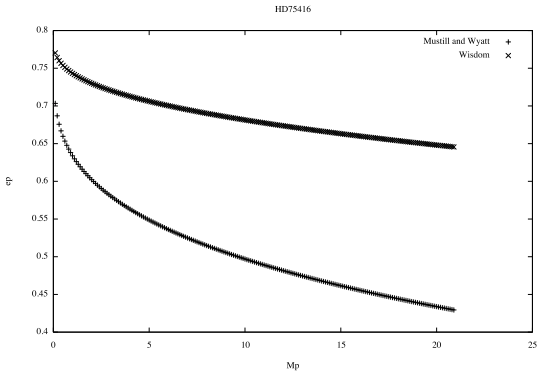
HD75416
Mustill and Wyatt
Wisdom
ep
Mp

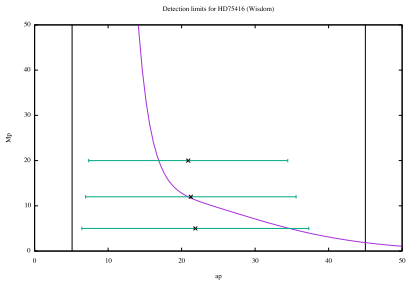
Detection limits for HD75416 (Wisdom)
Mp
ap

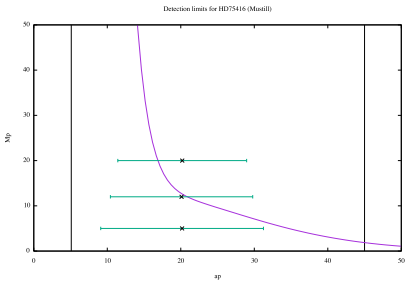
Detection limits for HD75416 (Mustill)
Mp
ap

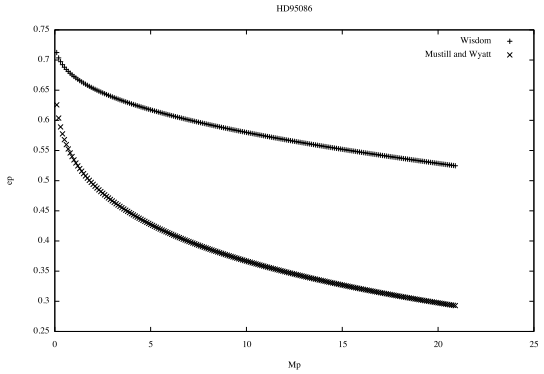
HD95086
Wisdom
Mustill and Wyatt
ap
Mp

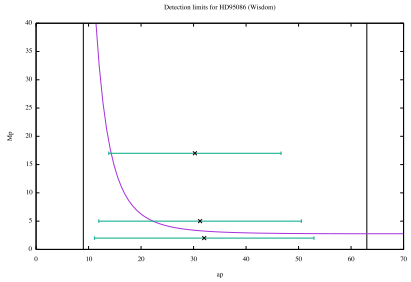
Detection limits for HD95086 (Wisdom)
Mp
ap

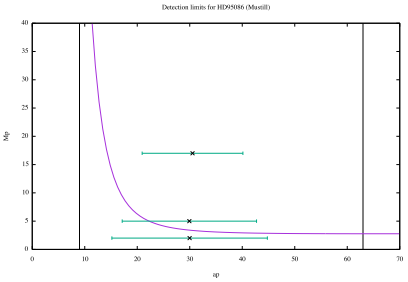
Detection limits for HD95086 (Mustill)
Mp
ap

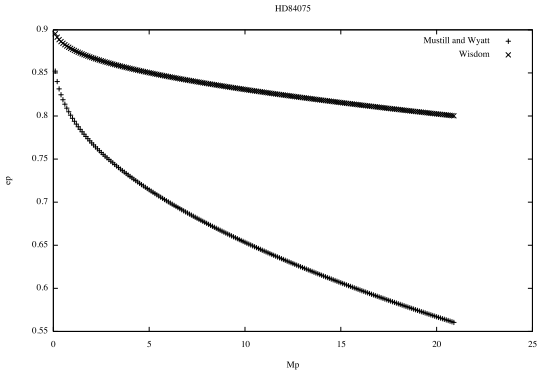
HD84075
Mustill and Wyatt
Wisdom
ep
Mp
0.9
0.85
0.8
0.75
0.7
0.65
0.6
0.55
0
5
10
15
20
25

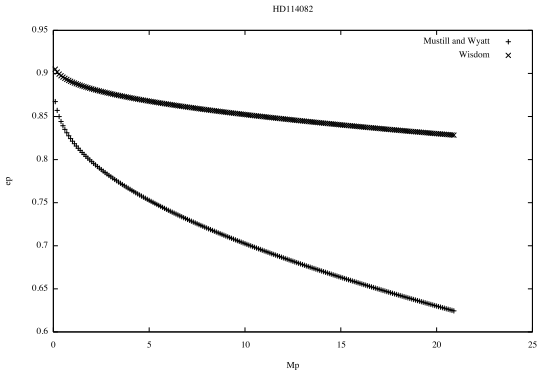
HD114082
Mustill and Wyatt
Wisdom
ep
Mp
0.95
0.9
0.85
0.8
0.75
0.7
0.65
0.6
0
5
10
15
20
25

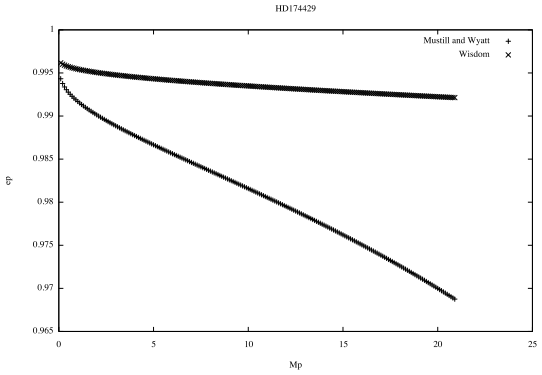
HD174429
Mustill and Wyatt
Wisdom
ep
Mp
1
0.995
0.99
0.985
0.98
0.975
0.97
0.965
0
5
10
15
20
25

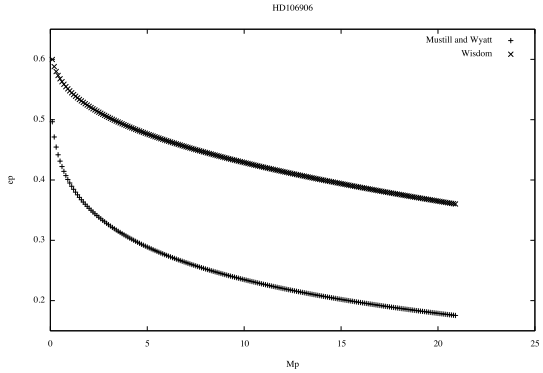
HD106906
Mustill and Wyatt
Wisdom
ep
Mp

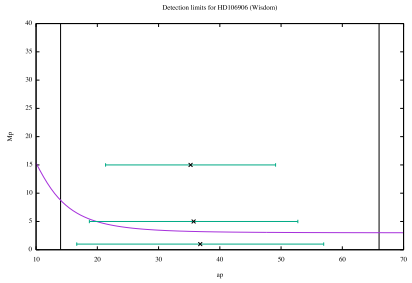
Detection limits for HD106906 (Wisdom)
Mp
ap

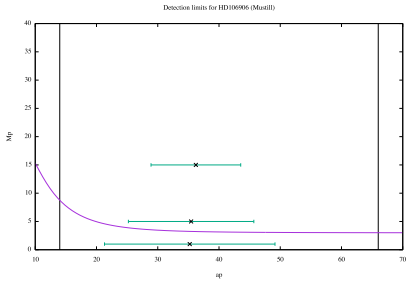
Detection limits for HD106906 (Mustill)
Mp
ap

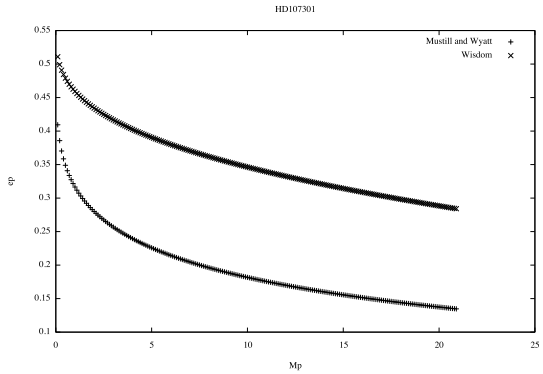
HD107301
Mustill and Wyatt
Wisdom
ep
Mp

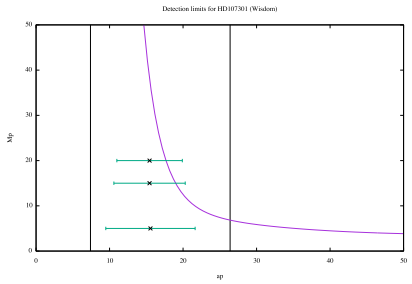
Detection limits for HD107301 (Wisdom)
Mp
ap

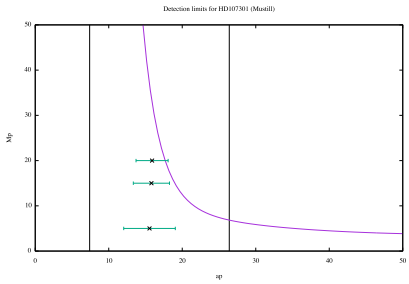
Detection limits for HD107301 (Mustill)
Mp
ap

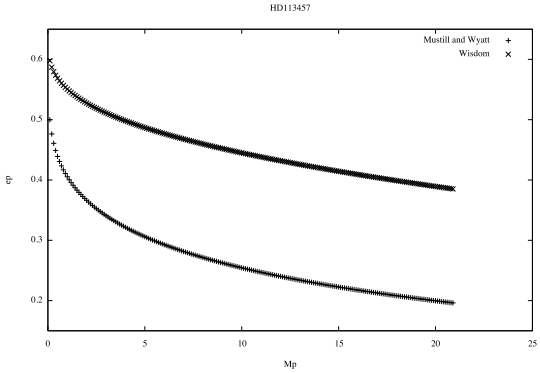
HD113457
Mustill and Wyatt
Wisdom
ep
Mp

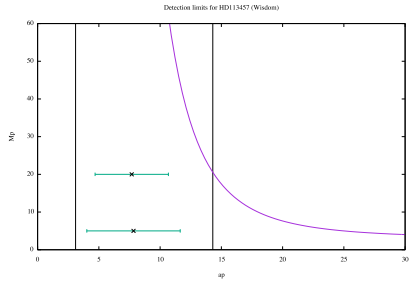
Detection limits for HD113457 (Wisdom)
Mp
ap

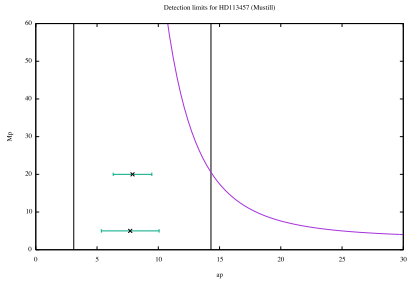
Detection limits for HD113457 (Mustill)
Mp
ap

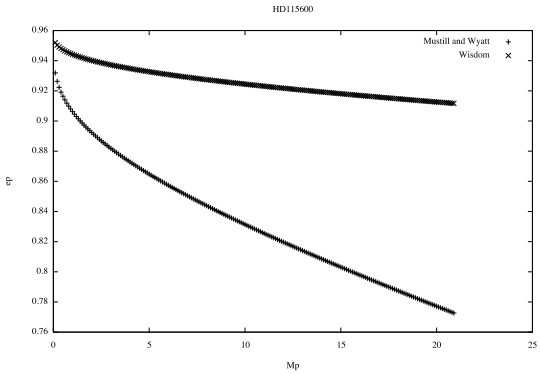
HD115600
Mustill and Wyatt
Wisdom
ep
Mp

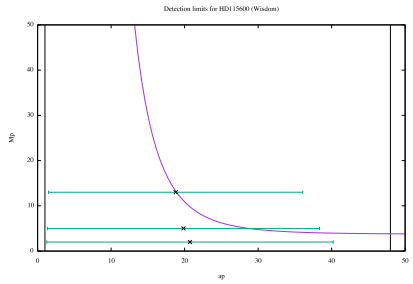
Detection limits for HD115600 (Wisdom)
Mp
ap

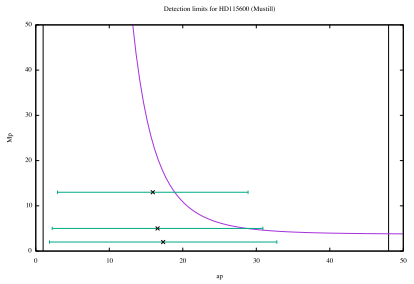
Detection limits for HD115600 (Mustill)
Mp
ap

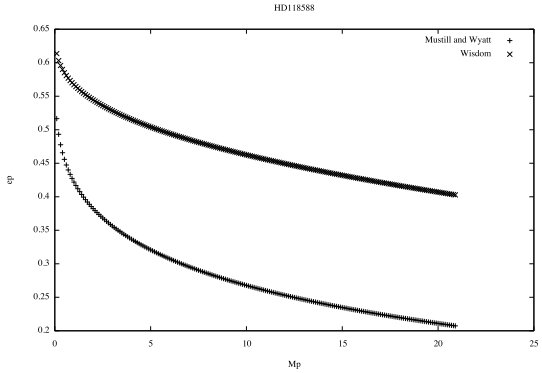
HD118588
Mustill and Wyatt
Wisdom
ep
Mp

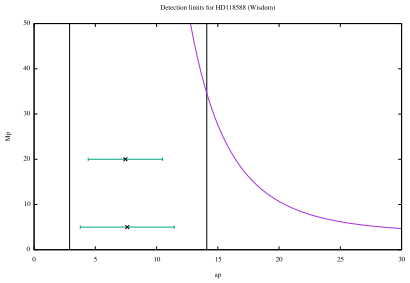
Detection limits for HD118588 (Wisdom)
Mp
ap

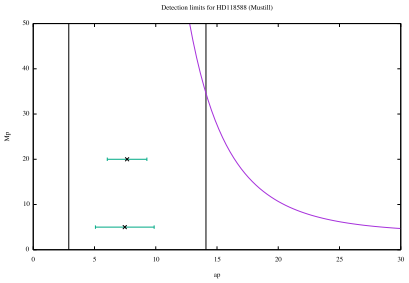
Detection limits for HD118588 (Mustill)
Mp
ap

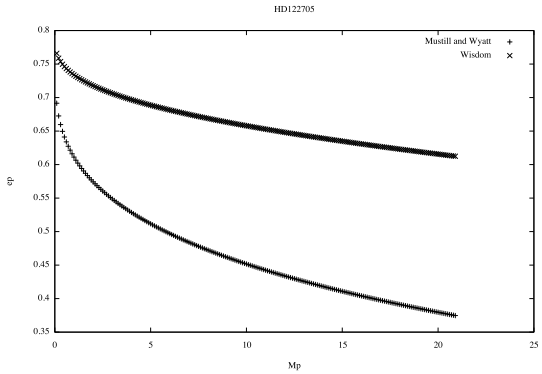
HD122705
Mustill and Wyatt
Wisdom
ep
Mp

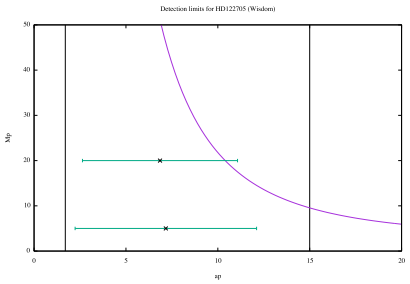
Detection limits for HD122705 (Wisdom)
Mp
ap

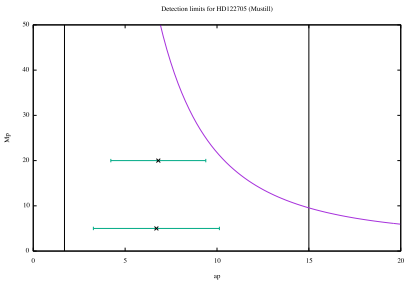
Detection limits for HD122705 (Mustill)
Mp
ap

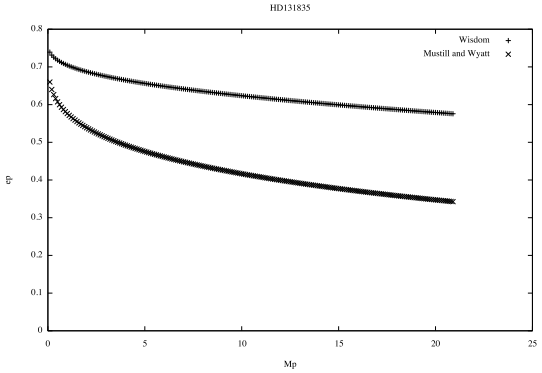
HD131835
Wisdom
Mustill and Wyatt
ep
Mp

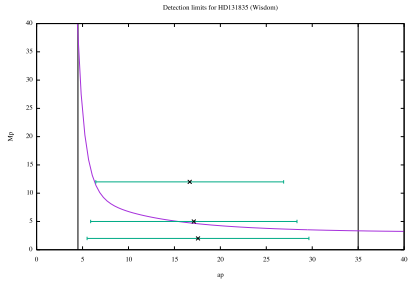
Detection limits for HD131835 (Wisdom)
Mp
ap

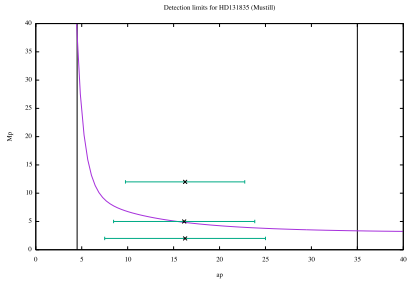
Detection limits for HD131835 (Mustill)
Mp
ap

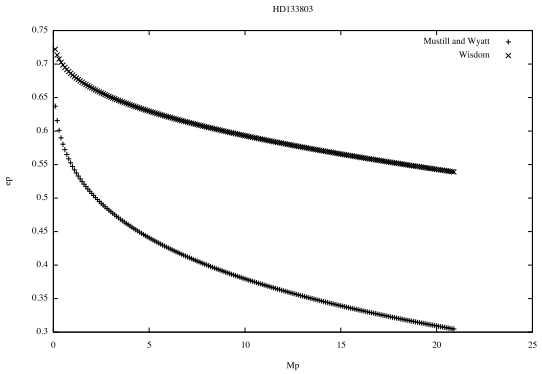
HD133803
Mustill and Wyatt
Wisdom
ep
Mp

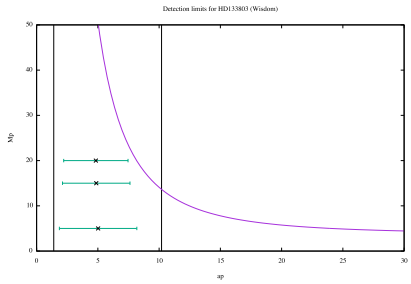
Detection limits for HD133803 (Wisdom)
Mp
ap

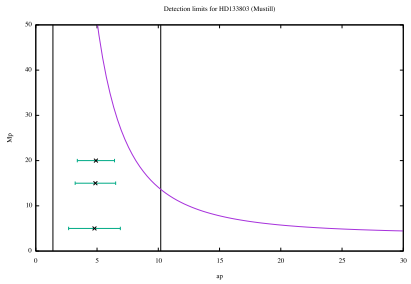
Detection limits for HD133803 (Mustill)
Mp
ap

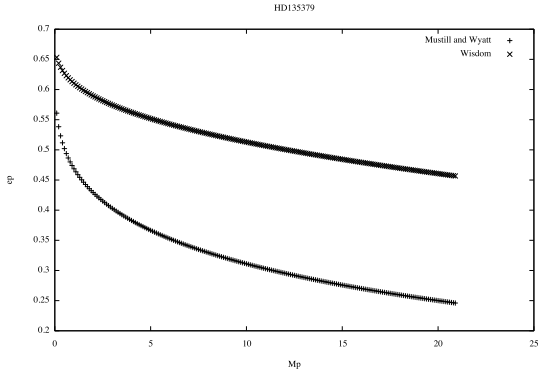
HD135379
Mustill and Wyatt
Wisdom
ep
Mp

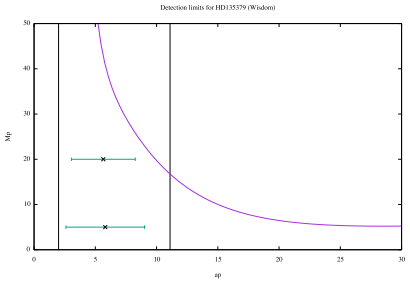
Detection limits for HD135379 (Wisdom)
Mp
ap

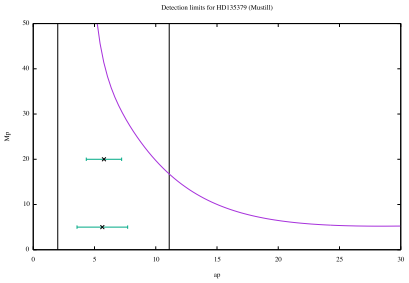
Detection limits for HD135379 (Mustill)
Mp
ap

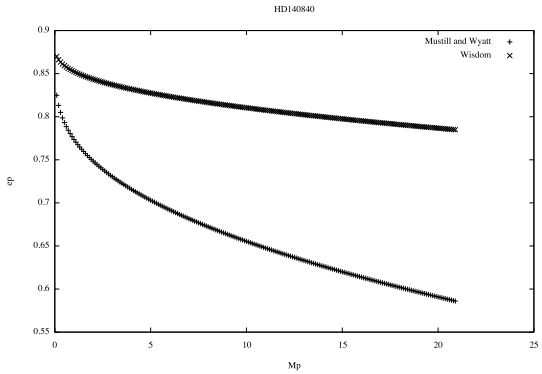
HD140840
Mustill and Wyatt
Wisdom
ep
Mp

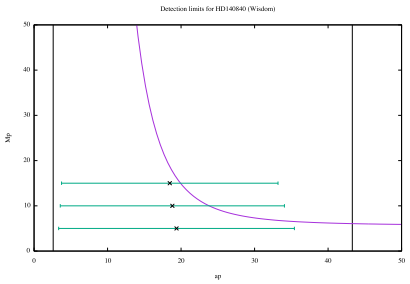
Detection limits for HD140840 (Wisdom)
Mp
ap

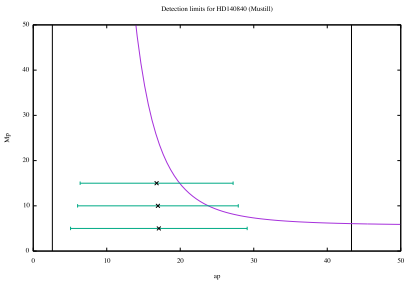
Detection limits for HD140840 (Mustill)
Mp
ap

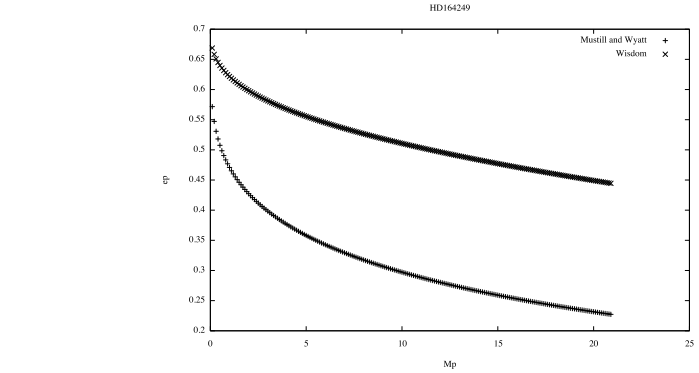
HD164249
Mustill and Wyatt
Wisdom
ep
Mp

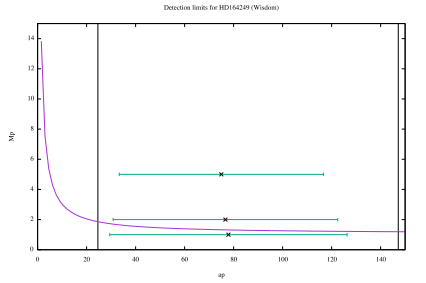
Detection limits for HD164249 (Wisdom)
Mp
ap

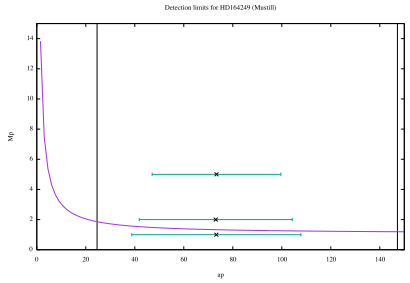
Detection limits for HD164249 (Mustill)
Mp
ap

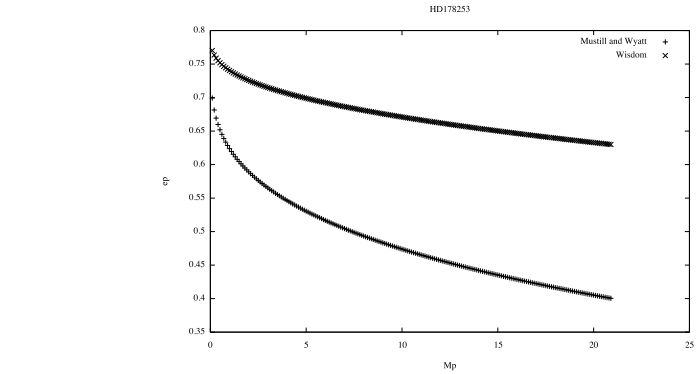
HD178253
Mustill and Wyatt
Wisdom
ep
Mp

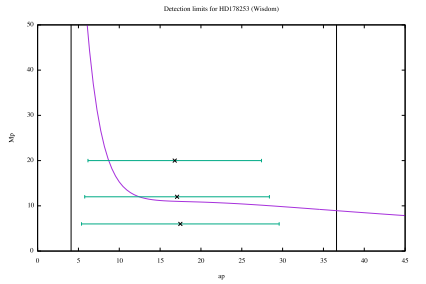
Detection limits for HD178253 (Wisdom)
Mp
ap

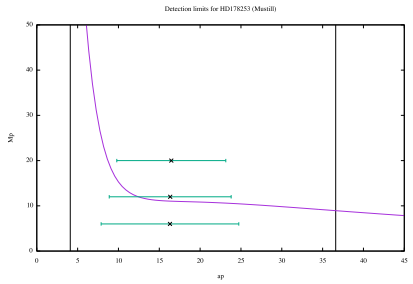
Detection limits for HD178253 (Mustill)
Mp
ap

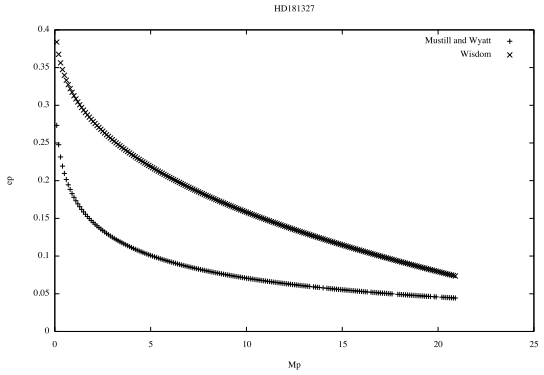
HD181327
Mustill and Wyatt
Wisdom
ep
Mp

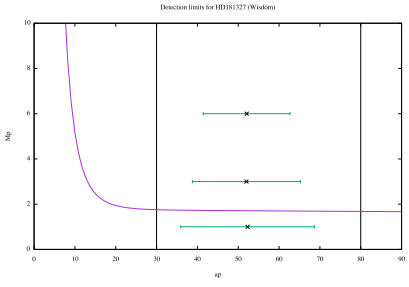
Detection limits for HD181327 (Wisdom)
Mp
ap

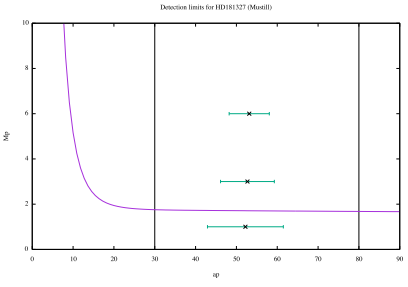
Detection limits for HD181327 (Mustill)
Mp
ap

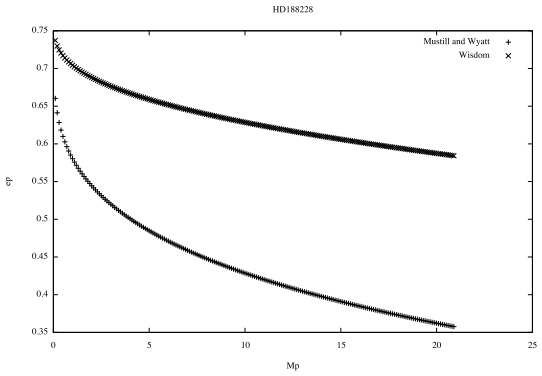
HD188228
Mustill and Wyatt
Wisdom
ep
Mp

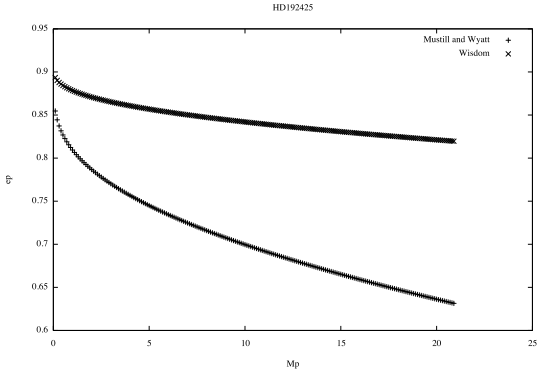
HD192425
Mustill and Wyatt
Wisdom
ep
Mp

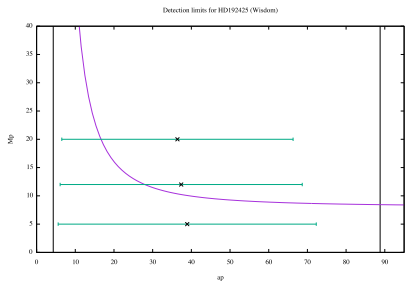
Detection limits for HD192425 (Wisdom)
Mp
ap

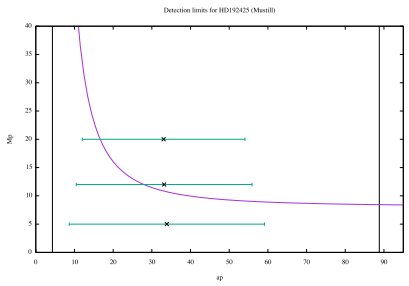
Detection limits for HD192425 (Mustill)
Mp
ap

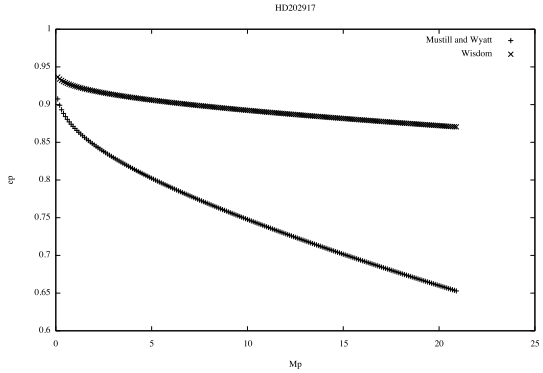
HD202917
Mustill and Wyatt
Wisdom
ep
Mp

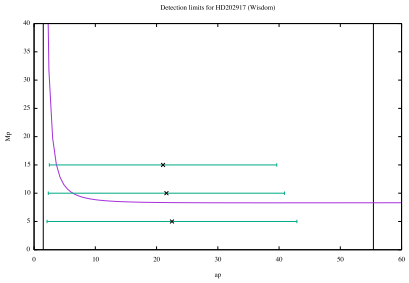
Detection limits for HD202917 (Wisdom)
Mp
ap

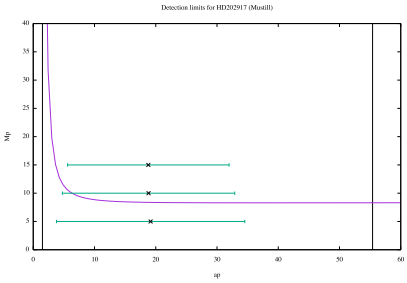
Detection limits for HD202917 (Mustill)
Mp
ap

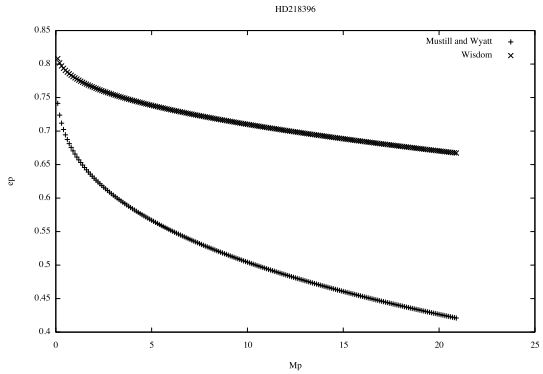
HD218396
Mustill and Wyatt
Wisdom
ep
Mp

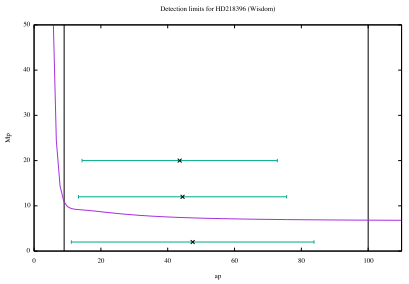
Detection limits for HD218396 (Wisdom)
Mp
ap

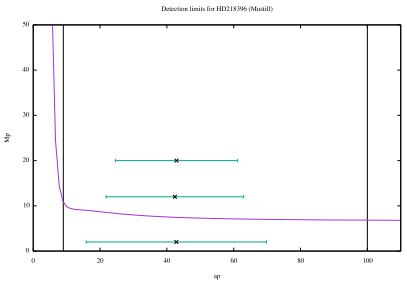
Detection limits for HD218396 (Mustill)
Mp
ap

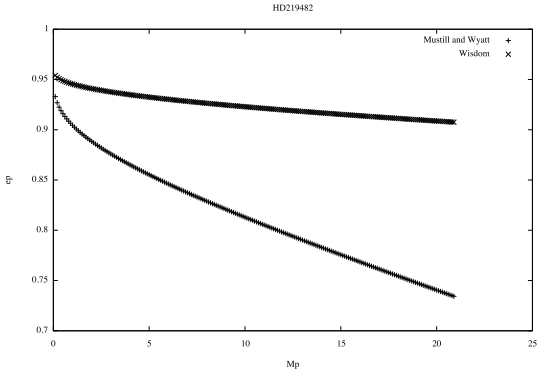
HD219482
Mustill and Wyatt
Wisdom
ep
Mp

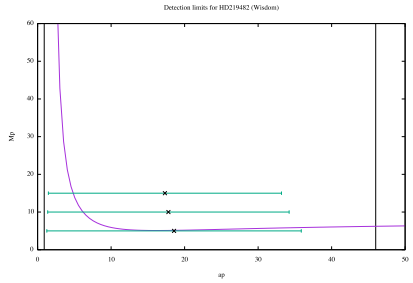
Detection limits for HD219482 (Wisdom)
Mp
ap

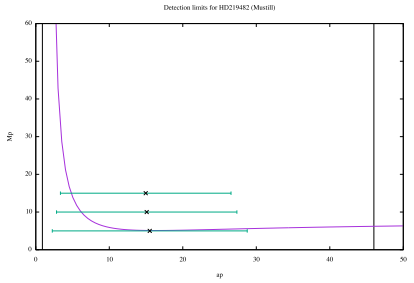
Detection limits for HD219482 (Mustill)
Mp
ap

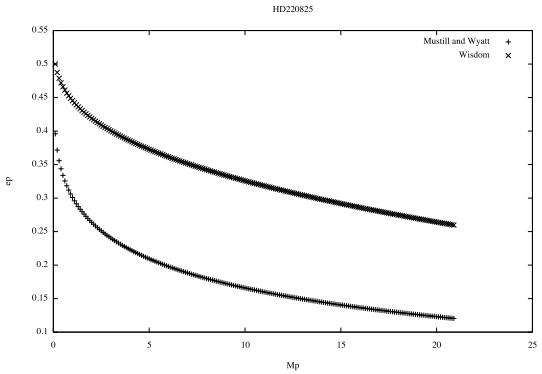
HD220825
Mustill and Wyatt
Wisdom
ep
Mp

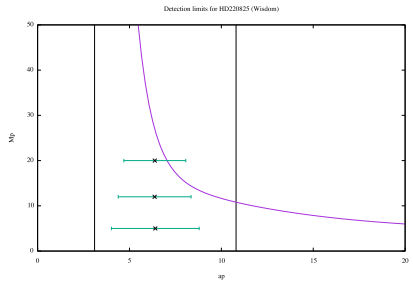
Detection limits for HD220825 (Wisdom)
Mp
ap

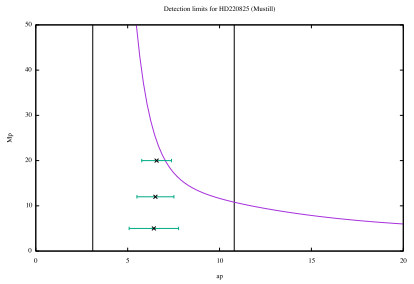
Detection limits for HD220825 (Mustill)
Mp
ap

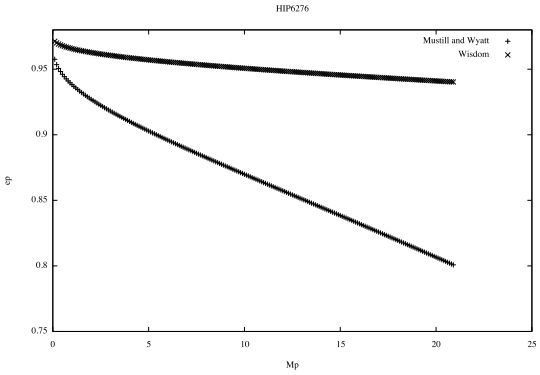
HIP6276
Mustill and Wyatt
Wisdom
ep
Mp
0.95
0.9
0.85
0.8
0.75
0
5
10
15
20
25

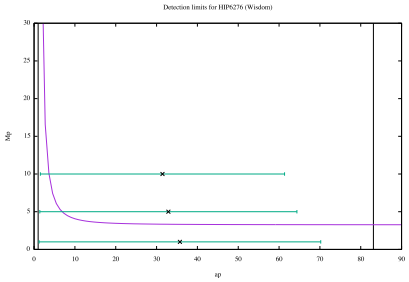
Detection limits for HIP6276 (Wisdom)
Mp
ap

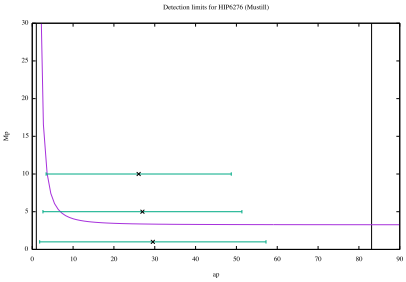
Detection limits for HIP6276 (Mustill)
Mp
ap

Appendix C

Multiple planets

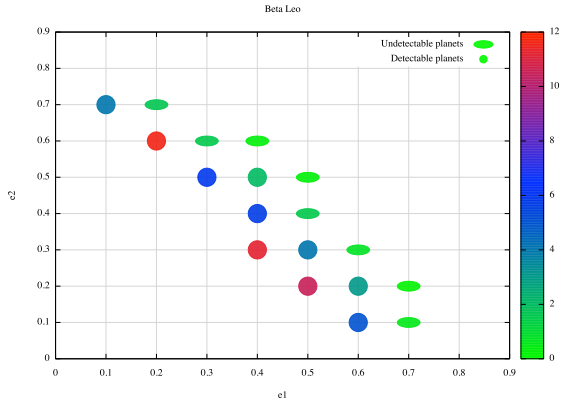

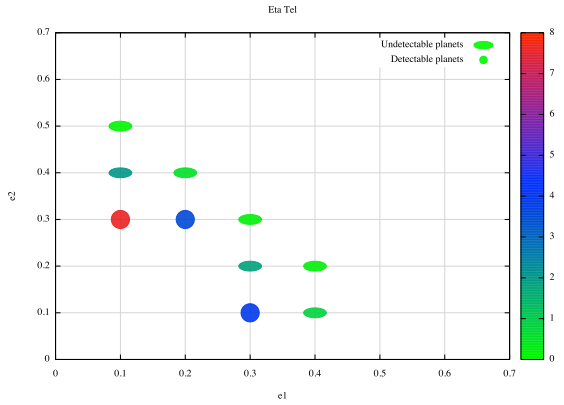

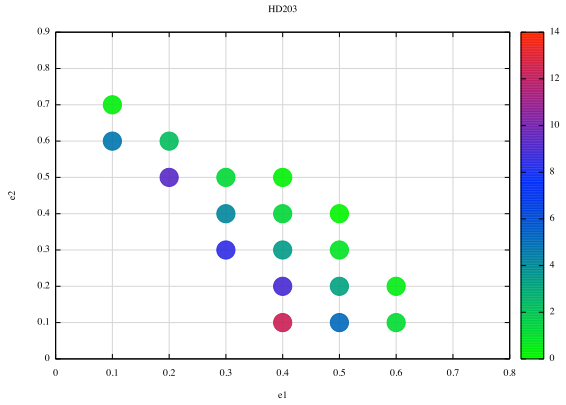
HD203
e2
e1

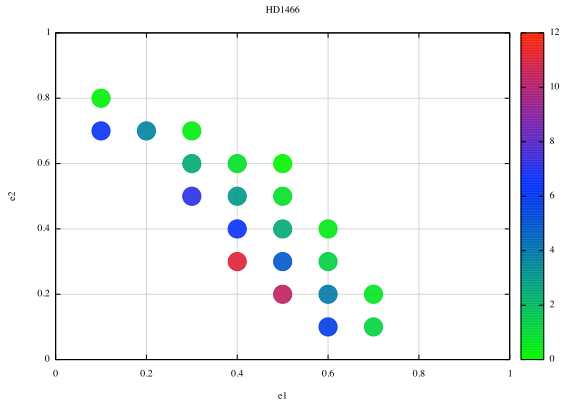
HD1466
e2
e1

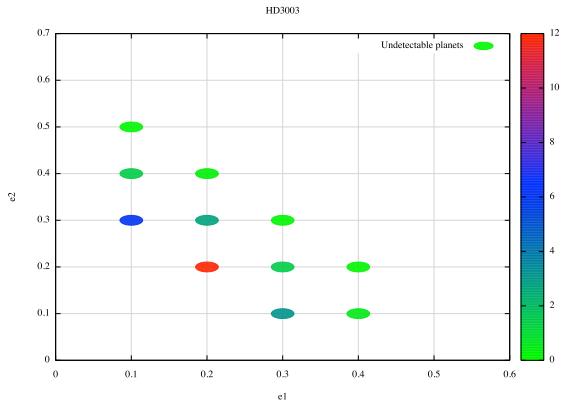
HD3003
Undetectable planets
e2
e1

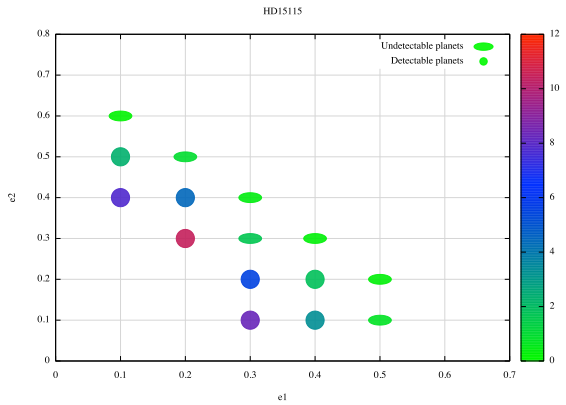
HD15115
Undetectable planets
Detectable planets
e2
e1

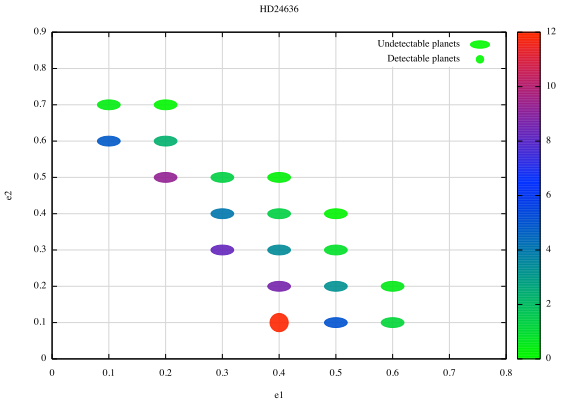
HD24636
Undetectable planets
Detectable planets
e1
e2

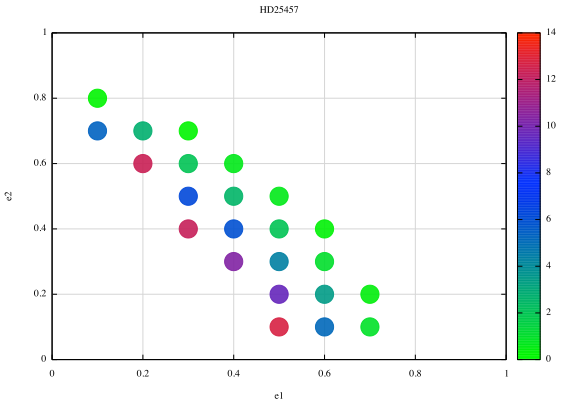
HD25457
e1
e2

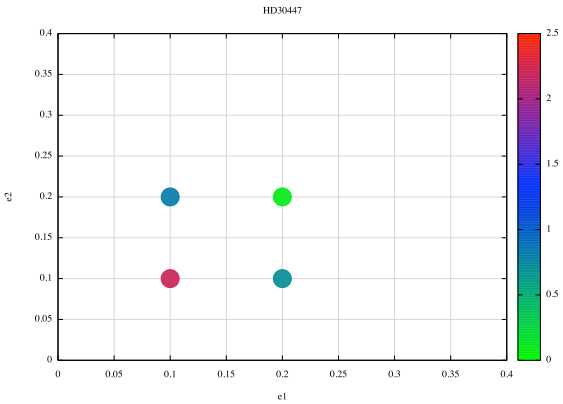
HD30447
e1
e2

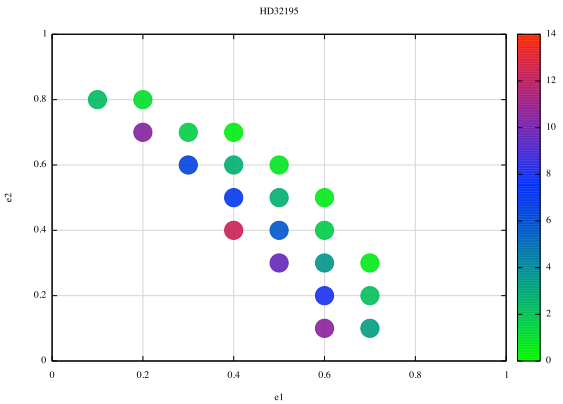
HD32195
e1
e2

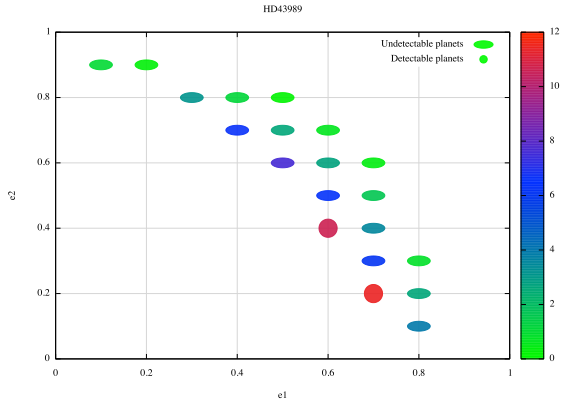
HD43989
Undetectable planets
Detectable planets
e1
e2

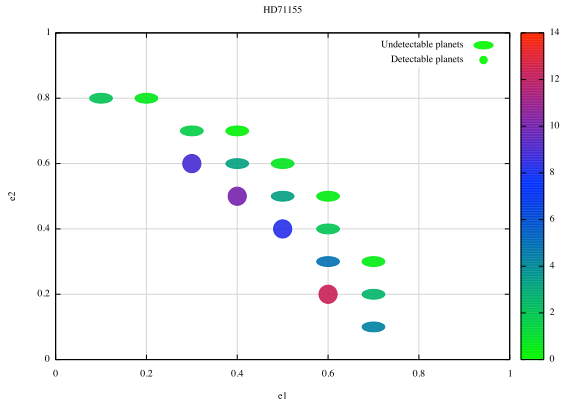
HD71155
Undetectable planets
Detectable planets
e1
e2

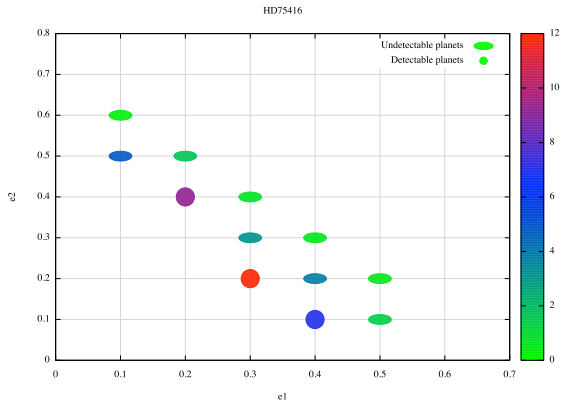
HD75416
Undetectable planets
Detectable planets
e1
e2

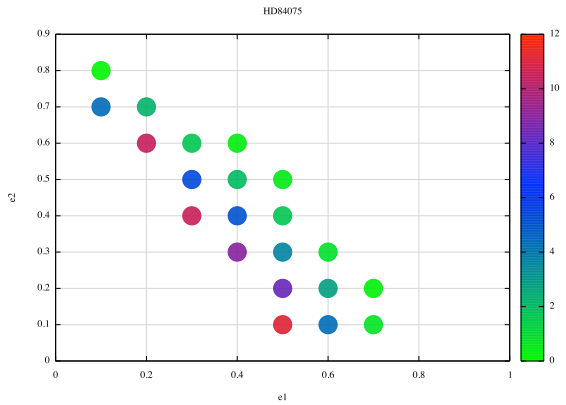
HD84075
e1
e2

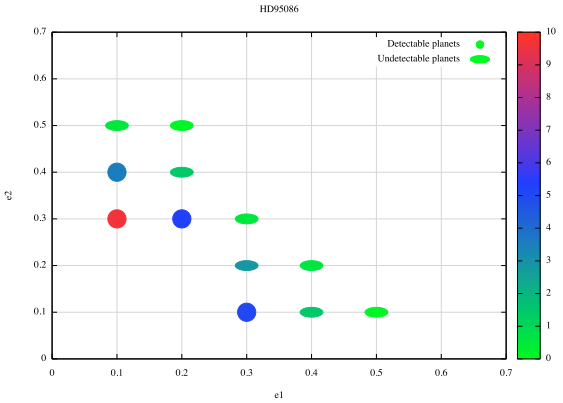
HD95086
Detectable planets
Undetectable planets
e1
e2

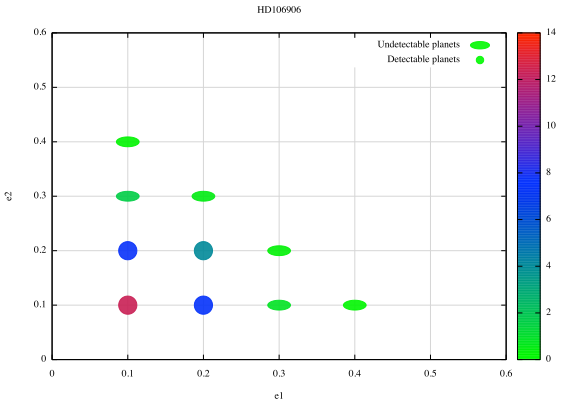
HD106906
Undetectable planets
Detectable planets
e1
e2

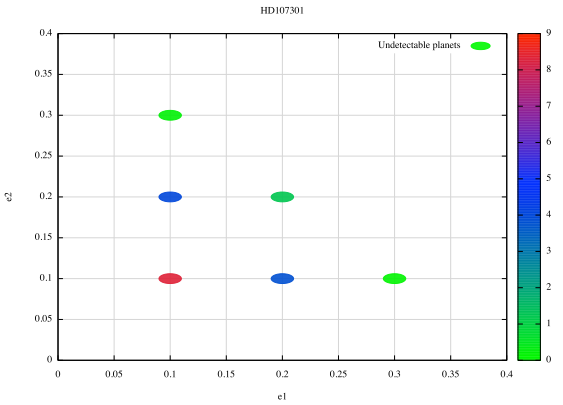
HD107301
Undetectable planets
e1
e2

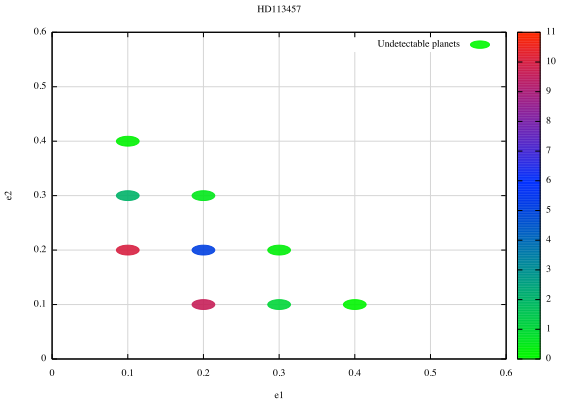
HD113457
Undetectable planets
e1
e2

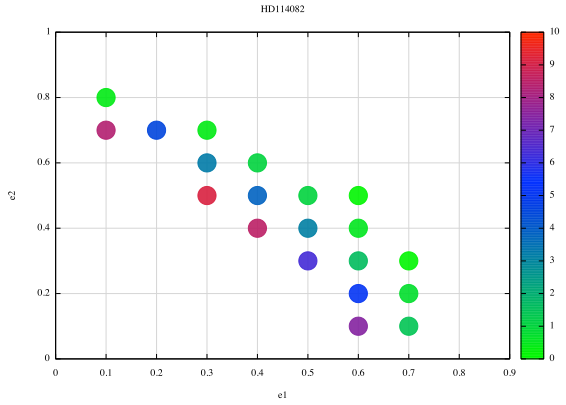
HD114082
e2
e1

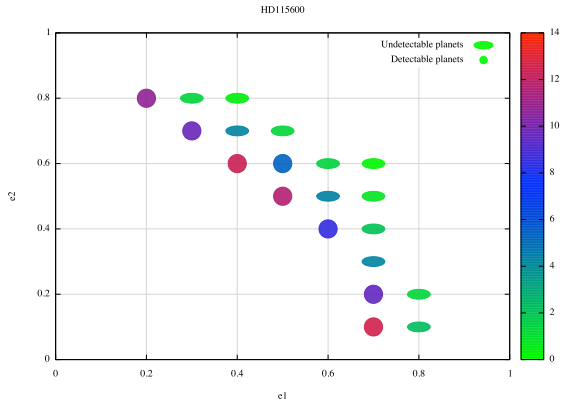
HD115600
Undetectable planets
Detectable planets
e2
e1

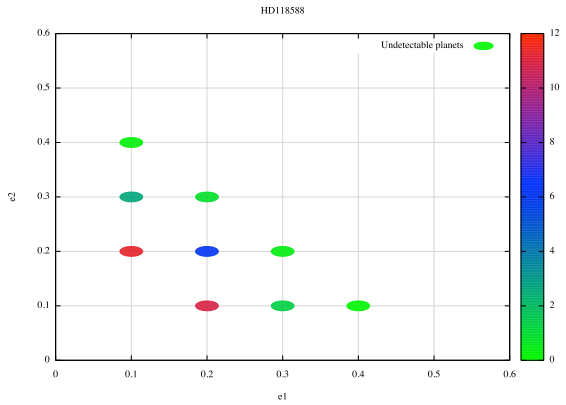
HD118588
Undetectable planets
e2
e1

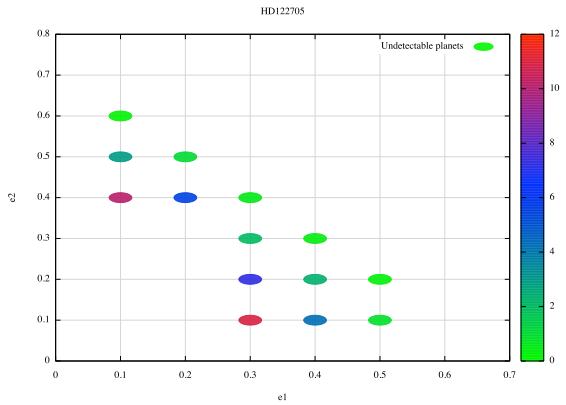
HD122705
Undetectable planets
e2
e1

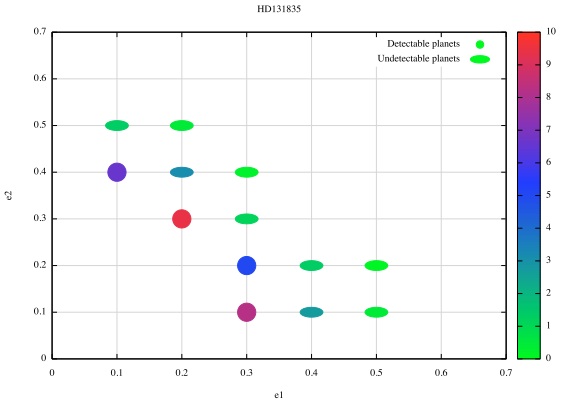
HD131835
Detectable planets
Undetectable planets
e1
e2

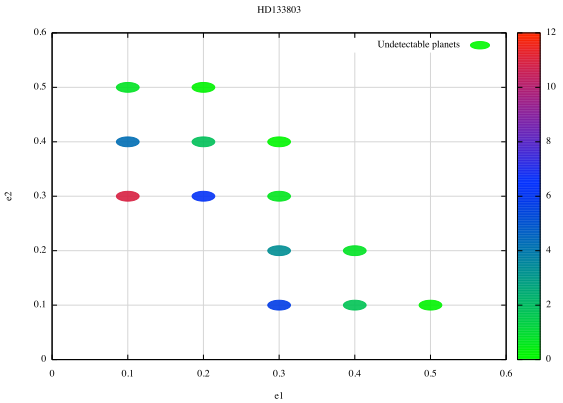
HD133803
Undetectable planets
e1
e2

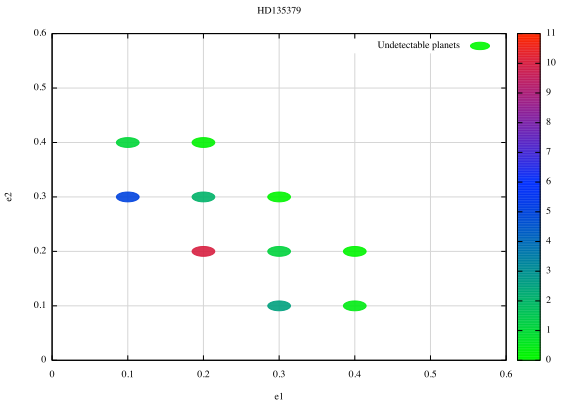
HD135379
Undetectable planets
e1
e2

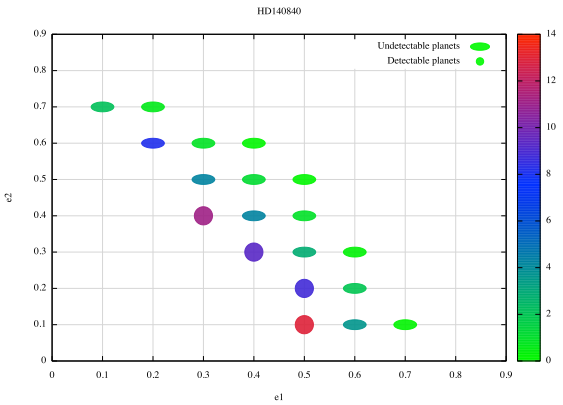
HD140840
Undetectable planets
Detectable planets
e1
e2

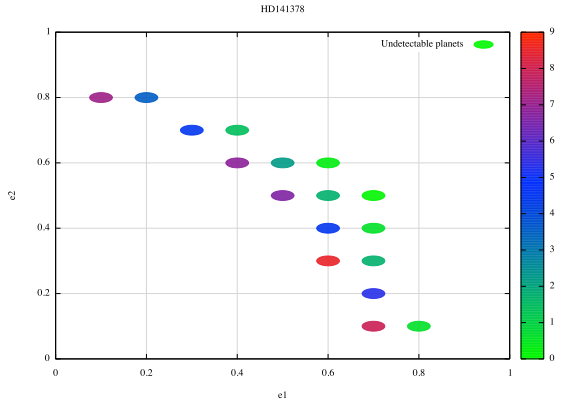
HD141378
Undetectable planets
e2
e1

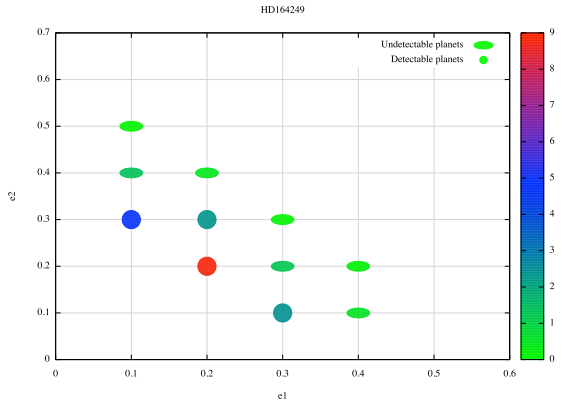
HD164249
Undetectable planets
Detectable planets
e2
e1

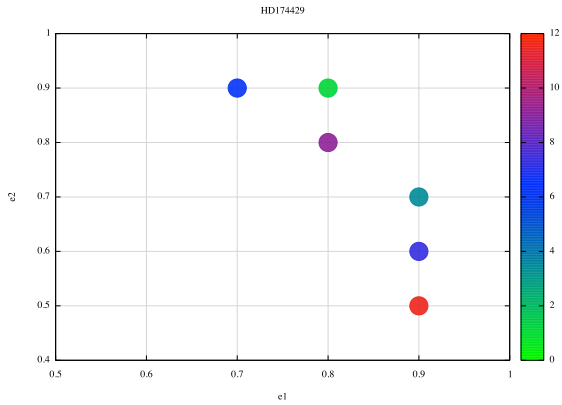
HD174429
e2
e1

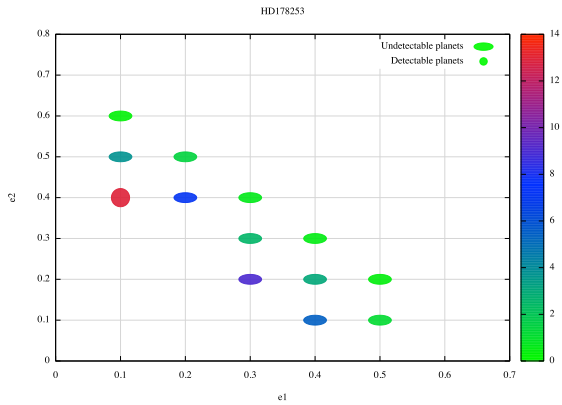
HD178253
Undetectable planets
Detectable planets
e2
e1

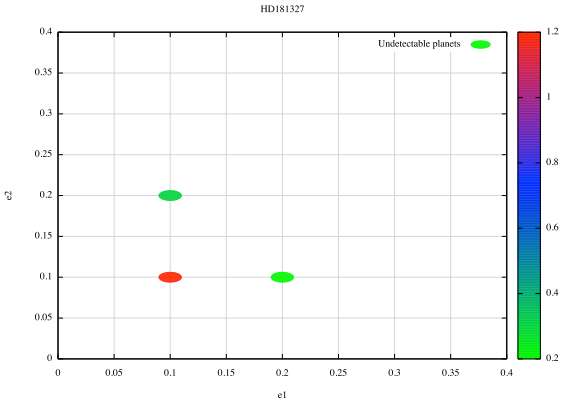
HD181327
Undetectable planets
e1
e2

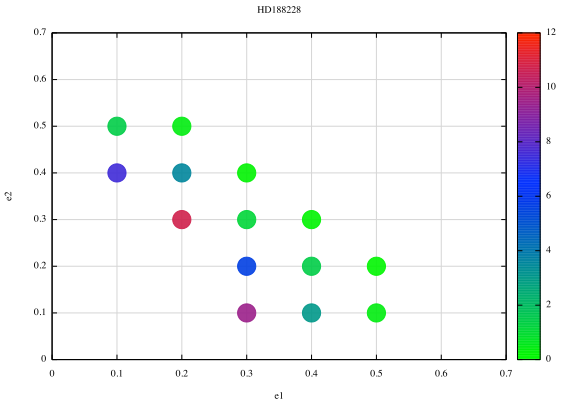
HD188228
e1
e2

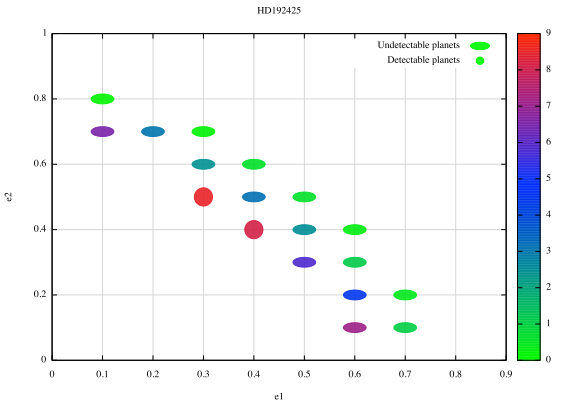
HD192425
Undetectable planets
Detectable planets
e1
e2

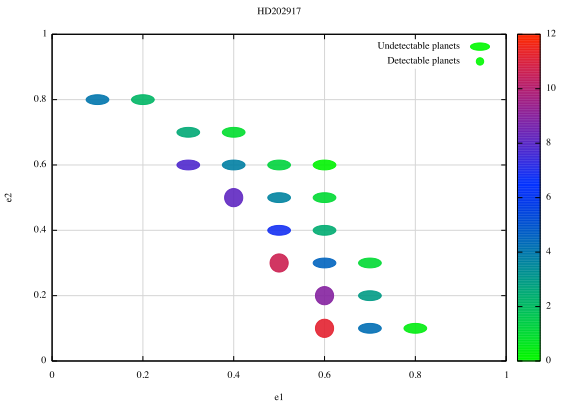
HD202917
Undetectable planets
Detectable planets
e1
e2

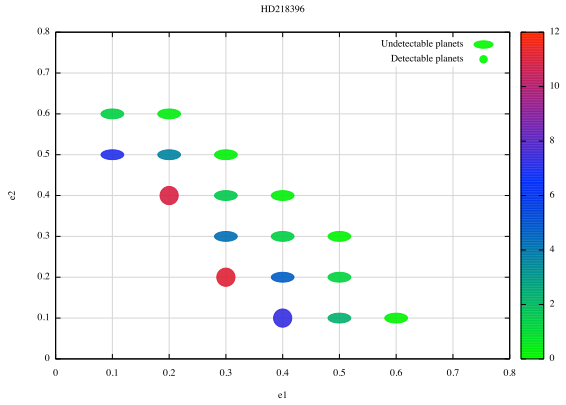
HD218396
Undetectable planets
Detectable planets
e1
e2

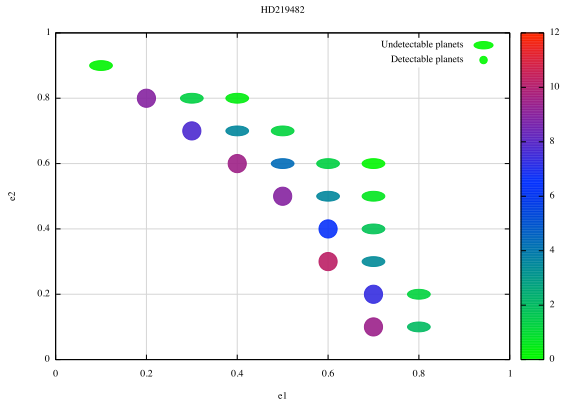
HD219482
Undetectable planets
Detectable planets
e1
e2

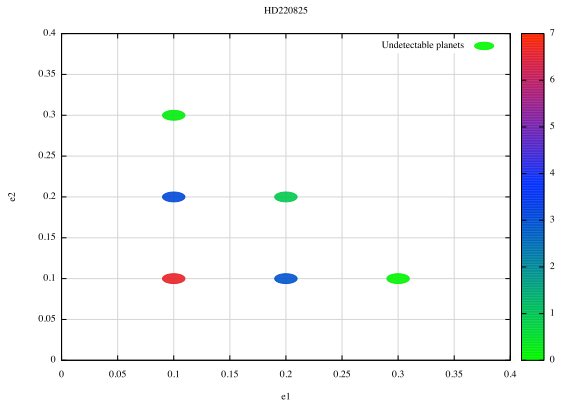
HD220825
Undetectable planets
e1
e2

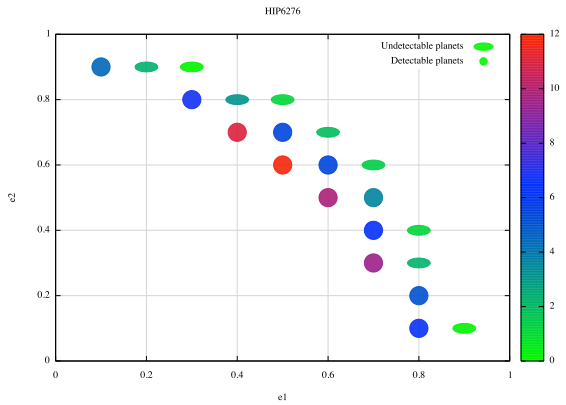
HIP6276
Undetectable planets
Detectable planets
e1
e2

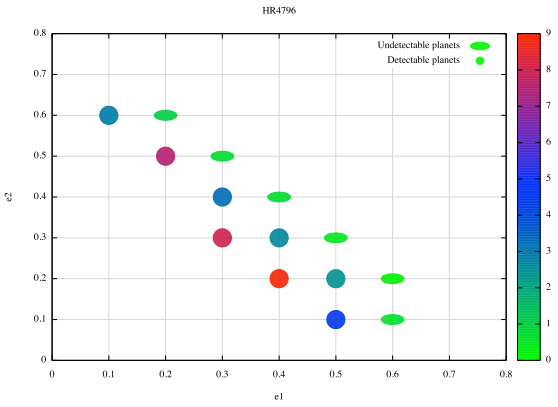
HR4796
Undetectable planets
Detectable planets
e2
e1
0
0.1
0.2
0.3
0.4
0.5
0.6
0.7
0.8
0
1
2
3
4
5
6
7
8
9

Appendix D

HIP67497

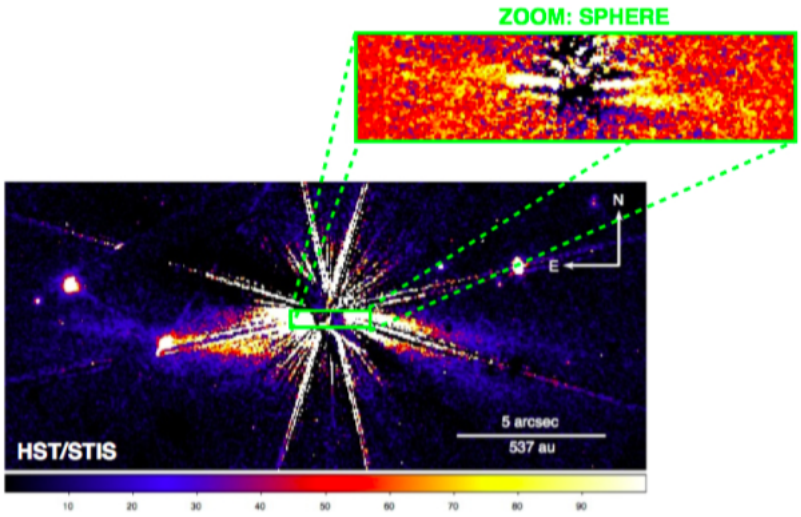

Figure D.1: Debris disk around HIP67497 as imaged with the HST/STIS and with SPHERE

HIP67497 is a F0 type star that belongs to the Upper Centaurus Lupus sub-group, thus with an estimated age of 16 Myr at nearly 107 pc from the Sun and with a mass $M_* = 1.6 M_\odot$. Moreover, this system has a large infrared excess ($L_{IR}/L_* \sim 10^{-3}$) that is indicative of the presence of a bright debris disk. The star is included among two-belts systems in C14 although alternative models to SED fitting have also been proposed. HIP67497 was observed with SPHERE as a part of an open time program devoted to the study of dual-belt systems and such data enable the first spatially resolved images of the disk. Results of direct imaging analysis seem to point to an highly inclined ring with almost no eccentricity and a second fainter belt further out. Also a model with a single ring and a continuos component was investigated but the system was best described by two belts. We show in table D.1 results obtained by applying the first model.

	PA(°)	d(AU)	i(°)
inner belt	-93 ± 1	58.6 ± 3	80 ± 1
outer belt	-93 ± 1	130 ± 8	80 ± 1

Table D.1: Position angle, position of the belt and inclination for the two rings

Such conclusions are presented in Bonnefoy et al. 2016, submitted to *Astronomy and Astrophysics*. As a part of the analysis included in this paper, we investigate the presence of one or more planet between the two belts applying the method described in chapter 6 and 7.
We first investigate the presence of one, two or three planets on circular orbits. Moreover, for the two and three planets models we assume equal masses. We show in figure D.2 values of mass as function of the distance of the planet from the star for each model. If just one planet is present it should have a mass of 20.6 M_J at a separation of ~ 90 AU and thus it would have been already detected in SPHERE images. For two planets the situation quite improves since they would have $M_p = 2.7\ M_J$ at separations of $a_{p,1} \sim 73$ AU and $a_{p,2} \sim 105$ AU, getting nearer to the detection limit curve. Indeed, a candidate companion of $\sim 2.5\ M_J$ at ~ 100 AU was detected and it is now under further investigation. For the three planets assumption we get $M_p \sim 0.14\ M_J$ at separations of $a_{p,1} \sim 64$ AU, $a_{p,2} \sim 88$ AU and $a_{p,3} \sim 119$ AU. In this case we are well beneath detectability.
For one planet on eccentric orbit, we show the variation of the eccentricity as

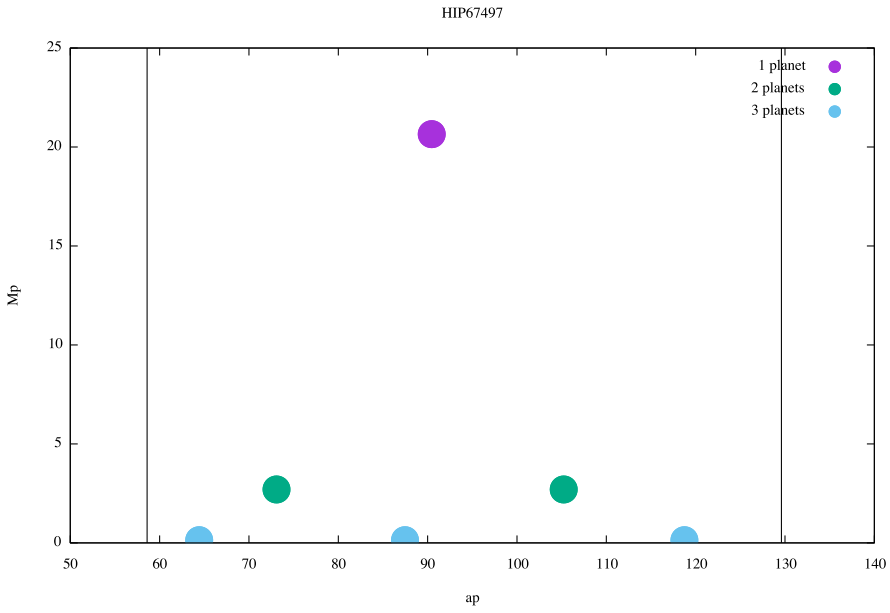

Figure D.2: Masses and positions for models with one, two and three planets on circular orbits. The black lines show the positions of the two belts.

a function of M_p in figure D.3. Since the semi-major axis of the planet varies between 95 AU and 120 AU, we deduce from the detection limits curve available in the paper that the minimum mass that the planet must have to be revealed is $\sim 2\ M_J$. From figure D.3 it is clear that smaller masses can be reached at modest eccentricities, confirming the possible presence of one planet not yet detected.

At the end, we investigate the presence of two equal-mass planets on eccentric

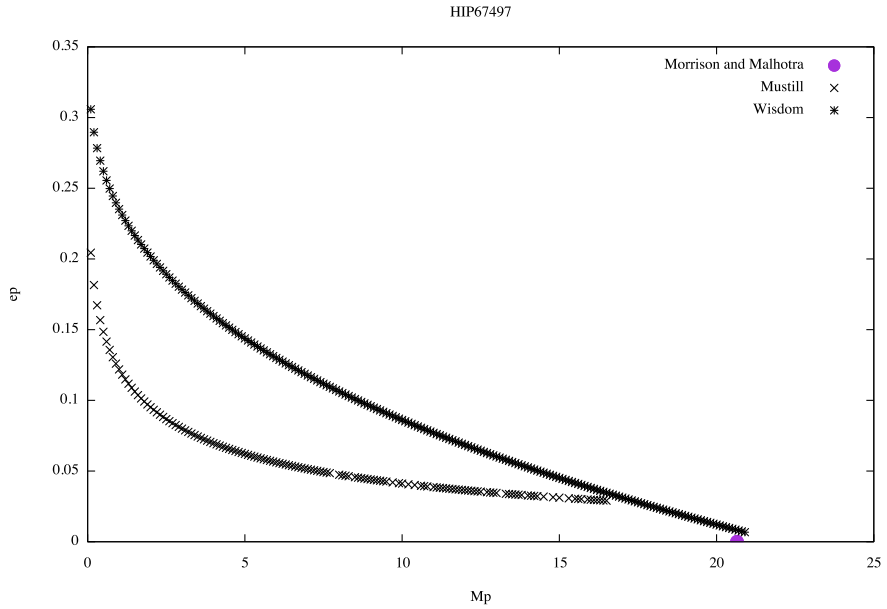

Figure D.3: Dependence of the eccentricity of the planet on its mass obtained from Wisdom (asterisks), Mustill & Wyatt (crosses) and Morrison & Malhotra (circle) expressions.

orbits. Results are shown in figure D.4. Planets' masses for this assumption varies in the range $[0.1, 0.4]\ M_J$ with quite small eccentricities $(0.1 - 0.2)$, below detection limits curve. As mentioned above, we are interested in looking for giant planets but smaller objects on higher eccentric orbits could be responsabile for the edges of the two belts.

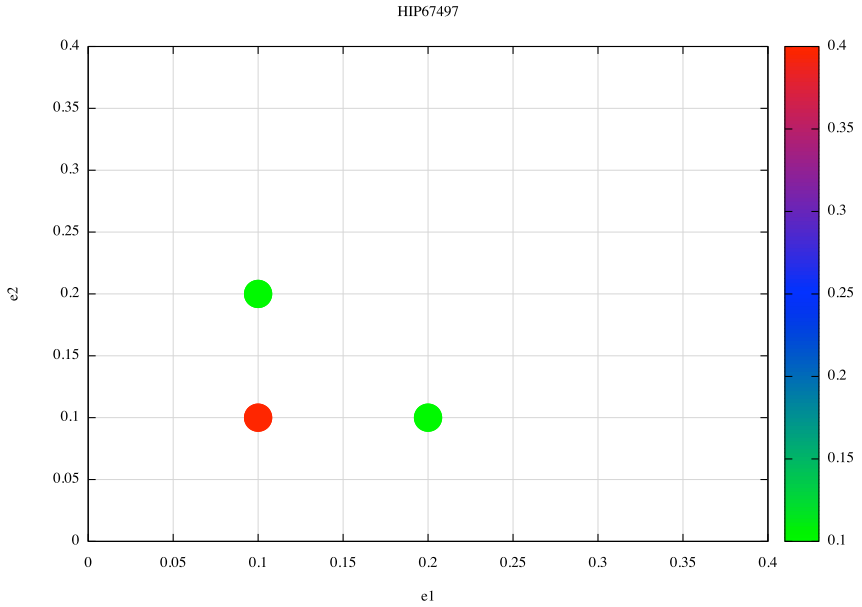

Figure D.4: Results for eccentricities of the inner ($e_{p,1}$) and outer ($e_{p,2}$) planets as a function of mass, represented by a graduation of colors. Possible values of M_p, in this case, belong to $[0.1, 0.4]$ M_J range.

Bibliography

[1] Armitage, P. J. 2010, Astrophysics of planet formation

[2] Booth, M., et al. 2013, Mon. Not. R. Astron. Soc. 428, 1263

[3] Broekhoven-Fiene, H., et al. 2012, Astrophys. J. arXiv:1212.1450v1

[4] Chen, C. H., et al. 2014, Astrophys. J. Suppl., 211, 25

[5] Currie, T., et al. 2015, Astrophys. J. Lett., 807, L7

[6] Gladman, B. 1993, ICARUS 106,247

[7] Hung, L.W., et al. 2015, Astrophys. J. 802, 138

[8] Kasper, M. et al 2012, The Messenger, 149, 17

[9] Krivov, A. V. 2010, Res. Astron. Astrophys., 10, 383

[10] Labadie, L., et al. 2014, SPIE Astron. Tel. Instr. Conf., arXiv:1408.3876v1

[11] Lagtange, A. M., et al. 2016, Astron. Astrophys. 586, L8

[12] Qulline, A. C. and Faber, P. 2006, Mon. Not. R. Astron. Soc. 373, 1245

[13] Marois, C., et al. 2010, arXiv:1011.4918v1

[14] Marzari, F. 2014, Mon. Not. R. Astron. Soc., arXiv:1405.1667.v2

[15] Matthews, B., et al. 2014, Astrophys. J. 780, 97

[16] Moerchen, M. M., et al. 2010, Astrophys. J. 723, 1418

[17] Moro-Martin, A. 2012, arXiv:1203.0005v2

[18] Morrison, S. and Malhotra, R. 2014, Astrophys. J. 637,799

[19] Mustill, A. J. and Wyatt, M.C. 2009, Mon. Not. R. Astron. Soc. 399, 1403

[20] Mustill, A. J. and Wyatt, M.C. 2012, Mon. Not. R. Astron. Soc. 419, 3074

[21] Rodigas, T. J., et al. 2012, Astrophys. J. 752,57

[22] Schneider, G., et al. 2014, Astrophys. J. 148, 59

[23] Schnerider, G., et al. 2016, Astrophys. J., arXiv:1606.00039v1

[24] Smith, R., et al. 2009, Astron. Astrophys. 493, 299

[25] Soummer, R., et al. 2014, Astrophys. J. Letter 786, L23

[26] Su, K. Y. L., et al. 2015, Astrophys. J. 799, 146

[27] Wisdom, J. 1980, Astron. J. 85, 8

[28] Wyatt, M. C. 2008, Ann. Rev. Astron. Astrophys., 46, 339

Ackonwledgment

We would like to thank Dino Mesa for letting us use his program to convert magnitudes in planet's masses and Mikael Bonnefoy for the data on HIP67497.